UNIVERSITY OF LJUBLJANA
FACULTY OF MATHEMATICS AND PHYSICS

Borut Eržen

Measurement of the $|V_{cs}|$ with the DELPHI Spectrometer

Doctoral Thesis

Supervisor: prof. dr. Danilo Zavrtanik

Ljubljana, 1999

UNIVERZA V LJUBLJANI
FAKULTETA ZA MATEMATIKO IN FIZIKO

Borut Eržen

Meritev matričnega elementa $|V_{cs}|$ s spektrometrom DELPHI

Disertacija

Mentor: prof. dr. Danilo Zavrtanik

Ljubljana, 1999

to Metka and Vid

Delo je bilo opravljeno pri eksperimentu DELPHI v Evropskem laboratoriju za fiziko delcev CERN v Ženevi, v okviru raziskovalnega programa Odseka za eksperimentalno fiziko osnovnih delcev Instituta Jožef Stefan. Financiralo ga je Ministrstvo za znanost in tehnologijo Republike Slovenije.

I would like to express my utmost gratitude to Tomaž Podobnik for many sparkling ideas, discussions and his interest in my work.

To my supervisor Prof. Danilo Zavrtanik I am most grateful for giving me opportunity to participate in the High energy physics and for his constant support.

For s-advises, s-motivation and s-coffees I wish to express my special gratitude to Olav Ullaland.

I especially thank Boštjan Golob for his patience in guiding me trough the DELPHI software and all valuable suggestions and cross-checks he made during the analysis.

Many thanks go to Emil Schyns for a nice cooperation and his feed-back during development of our software.

Whenever I needed computer-help Andrej Filipčič was there with a 3 minutes delay. Many thanks to Andrej.

For a critical reading of draft I am especially grateful to Prof. Gabrijel Kernel, Prof. Danilo Zavrtanik, Boštjan Golob and Tomaž Podobnik.

It was a privilege for me to work in a friendly and dynamical environment at the department of High energy physics at Jožef Stefan Institute. My gratitude goes to Marko Mikuž as the Chief of the Department.

I acknowledge all visitors and shareholders of 'Cukrarna' for all memorable and non-memorable discussions and events.

Many great thanks go to my parents, my brother, and sister for their outstanding support and understanding.

Finally, I am utmost grateful to Metka for patience during my work and frequent stays abroad and for giving birth to Vid during my over-occupation in the last months.

There is a theory which states that if ever anyone discovers exactly what the Universe is for and why it is here, it will instantly disappear and be replaced by something even more bizarre and inexplicable.

Douglas Adams, *The Restaurant at the End of the Universe*

There is another theory which states that this has happened already.

Alojz Kodre, *Restavracija ob koncu Vesolja*

Abstract

Decays of W^+W^- pairs produced at the LEP2 collider were used to measure the $|V_{cs}|$ element of the Cabibbo-Kobayashi-Maskawa (CKM) matrix. Analysis was applied to data recorded by the DELPHI detector at the e^+e^- center of mass energies of 161, 172 and 183 GeV. At these energies the integrated luminosity of approximately 70 pb^{-1} was delivered in the years 1996 and 1997. Produced W^+W^- pairs were separately selected in the hadronic, mixed, and leptonic decay channel. The selected events provided a measurement of the hadronic branching ratio of the $W^\pm$ bosons and the total cross-section for the W^+W^- production. The measured hadronic branching ratio was interpreted in terms of the $|V_{cs}|$ element whereby the previously measured values of other CKM elements are used. In addition, the value of the $|V_{cs}|$ element was obtained from the measured fraction of cs di-jets in the hadronic decays of $W^\pm$ bosons. Separation between cs di-jets and other flavour combinations was achieved by making use of measured impact parameters of charged tracks and of measured momentum spectra of particles identified by the DELPHI RICH counters. Combination of results of two measurements yields:

$$|V_{cs}| = 1.01 \pm 0.06\,(\text{stat.}) \pm 0.03\,(\text{syst.}).$$

This value in combination with the previously measured values of other CKM elements is consistent with the unitarity of the CKM matrix as predicted by the Standard model. If the unitarity constraint is imposed on the measured values of CKM elements while the number of quark families is not limited, the 90% confidence interval for the value of $|V_{cs}|$ lies between 0.925 and 0.975. The achieved precision of $|V_{cs}|$ exceeds the combination of all previous measurements by more than a factor of two.

Keywords: CKM matrix, $|V_{cs}|$, W boson, decays of W boson, flavour tagging, DELPHI, LEP.

PACS:
12.15.Hh Determination of Kobayashi-Maskawa matrix elements
14.70.Fm W boson
12.15.-y Electroweak interactions

Povzetek

Na podlagi analize razpadov bozonov W^+W^-, nastalih na trkalniku LEP2, smo izmerili element $|V_{cs}|$ matrike Cabibbo-Kobayashi-Maskawa (CKM). Analizirali smo podatke, zbrane z detektorjem DELPHI, pri težiščnih energijah elektronov in pozitronov 161, 172 in 183 GeV. Podatki, zbrani v letih 1996 in 1997, ustrezajo integrirani luminoznosti 70 pb^{-1}. Nastale pare bozonov W^+W^- smo ločeno izbrali v hadronskem, mešanem in leptonskem razpadnem načinu. Na podlagi števila izbranih dogodkov smo izmerili presek za nastanek parov bozonov W^+W^- in delež hadronskih razpadov bozonov $W^{\pm}$. Element $|V_{cs}|$ smo izračunali iz izmerjenega deleža hadronskih razpadov bozonov $W^{\pm}$, pri čemer smo uporabili predhodno izmerjene vrednosti ostalih elementov matrike CKM. Vrednost elementa $|V_{cs}|$ smo določili tudi iz merjenega deleža kvarkovskih parov cs med hadronskimi razpadi bozonov $W^{\pm}$. Kot kriterij za ločevanje parov cs od ostalih kvarkovskih parov so nam služili izmerjeni vpadni parametri nabitih sledi in izmerjeni spektri gibalnih količin delcev, ki jih identificiramo z detektorjem Čerenkovih obročev RICH. Kombinacija rezultatov obeh meritev vodi do vrednosti:

$$|V_{cs}| = 1.01 \pm 0.06\,(\text{stat.}) \pm 0.03\,(\text{sist.}).$$

Izmerjena vrednost, skupaj s predhodno merjenimi vrednostmi ostalih elementov matrike CKM, sovpada z napovedjo Standardnega modela, da je matrika CKM unitarna. Če zahtevamo, da je matrika CKM unitarna, medtem ko števila kvarkovskih družin ne omejimo, vrednost elementa $|V_{cs}|$ leži med 0.925 in 0.975 ob 90% stopnji zaupanja. Natančnost izmerjene vrednosti elementa $|V_{cs}|$ za več kot dvakrat presega natančnost kombiniranega rezultata predhodnih meritev.

Ključne besede: matrika CKM, $|V_{cs}|$, bozon W, razpadi bozona W, določanje okusa kvarkov, DELPHI, LEP.

PACS:
12.15.Hh Determination of Kobayashi-Maskawa matrix elements
14.70.Fm W boson
12.15.-y Electroweak interactions

Contents

1

Introduction

In 1950's and 1960's a host of new hadrons were discovered and among these were many that decay via the weak interaction. However, some differences were observed in the invariant decay amplitudes as for instance between decays of $\pi^- \to \mu^- \bar{\nu}_\mu$ and $K^- \to \mu^- \bar{\nu}_\mu$. The observed differences were opposing a universal theory of weak interaction. In 1963 N. Cabibbo [1] formulated a hypothesis of mixing between hadronic currents. One year later Gell-Mann [2] and Zweig [3] introduced quarks as fundamental constituents of hadrons and the mixing was naturally attributed to quarks. Weak eigenstates of quarks were considered as a linear combination of the mass eigenstates of quarks. Nowadays, this hypothesis is a part of the Standard Model of electroweak interaction formulated by Glashow, Salam, and Weinberg [4, 5, 6] during the late 1960's. By introduction of the mixing between quarks the electroweak interaction appears with a universal form and coupling strength for all quarks and leptons. This has been verified experimentally with a high precision.

The mixing between 6 quarks known today is described by a unitary 3×3 Cabibbo-Kobayashi-Maskawa (CKM) matrix. Apart from elements related to the heaviest t quark, the V_{cs} element is measured with the poorest precision among others. Therefore, an improved measurement of V_{cs} enables a more stringent test of the unitarity and consequently a test of the Standard Model.

The weak interactions between quarks of different charges are mediated by $W^\pm$ bosons. The LEP environment with the production of real $W^\pm$ bosons provides a unique opportunity to measure the absolute value of the V_{cs} element with an improved precision. The thesis presents the measurement of $|V_{cs}|$ based on data collected with the DELPHI detector at the LEP collider.

In Chapter 2 the CKM matrix is introduced and possibilities to measure $|V_{cs}|$ in combination with the W^+W^- pair production at LEP2 are discussed. The experimental environment including the LEP collider and the DELPHI detector is presented in Chapter

3. In the next Chapter some general methods of the off-line data analysis are reviewed. The emphasis is given to the fine tuning of the Vertex Detector and the RICH counters as the crucial detectors for the presented analysis. The method used to select the W^+W^- events is presented in Chapter 5. The selected events are interpreted in the next Chapter in terms of the cross-section for the W^+W^- pair production, the hadronic branching ratio of the $W^\pm$ bosons, and $|V_{cs}|$ obtained from the latter. An alternative method to measure $|V_{cs}|$ makes use of tagged $W^\pm \to cs$ di-jets. The tagging algorithm is described in Chapter 7. The likelihood fit which provides the fraction of cs di-jets in the hadronic $W^\pm$ decays and consequently the value of $|V_{cs}|$ is presented in the next Chapter. In Chapter 9 the results of the two methods are reviewed, combined, and compared with other measurements of the $|V_{cs}|$ element.

2

Theoretical framework

2.1 The Standard Model and the CKM matrix

The Standard Model (SM) [4, 5, 6] describes properties and interactions among elementary particles of the nature. It incorporates and combines the postulates of special relativity and quantum mechanics into a consistent and predictive quantised field theory. Its predictions are suitable to basically all experimental observations up to currently available energies of about 200 GeV. Therefore, the Standard Model is widely accepted among high energy physicists.

In the theory of elementary particles the dynamics and interactions of particles are usually described by the Lagrange density. Calculations of physical observables are expressed as a perturbation expansion in the number of point like couplings and are typically represented by Feynman diagrams. Every vertex contributes the corresponding coupling constant to the term in the series. In the Standard Model all elementary particles are arranged in few discrete symmetry groups with respect to interactions involved. Transitions between particles are allowed only within members of the same symmetry group and are generated by the corresponding group transformations. The central principle of the Standard Model is the invariance of Lagrange density under gauge transformations. In the gauge transformations parameters of transformations continuously vary from one space-time point to another. In this way the renormalisability of the theory is automatically assured [7]. The gauge invariant theory is also very predictive. Once we assume a certain symmetry group for a set of particles the complete form of the Lagrange density is practically determined.

In the following paragraphs we will briefly review the main properties of elementary particles and interactions among them expressed with the language of the SM. For a more detailed overview the reader is advised to consult [8, 9, 10].

boson	q	spin	mass (GeV)	interaction
W^+	$+1$	1	80.41 ± 0.10	weak
W^-	-1	1	80.41 ± 0.10	weak
Z^0	0	1	91.187 ± 9.007	electroweak
γ	0	1	0	electromagnetic
g	0	1	0	strong

Table 2.1: The main properties of bosons: the charge (q), the spin, the mass, and the corresponding interaction . The measured masses are taken from [11].

There are two main types of elementary particles: fermions that posses the spin of $\frac{1}{2}$ and bosons with the spin of 1. Every fermion has an anti-fermion partner with conjugate quantum numbers. Interactions among the elementary particles are grouped into four classes: electromagnetic interaction, weak interaction, strong interaction and gravitation. The electromagnetic and the weak interaction can be considered as parts of a more general electroweak interaction. The gravitation is not yet successfully incorporated within the SM. It is about 19 orders of magnitude weaker than any other interaction, therefore, we will ignore gravitation in the rest of the discussion.

In general, an arbitrary particle will not take part in all interactions. Based on interactions involved we divide fermions into quarks and leptons. Quarks participate in all interactions while leptons interact only trough the electroweak interaction. There are 6 known flavours of quarks denoted as u, d, s, c, b, t and also 6 leptons: $e, \nu_e, \mu, \nu_\mu, \tau, \nu_\tau$.

Bosons can be considered as the mediators of interactions. Eight massless bosons mediating the strong interaction are called gluons. The electroweak interaction is governed by three massive bosons W^+, W^- and Z^0, while photons as massless particles are responsible for the electromagnetic interaction. The main characteristics of bosons are summarised in Table 2.1. The existence of these bosons is automatically predicted by the SM if the gauge invariance of Lagrange densities for free fermions involved in the interactions is required. Apart from the existence of bosons, the gauge principle also determines the coupling of bosons to fermions as well as the self interaction of bosons.

Apart from the spin, particles have to posses additional internal quantum numbers by which they are recognised and distinguished in different interactions. As far as the strong interaction is concerned, experiments confirm that each quark possesses three internal degrees of freedom. The corresponding quantum number is called colour: red, blue, and green. Transitions between different colour states of quarks are generated by eight coloured gluons and are described by transformations of the SU(3) group. Since gluons are coloured, they interact also with each other. The self-interaction of gluons in the combination with the SU(3) group leads to the so called confinement of quarks and gluons.

Quarks and gluons never appear as free particles in the nature. They are constituents of hadrons as the 'colour-less' states. There are two types of hadrons: mesons composed of a quark and an anti-quark ($q_i\bar{q}_j$) and barions composed of three quarks ($q_iq_jq_k$) or anti-quarks ($\bar{q}_i\bar{q}_j\bar{q}_k$). The strong coupling constant α_S becomes larger than 1 at energies below about 1 GeV. Therefore, the perturbative way of calculating measurable quantities fails. This introduces large uncertainties in predictions of processes at low energies.

Within the electromagnetic interaction particles are distinguished by the amount of the basic charge they posses. Leptons like e, μ, and τ carry one unit of the charge. Neutrinos are neutral particles. Therefore, they do not take part in the electromagnetic interaction. Quarks like u, c, t posses $\frac{2}{3}$ of the unit charge, while d, s, and b quarks carry $-\frac{1}{3}$ of the basic charge. The photon itself is neutral. Hence, photons do not interact directly with each other. The electromagnetic interaction, as a scalar interaction, can be described by transformations of the U(1) group.

The weak interaction, or strictly, the electroweak interaction, is of primary importance for the presented analysis. By studying interactions of leptons it has been observed that transitions occur only within members of the following lepton pairs: (e, ν_e), (μ, ν_μ) and (τ, ν_τ). The transitions occur either within the same type of lepton (neutral current) or between e, μ, or τ and the corresponding neutrino (charged current). Neutral currents between different lepton types (like $e \rightarrow \mu$) have not been observed suggesting SU(2) as a suitable symmetry group. The SU(2) symmetry applies for each lepton pair separately, while the corresponding coupling constant is assumed to be universal for all three lepton families. Three bosons required by the SU(2) gauge invariance are identified as the Z^0, W^+ and W^- bosons observed in high energy experiments. The Z^0 boson is involved in the neutral currents while the W^+ and W^- bosons mediate the charge currents. Self-coupling of the electroweak bosons is determined by the gauge invariance.

Studies of angular distributions in charged transitions have shown that the parity is maximally violated in the sense that a process is not identical if the space coordinates are inverted. This implies that the form of the coupling combines a vector (V) and an axial vector (A) part; V-A interaction. The V-A operator projects out particles that are said to be left-handed. This is equivalent to the fact that only the left-handed particles are taking place in the charged transitions and the usual vectorial form of interactions is retained. In the limit where the energy of a particle is large with respect to its mass, the left-handed particles are equivalent to particles with the helicity -1 (i.e. the spin of a particle is oriented opposite to its direction). On the other hand, the Z^0 bosons couple also the right-handed particles, however not with an equal strength as the left-handed. This has lead to the conclusion that the neutral interaction consist of a scalar U(1) transition of both right and left-handed particles and a pure left-handed transition embedded in the $SU(2)_L$

group. The remaining part of the U(1) transitions not proceeding trough the Z^0 bosons is identified as the electromagnetic interaction. Therefore, the electroweak interaction is considered as the group product $SU(2)_L \times U(1)$ and combines the electromagnetic and the weak interaction. Because of the product of two symmetry groups, the coupling constant g_{Z^0} of Z^0 bosons to fermions is slightly different from g_W as the pure $SU(2)_L$ coupling constant.

So far we have discussed features and interpretations of weak interaction in the leptonic sector. Measurements of hadronic interactions have confirmed that the $SU(2)_L \times U(1)$ symmetry of electroweak interaction applies for quarks in a similar manner. Moreover, experiments have implied the universality of the electroweak interaction in the sense that all leptons and quarks couple to bosons Z^0, W^+ and W^- with the same coupling constants g_W and g_{Z^0}. Arrangement of quarks and leptons in left-handed $SU(2)_L$ doublets and right-handed U(1) singlets is presented in Table 2.2.

In comparison with the strong interaction where members of colour triplets are quarks of a given flavour, the members of weak doublets are particles with different masses, thus, physically distinguishable. In general, the weak eigenstates could also be mixtures of the mass eigenstates. Indeed, there are weak decays such as $\pi^-(\bar{u}d) \to \mu^-\bar{\nu}_\mu$ as well as $K^-(\bar{u}s) \to \mu^-\bar{\nu}_\mu$. The decay of π^- is a weak decay in an usual manner proceeding via an annihilation of a $\bar{u}$ and a d quark into a W^- boson that further decays into the lepton pair. The decay of K^- proceeds via an annihilation of a $\bar{u}$ and an s quark. This transition is forbidden by the $SU(2)_L$ symmetry, if weak eigenstates of quarks were equal to the mass eigenstates u, d and s. The invariant partial decay width for the K^- decay amounts to about 5% of the partial decay width for the given π^- decay. On the other hand, experiments have shown no evidence of flavour changing neutral currents like $d \to s$, $u \to c$ ... [11]. A solution to retain the $SU(2)_L$ symmetry and the universality of the weak interaction is to consider weak eigenstates as a linear combination of the mass eigenstates. To describe all possible couplings it is sufficient to rotate only the down-like members (d, s, b), while the up-like members are kept equal to the mass eigenstates.Mixing makes no sense in the leptonic sector as long as neutrinos are considered as massless particles. The weak eigenstates of quarks, denoted by d', s', and b', are expressed as a linear combination of the quark mass eigenstates via a 3×3 unitary matrix V, called the Cabibbo-Kobayashi-Maskawa (CKM) matrix [1, 12]:

$$\begin{pmatrix} d' \\ s' \\ b' \end{pmatrix} = V \begin{pmatrix} d \\ s \\ b \end{pmatrix}, \tag{2.1}$$

fermion			q	interaction
leptons				
$\begin{pmatrix}\nu_{eL}\\ e_L\end{pmatrix}$	$\begin{pmatrix}\nu_{\mu L}\\ \mu_L\end{pmatrix}$	$\begin{pmatrix}\nu_{\tau L}\\ \tau_L\end{pmatrix}$	$\begin{matrix}0\\ -1\end{matrix}$	weak weak, EM
e_R	μ_R	τ_R	-1	weak, EM
quarks				
$\begin{pmatrix}u_L\\ d'_L\end{pmatrix}$	$\begin{pmatrix}c_L\\ s'_L\end{pmatrix}$	$\begin{pmatrix}t_L\\ b'_L\end{pmatrix}$	$\begin{matrix}+\frac{2}{3}\\ -\frac{1}{3}\end{matrix}$	weak, EM, strong weak, EM, strong
u_R	c_R	t_R	$+\frac{2}{3}$	weak, EM, strong
d_R	s_R	b_R	$-\frac{1}{3}$	weak, EM, strong

Table 2.2: List of fermions and their grouping within different interactions.

where elements of the CKM matrix are conventionally denoted as follows:

$$V = \begin{pmatrix} V_{ud} & V_{us} & V_{ub} \\ V_{cd} & V_{cs} & V_{cb} \\ V_{td} & V_{ts} & V_{tb} \end{pmatrix}. \tag{2.2}$$

As a matrix that changes only the basis of quark eigenstates, the CKM matrix is unitary by definition. The unitarity condition can be written as:

$$\sum_{i,k} V^*_{ji} V_{jk} = \delta_{ik}. \tag{2.3}$$

We can easily verify that the unitarity is a sufficient condition for the absence of flavour changing neutral currents:

$$\sum_{i=d-like} \bar{q}'_i q'_i = \sum_{i,j,k} \bar{q}_j U^*_{ij} U_{ik} q_k = \sum_j \bar{q}_j q_j.$$

Physically, nothing will change if we change the phase of each of 6 quarks separately. A common change of all quark phases leaves the CKM matrix invariant. Hence, we are left with 13 parameters and 9 unitarity constraints (Eq. 2.3). Three of four independent parameters are real and one is a phase factor. One of the most commonly used parameterisation of the CKM matrix is the following [13]:

$$V = \begin{pmatrix} c_1 & s_1 c_3 & s_1 s_3 \\ -s_1 c_2 & c_1 c_2 c_3 - e^{i\delta} s_2 s_3 & c_1 c_2 s_3 + e^{i\delta} s_2 c_3 \\ -s_1 s_2 & c_1 s_2 c_3 + e^{i\delta} c_2 s_3 & c_1 s_2 s_3 - e^{i\delta} c_2 s_3 \end{pmatrix},$$

with $c_i = \cos\theta_i$, $s_i = \sin\theta_i$, where $0 \leq \theta_i \leq \frac{\pi}{2}$, and $0 \leq \delta \leq 2\pi$.

The quark mixing described by the CKM matrix is based on the universality of the $SU(2)_L$ symmetry, motivated by the absence of the flavour changing neutral currents. However, if the weak interaction was not universal, we could conditionally still speak about the CKM elements as the relative coupling strengths. The squared matrix element for a charged transition between an up-like quark q_i and a down-like quark q_j, $|M_{q_i \leftrightarrow q_j}|^2$, is proportional to the square of the corresponding CKM element times the coupling constant g_W:

$$|M_{q_i \leftrightarrow q_j}|^2 \propto g_W^2 \cdot |V_{ij}|^2. \tag{2.4}$$

In an experiment we are usually not able to isolate a CKM element from the associated coupling constant. Hence, the CKM element is only an interpretation of the measured coupling strength, whereby the universality of the coupling constant is assumed. In this way, the measured CKM matrix could violate the unitarity condition, if any of the SM assumptions was wrong. If the measured elements were smaller than expected, one could also speculate of having additional quark families that couple to the known ones. Theoretically, there is no strong argument why there should be only 3 quark doublets, though any new quark should be heavier than about 100 GeV if the current experimental limits are considered [11]. Additional doublets of quarks would still fit within the SM, only the dimension of the CKM matrix should be increased to the actual number of quark families. If considering possible scenarios outside the SM, the CKM elements could depend on energy transfer in the transitions. This could appear, for instance, if quarks were bound states, or, if there were other heavier particles that would interfere with the assumed SM processes.

In this thesis we will present a measurement of the coupling of the $W^\pm$ bosons to c and s quarks. The coupling will be interpreted within the SM as a measurement of the $|V_{cs}|$ element. The measurement can serve as a test of the SM in terms of the unitarity of the CKM matrix.

The current world average values of the measured CKM elements are the following [11]:

$$|V^{meas.}| = \begin{pmatrix} 0.9740 \pm 0.0010 & 0.2196 \pm 0.0023 & 0.0033 \pm 0.0008 \\ 0.224 \pm 0.016 & 1.04 \pm 0.16 & 0.0395 \pm 0.0017 \\ ? & ? & ? \end{pmatrix}. \tag{2.5}$$

The elements related to the t quark are measured only relative to each other, thus, not quoted. Among others, $|V_{cs}|$ is measured with the poorest precision. In the first experiments the production of c quarks by scattering neutrinos on nuclei was used to determine $|V_{cs}|$. These measurements set the constraint: $|V_{cs}| > 0.59$ ([14]). The limiting factor is the uncertainty of density of s quarks in the parton sea. An improved precision has been obtained by measuring the decay width of the process: $D^+ \to \bar{K}e^+\nu_e$ [15, 16, 17, 18]. The measured decay width is then compared to the calculated one resulting in:

$$|V_{cs}| = 1.04 \pm 0.16. \tag{2.6}$$

The precision of this results is limited by the theoretical uncertainty of the value of the form factor of D mesons ($f_+^D(0)$).

If the unitarity constraint (Eq. 2.3) is imposed on the measured CKM elements (Eq. 2.5) and no assumption on the number of quark families is made, the following 90% confidence intervals are obtained [11]:

$$|V^{uni.}| = \begin{pmatrix} 0.9724 - 0.9755 & 0.217 - 0.223 & 0.0018 - 0.0044 & ... \\ 0.199 - 0.232 & 0.847 - 0.975 & 0.036 - 0.042 & ... \\ 0 - 0.1 & 0 - 0.36 & 0.05 - 0.9994 & ... \\ . & . & . & ... \end{pmatrix}. \tag{2.7}$$

The limitation to three families of quarks shrinks the intervals to [11]:

$$|V^{uni+6q}| = \begin{pmatrix} 0.9745 - 0.9760 & 0.217 - 0.224 & 0.0018 - 0.0045 \\ 0.217 - 0.224 & 0.9737 - 0.9753 & 0.036 - 0.042 \\ 0.004 - 0.013 & 0.035 - 0.042 & 0.9992 - 0.9994 \end{pmatrix}. \tag{2.8}$$

The value of $|V_{cs}|$ is strongly limited if three families of quarks and the unitarity are imposed. We do not expect that we could come close to this limit with any direct measurement in the near future. This essentially means that we can not significantly improve the constraints on other CKM elements by measuring $|V_{cs}|$.

2.2 $W^{\pm}$ boson at LEP2

The precision of existing measurements of the $|V_{cs}|$ element is mainly limited by theoretical uncertainties concerning the non-perturbative regime of strong processes inside hadrons. A step forward by improving the precision are studies of decays of real $W^{\pm}$ bosons where energies are much higher, thus, calculations become more accurate.

Existence of the $W^{\pm}$ boson was experimentally confirmed in 1983 by the UA1 ([19]) and UA2 ([20]) collaborations at the $Sp\bar{p}S$ collider at CERN. Since then it has been observed also by the CDF ([21]) and D0 ([22]) collaborations at the TEVATRON Collider in Fermi National Laboratories. Both, the TEVATRON and the $Sp\bar{p}S$ are hadron colliders where $W^{\pm}$ bosons are produced in small fractions compared to other processes. These does not provide precise measurements of the $|V_{cs}|$ element. Our experimental environment is the LEP e^+e^- collider. In the phase 2 of LEP operation the center of mass energy was risen above 161 GeV enabling in this way the production of real W^+W^- pairs.

2.2.1 Production and decays of W^+W^- pairs

The leading order Feynman diagrams (CCO3 diagrams) for the production of W^+W^- pairs at LEP2 are shown in Figure 2.1 [23]. In the t-channel the $W^{\pm}$ pairs are produced via a neutrino exchange. In the s-channel the W^+ and W^- bosons directly couple to another gauge boson; Z^0 or γ.

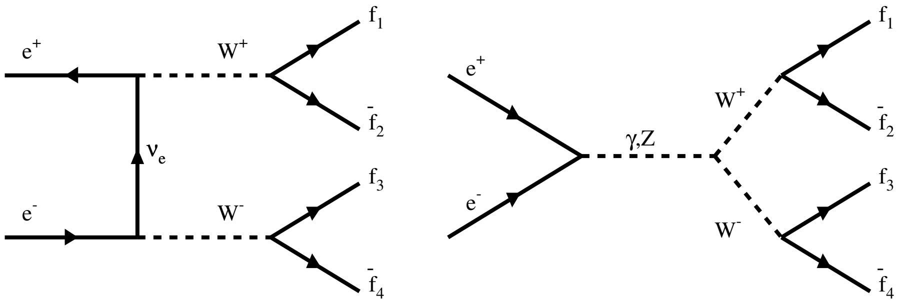

Figure 2.1: The leading order Feynman diagrams for W^+W^- production (CC03 diagrams).

According to the SM, the produced $W^{\pm}$ bosons promptly decay into a fermion and an anti-fermion members of the same weak doublet. To a good approximation the process of $W^{\pm}$ pair creation and decays can be considered as a doubly-resonant Breit-Wiegner resonance where two $W^{\pm}$ bosons propagate and decay independently from each other. In this approximation the partial cross-section $\sigma^0_{WW\to f_1\bar{f}_2,f_3\bar{f}_4}$ as a function of the center of mass energy $\sqrt{s}$ can be written as ([23]):

$$\sigma^0_{WW\to f_1\bar{f}_2,f_3\bar{f}_4}(s) = \frac{\Gamma_{W\to f_1\bar{f}_2}\Gamma_{W\to f_3\bar{f}_4}}{\Gamma_W^2}\int_0^s ds_1 \int_0^{(\sqrt{s}-\sqrt{s_1})^2} \rho(s_1)\rho(s_2)\sigma_0(s,s_1,s_2)ds_2, \quad (2.9)$$

where

$$\rho(s) = \frac{1}{\pi}\frac{\Gamma_W}{M_W}\frac{s}{(s-{M_W}^2)^2+s^2{\Gamma_W}^2/{M_W}^2}, \quad (2.10)$$

and

$$\sigma_0(s,s_1,s_2) = \frac{g_W^4}{256\pi s^2 s_1 s_2}\{a_{\gamma\gamma}+a_{Z^0Z^0}+a_{\gamma Z^0}+a_{\nu\nu}+a_{\nu Z^0}+a_{\nu\gamma}\}. \quad (2.11)$$

$\sigma_0(s, s_1, s_2)$ represents the on-shell cross-section for the $W^\pm$ pair production if $\sqrt{s_1}$ and $\sqrt{s_2}$ were masses of two $W^\pm$ bosons. The terms in brackets describe contributions from diagrams with different intermediate states γ, Z^0 or ν and interferences among them [25]. The coupling constant g_W is related to the Fermi constant G_μ as follows: $q_W^2 = 8M_W^2 G_\mu/\sqrt{2}$. $\rho(s)$ is the propagator term with an energy dependent decay width Γ_W of $W^\pm$ bosons. By definition, Γ_W equals the sum of all partial decay widths $\Gamma_{W \to f_i \bar{f}_j}$:

$$\Gamma_W = \sum_{i,j} \Gamma_{W \to f_i \bar{f}_j}. \tag{2.12}$$

The partial decay width $\Gamma_{W \to f_i \bar{f}_j}$ for decays of $W^\pm$ bosons into fermions f_i and $\bar{f}_j$ can be expressed in the Born approximation as follows:

$$\Gamma_{W \to f_i \bar{f}_j} = N_c^f \frac{g_W{}^2 \cdot M_W}{48\pi} |V_{ij}|^2, \tag{2.13}$$

where V_{ij} is the relevant CKM matrix element applicative in hadronic decays only. N_c^f is the colour factor and is equal 3 for hadronic decays and 1 in the case of a leptonic decay. In above expressions zero fermion masses are assumed. A more precise calculation of the decay widths should include also interactions of final fermions. The corrections are relatively large in particular for hadronic decays due to emission of hard gluons. By inclusion of the QCD corrections to the second order Feynman diagrams the partial decay width for hadronic decays reads:

$$\Gamma_{W \to q_i \bar{q}_j} = 3 \frac{g_W{}^2 \cdot M_W}{48\pi} |V_{ij}|^2 (1 + \frac{\alpha_s(M_W{}^2)}{\pi}), \tag{2.14}$$

where $\alpha_s(M_W{}^2)$ is the effective strong coupling constant at the $W^\pm$ mass. The value $\alpha_s(M_W{}^2) = 0.123$ was evaluated from the one measured at the Z^0 mass [11]. Even more precise calculations of the decay widths were performed numerically and include also finite fermion masses, electroweak and QED corrections. Their values, obtained with the CKM elements determined by the unitarity constraint (see Table 2.8), are displayed in Table 2.3.

Due to the V-A structure of the weak interaction and the gauge induced form of self coupling of the electroweak bosons, the W^- bosons escape predominantly at small angles with respect to the incoming electrons while the W^+ bosons emerge at larger angles (Figure 2.2). In addition, the $W^\pm$ bosons are slightly polarised, whereby the orientation of the polarisation depends on charge of the $W^\pm$ boson. The spin of the W^- boson is likely to be oriented opposite to the direction of its flight, while the spin of the W^+ bosons tends to be oriented along its direction. As a consequence, the up-like fermions are likely to fly at large angles with respect to the $W^\pm$ direction, whereby the angle is calculated in the rest frame of the $W^\pm$ boson. In contrary, the down-like fermions escape at small angles with respect to the direction of the parent $W^\pm$ boson [23].

$\Gamma_{W\to lept}$	0.6763 GeV
$\Gamma^0_{W\to ud}$	0.6684 GeV
$\Gamma^0_{W\to us}$	0.03432 GeV
$\Gamma^0_{W\to ub}$	0.1122×10^{-4} GeV
$\Gamma^0_{W\to cd}$	0.03431 GeV
$\Gamma^0_{W\to cs}$	0.6672 GeV
$\Gamma^0_{W\to cb}$	0.1121×10^{-2} GeV
$\alpha_S(M_W)$	0.123
G_μ	$1.1663910^{-5}\mathrm{GeV}^{-2}$

Table 2.3: Partial decay widths of $W^\pm$ bosons using CKM elements determined by the unitarity constraint (Table 2.8) and values of other important parameters used in calculations. Values are taken from [11] and [23]

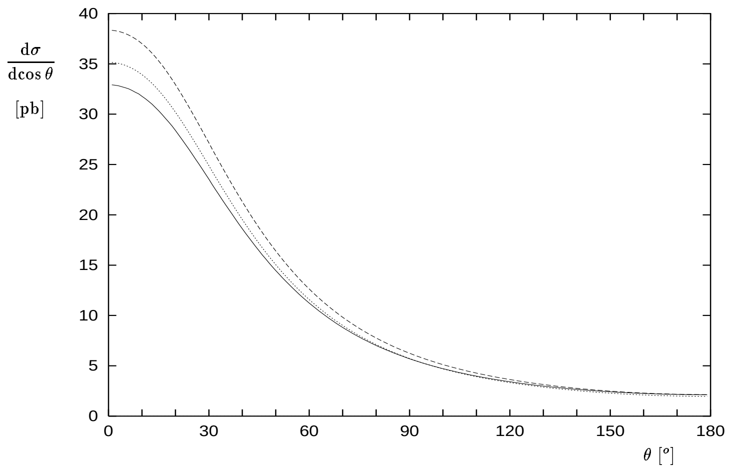

Figure 2.2: The expected differential cross-section $d\sigma_{WW}/d\cos\theta_{W^-}$ for various approximations at the center of mass energy of 190 GeV. The dashed curve corresponds to the on-shell Born approximation, the dotted one to the off-shell Born approximation, and the solid one to the full first order electroweak corrections. The polar angle of W^- bosons θ_{W^-} is defined with respect to the direction of the electron beam. The figure is taken from [23].

2.2.2 Corrections to leading order diagrams

So far we have considered only two leading order diagrams for the $W^{\pm}$ pair production. (Fig. 2.1). There are also higher order diagrams that contribute to the $W^{\pm}$ pair production as well as diagrams leading to additional photons in the final state. Apart from the $W^{\pm}$ pair production, a number of other processes leads to the same four-fermion final state. In principle, the matrix elements of all processes producing the same final state have to be summed up coherently in order to account for interferences. It is conventional to write the four-fermion cross-section $\sigma_{f_1\bar{f}_2f_3\bar{f}_4}$ for the reaction $e^+e^- \to f_1f_2f_3f_4(+\gamma, g, ...)$ as follows:

$$\sigma_{f_1\bar{f}_2f_3\bar{f}_4} = \sigma_{WW\to f_1\bar{f}_2,f_3\bar{f}_4} + \sigma^{bkg}_{f_1\bar{f}_2f_3\bar{f}_4}, \tag{2.15}$$

where

$$\sigma_{WW\to f_1\bar{f}_2,f_3\bar{f}_4} = \sigma^0_{WW\to f_1\bar{f}_2,f_3\bar{f}_4} \cdot (1 + \delta^{EW}_{f_1\bar{f}_2,f_3\bar{f}_4} + \delta^{QCD}_{f_1\bar{f}_2,f_3\bar{f}_4}). \tag{2.16}$$

The set $f_1\bar{f}_2f_3\bar{f}_4$ represents any fermion combination possible in decays of $W^{\pm}$ pairs. In this way we defined $\sigma_{WW\to f_1\bar{f}_2,f_3\bar{f}_4}$ as the partial cross-section for the production of a given final state via the intermediate W^+W^- pair. Usually, $\sigma_{WW\to f_1\bar{f}_2,f_3\bar{f}_4}$ is referred as the CC03 cross-section. Other terms in Eq. 2.15 and Eq. 2.16 are the following:

- $\sigma^{\mathbf{0}}_{\mathbf{WW\to f_1\bar{f}_2,f_3\bar{f}_4}}$ is the Born off-shell contribution from the leading order CC03 diagrams given by Eq. 2.9. Interactions between fermions that are coming from the same $W^{\pm}$ boson are embedded in the calculations of the partial decay widths discussed in Section 2.2.1.

- $\delta^{\mathbf{EW}}_{\mathbf{f_1\bar{f}_2,f_3\bar{f}_4}}$ are higher-order electroweak corrections including loop corrections, real photon emission off the initial and final state, electroweak interconnection phenomena, etc. The largest effect is expected to arise from the Coulomb interaction and the radiation of a photon off the initial state (ISR). The Coulomb interaction incorporates exchange of a virtual photon between two $W^{\pm}$ bosons. It leads up to a 6% correction of the cross-section ([23]). The correction is more important close to the threshold center of mass (CMS) energy where the $W^{\pm}$ bosons are slow, hence the probability of exchanging a photon is larger. A significant correction of about 20% is expected from the radiation of photons from the incoming electron or positron. The average photon energy is about 1 GeV. All effects discussed so far are factorisable in the sense that they do not depend on the type of fermions in the final state. However, there are also interconnection processes where a photon connects fermions coming from different $W^{\pm}$ bosons, initial and final state fermions, or a $W^{\pm}$ boson to fermions from another $W^{\pm}$ boson. In general, these corrections depend on the final state. They are estimated to be of the relative order $\alpha\Gamma_W/M_W \sim 0.02\%(\alpha \sim 1/137)$ [23]. In the analysis they are neglected.

- $\delta^{\mathbf{QCD}}_{\mathbf{f_1\bar{f}_2,f_3\bar{f}_4}}$ are the QCD corrections not included in the decay widths. They are due to an interconnection between quarks and gluons from different $W^{\pm}$ bosons. Therefore, they are relevant only for the fully hadronic final state. The corrections are divided into a perturbative and a non-perturbative part. The perturbative part changes the cross-section by about $\alpha_s^2/(N_C^2 - 1) \sim 0.2\%$ [23]. The change is well below the anticipated experimental precision, thus neglected.

  The non-perturbative part of interconnection is not expected to change the overall cross-section. However, it can alter some of event shape variables. There are essentially two types of interconnection phenomena: the colour reconnection and the Bose-Einstein correlation. The colour reconnection stems from the fact that an average space-time distance between the decay vertices of different $W^{\pm}$ bosons amounts to 0.1 fm, while the typical scale of hadronisation process is 1 fm. A gluon of fairly low energy, $E_g \lesssim \Gamma_W$, can fill the colour field of all four quarks and their fragments. Hence, fragmentation of the W^+ and W^- bosons may not be independent. The colour reconnection can affect several observable quantities. It can, for example, lead to distorted energy spectra of particles and changed ratios of different hadron types. Several models have been proposed often leading to contradictory predictions [41, 42, 23]. Some of scenarios have been rejected already by dedicated measurements that have not resulted in any significant effects [39]. These measurements mostly rely on a comparison of event shape variables and momentum spectra of identified particles between events in which both $W^{\pm}$ bosons decay into quarks to those where only one $W^{\pm}$ boson decays hadronicaly.

  Another type of interconnection is the Bose-Einstein correlation between hadrons coming from different $W^{\pm}$ bosons. Here, an enhancement of identical (like-signed) pions with small differences between their momenta is expected. The Bose-Einstein correlation is phenomenologically adopted in many simulation models that describe the process of hadronisation and formation of jets [44]. The predicted effects are usually of the same order as those from the colour reconnection. To test existence of the Bose-Einstein correlation event shape variables between interactions $W^+W^- \to q_1\bar{q}_2q_3\bar{q}_4$, $W^+W^- \to q_1\bar{q}_2\nu l$, and hadronic decays of Z^0 bosons were compared. So far, no significant effects have been observed for hadrons coming from different $W^{\pm}$ bosons [40, 45, 46].

- $\sigma^{\mathbf{bkg}}_{\mathbf{f_1\bar{f}_2f_3\bar{f}_4}}$ includes contributions of all non-W^+W^- diagrams that lead to the same

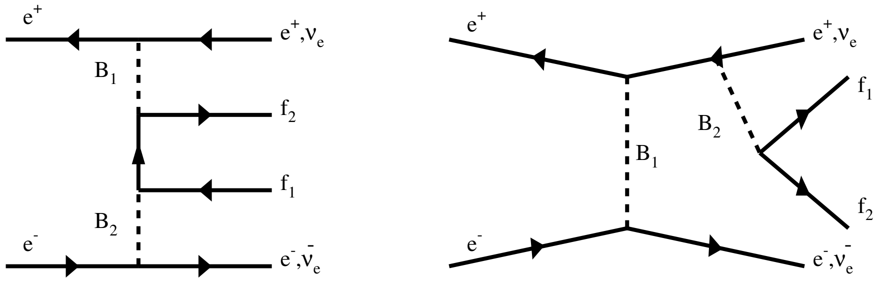

Figure 2.3: Two types of four-fermion processes. B_1 and B_2 stand for $W^{\pm}$, Z^0 or γ.

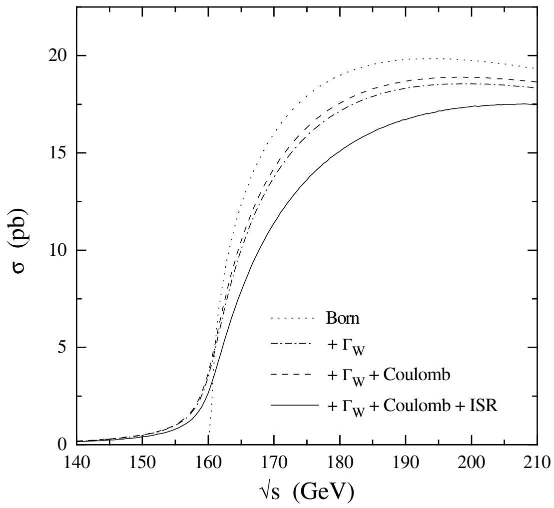

Figure 2.4: The expected cross-section σ_{WW} as a function of the CMS energy in various approximations: Born on-shell cross-section, Born off-shell cross-section, including Coulomb corrections, and initial state radiation (ISR). Figure is taken from [24].

four-fermion final states as well as their interferences with the W^+W^- diagrams [37, 35, 36]. As an illustration, two types of these processes are shown in Figure 2.3. We will discuss this subject in more details in Section 6.2.3 devoted to the cross-section measurement.

All corrections, apart from the colour reconnection and the Bose-Einstein correlation, are calculated with a satisfactory precision of generally less than 1% relative uncertainty. The simulated total cross-section σ_{WW} as a function of the CMS energy is shown in Figure 2.4.

2.3 Measurement of $|V_{cs}|$ at LEP2

In the LEP2 environment, there are essentially three measurable quantities that depend on the value of $|V_{cs}|$. These are: the total W^+W^- production cross-section σ_{WW}, the hadronic branching ratio of $W^\pm$ bosons $Br_{W\to had}$, and the fraction of $W \to cs$[1] decays in the hadronic $W^\pm$ decays (r_{cs}). All three quantities can be expressed by the partial decay widths of $W^\pm$ bosons. As we do not want to imply the unitarity constraint the measured values of CKM elements ($|V^{meas}_{f_if_j}|$) are used to calculate the hadronic partial decay widths:

$$\Gamma_{W\to f_if_j} = \frac{|V^{meas}_{f_if_j}|^2}{|V^0_{f_if_j}|^2} \cdot \Gamma^0_{W\to f_if_j}, \tag{2.17}$$

where $|V^0_{f_if_j}|$ are the values of CKM elements determined by the unitarity constraint and $\Gamma^0_{W\to f_if_j}$ are the corresponding decay widths (see Table 2.3). In the following we will describe the main features and sensitivity of each of the three quantities that depend on the value of $|V_{cs}|$:

- $\mathbf{Br_{W\to had}}$ is by definition related to the partial decay widths and consequently to $|V_{cs}|$ as follows:

$$Br_{W\to had} = \frac{\Gamma_{W\to cs} + \sum_{q_iq_j,\, q_iq_j\neq cs} \Gamma_{W\to q_iq_j}}{\Gamma_{W\to cs} + \sum_{q_iq_j,\, q_iq_j\neq cs} \Gamma_{W\to q_iq_j} + \Gamma_{W\to lept}}. \tag{2.18}$$

  In above expression the universality of lepton families is assumed. The uncertainty of α_S needed to fix the ratio between the leptonic and the hadronic decay widths is well below the predicted statistical precision of the measurement. The measured value of the hadronic branching ratio can be obtained from the measured partial cross-sections for the production of $W^\pm$ pairs decaying in three main channels: hadronic ($WW \to qqqq$), mixed ($WW \to qql\nu$) and leptonic ($WW \to l\nu l\nu$). In Section 2.2.2 we showed that the higher order corrections to the cross-section $\sigma^0_{WW\to f_1\bar{f}_2f_3\bar{f}_4}$ (Eq. 2.16) practically do not depend on the final fermion state. Under this assumption we can write (Eqs. 2.16, 2.9 and 2.18):

$$\begin{aligned} \sigma_{WW\to qqqq} &= \sigma_{WW} \cdot Br^2_{W\to had}, \\ \sigma_{WW\to qql\nu} &= 2\sigma_{WW} \cdot Br_{W\to had} \cdot (1 - Br_{W\to had}), \\ \sigma_{WW\to l\nu l\nu} &= \sigma_{WW} \cdot (1 - Br_{W\to had})^2. \end{aligned} \tag{2.19}$$

  The dependence of the partial and the total cross-section as a function of $|V_{cs}|$ is shown in Figure 2.5.

[1]Throughout the thesis the states without specified charges imply all physically allowed combinations (i.e. $W \to cs = W^+ \to c\bar{s}$ and $W^- \to \bar{c}s$).

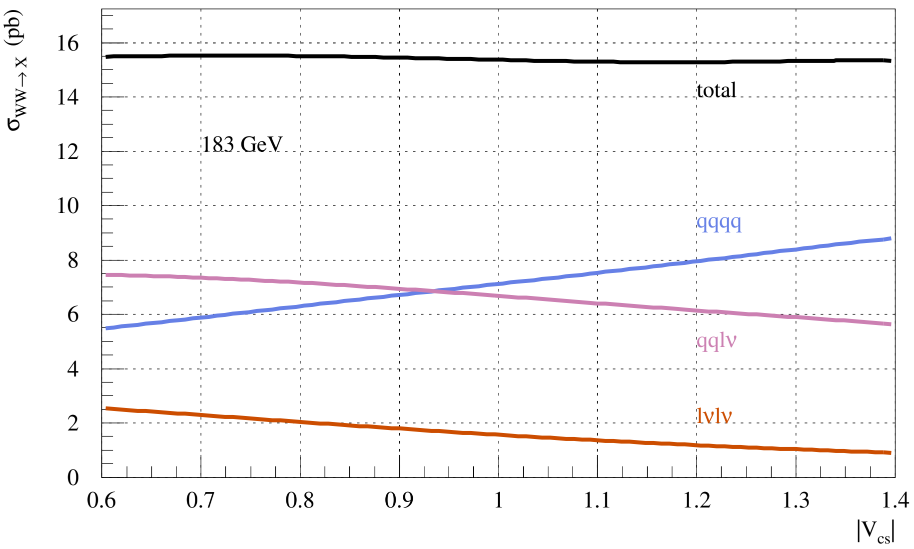

Figure 2.5: The expected partial cross-sections for W^+W^- production at 183 GeV as a function of $|V_{cs}|$ for the main decay modes.

- $\mathbf{r_{cs}}$ is expressed by the partial decay widths as follows:

$$r_{cs} = \frac{\Gamma_{W\to cs}}{\Gamma_{W\to cs} + \sum_{q_i q_j,\, q_i q_j \neq cs} \Gamma_{W\to q_i q_j}}. \tag{2.20}$$

  The value of $|V_{cs}|$ derived from r_{cs} is more direct than the one obtained from $Br_{W\to had}$ since we do not need any assumption about the leptonic decay widths. Still we have to assume the measured values of non-cs hadronic decay widths. For the measurement of r_{cs} we need a separation of cs di-jets from other flavour combinations in the hadronic decays of $W^\pm$ bosons.

- $\sigma_{\mathbf{WW}}$ as a function of $|V_{cs}|$ is calculated numerically by the integration of Eq. 2.9. The dependence of σ_{WW} on the value of $|V_{cs}|$ is presented in Figure 2.5. Since the dependence is very weak, the total cross-section was not used to measure $|V_{cs}|$.

2.4 Other processes at LEP2

In addition to the $W^\pm$ pair production, there are also other physical processes occurring at LEP2 [26]. Some of them may look similar to the W^+W^- events and can not be fully separated from them. Processes that lead to the same four-fermion final states even interfere with the W^+W^- production diagrams. In the analysis we considered the following background processes:

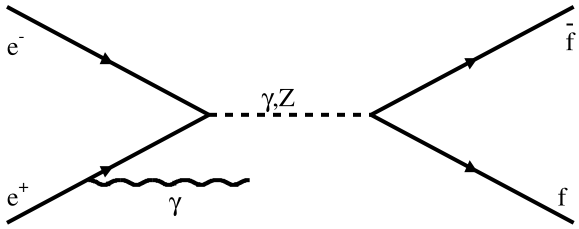

Figure 2.6: The Feynman diagram for the process $e^+e^- \to Z^0(\gamma) \to q_i\bar{q}_i(\gamma)$.

- $e^+e^- \to Z^0(\gamma) \to q_i\bar{q}_i(\gamma)$ proceeds via an intermediate real or virtual Z^0 boson or a photon [27]. In the literature, the process is usually referred as the QCD event. In about 70% of QCD events an energetic photon is emitted off the initial electron-positron state. The remaining e^+e^- CMS energy is likely to equal the Z^0 mass. The Feynman diagram for this process is shown in Figure 2.6. The cross-section for QCD events is approximately proportional to $1/s$. At the center of mass energy of 183 GeV it amounts to about 100 pb. This value should be compared to the expected cross-section for $W^\pm$ pair production which amounts to about 16 pb at the same energy. In the case where one or two quarks emit a hard gluon, the QCD event may look very similar to a W^+W^- event which decays hadronicaly.

- $e^+e^- \to Z^0(\gamma) \to \mu^+\mu^-(\gamma)$, $\tau^+\tau^-(\gamma)$ production is similar to QCD events except that leptons are produced instead of quarks. These events are of the main importance as a possible background source in the leptonic decays of W^+W^- pairs. The cross-section at the center of mass energy of 183 GeV is 9.91 pb and 8.74 pb for the μ and τ channel, respectively. At the same time, the expected cross-section for the leptonic decays of W^+W^- pairs is about 1.5 pb.

- $e^+e^- \to e^+e^-(\gamma)$ (Bhabha scattering) proceeds either trough the s-channel as for the μ or τ production or trough the t channel. The latter has a much larger cross-section of around 12000 pb. The bulk of outgoing leptons peaks at small angles with respect to the beam axis and is relatively easy removable.

- $e^+e^- \to Z^0Z^0(\gamma\gamma)$ is a process similar to the W^+W^- production. Fortunately, the cross-section of 1.34 pb at the CMS energy of 183 GeV is small compared to the one for the $W^\pm$ pair production.

- $e^+e^- \to Z^0e^+e^-, We\nu$. The cross-section for Z^0 production is 6.81 pb at the CMS energy of 183 GeV while it is about one order of magnitude smaller for the single

$W^{\pm}$ production. The two processes lead to the same final states as the $W^{\pm}$ pair production, too.

- $e^+e^- \rightarrow \gamma\gamma e^+e^-$ where two virtual photons emitted from the initial e^-e^+ system interact and produce few hadrons [28]. The cross-section is comparable with the one for the Bhabha scattering. However, the center of mass energy of the $\gamma\gamma$ system is in most cases small and boosted along the beam direction. Such events can be relatively easy rejected.

- In addition to the above processes, we considered also the Compton scattering and the production of $e^+e^-e^+e^-$. The two were found to be of little importance as background sources.

3

The LEP Collider and the DELPHI Detector

3.1 The LEP Collider

The Large Electron Positron collider LEP is located at the European Laboratory for Particle Physics near Geneva. Being mounted in a ring of 26.7 km circumference makes the LEP collider [54] the biggest accelerator in the world. It is positioned in the tunnel about 100 m underground and was constructed between 1983 and 1989. The tunnel was excavated from alternate straight and bent sections.

Electrons and positrons are injected into the LEP ring with an energy of 20 GeV. Before the beams are injected into LEP they are pre-accelerated at several stages (Figure 3.1). Electrons from the electron gun and positrons from the tungsten electron converter are first accelerated to 600 MeV in the two linear accelerators followed by an electron-positron accumulator which injects the particles into the CERN Proton Synchrotron (PS). At the energy of 3.5 GeV particles are passed over from the PS into the CERN Super Proton Synchrotron (SPS). In the SPS beams are accelerated to 20 GeV and then injected into LEP. In eight bent sections the electron and positron beams are kept in orbit by more then 5000 dipole, quadrupole, sextupole, and other correction magnets. In the straight sections beams are accelerated to the desired energy using RF cavities. Once the desired energy is reached the LEP is operating as a storage ring. A typical lifetime of the stored beam is about 10 hours. In this phase cavities are used to compensate for energy losses due to the synchrotron radiation. The energy loss is proportional to E^4/r with r being the radius of the LEP ring and E the beam energy. Since 1996 about 200 cooper cavities have been replaced by super-conducting ones to achieve higher energies without significant increase in power consumption.

Four multipurpose detectors L3, ALEPH, OPAL, and DELPHI are located in every second straight section. The electron and positron beams coming from opposite directions

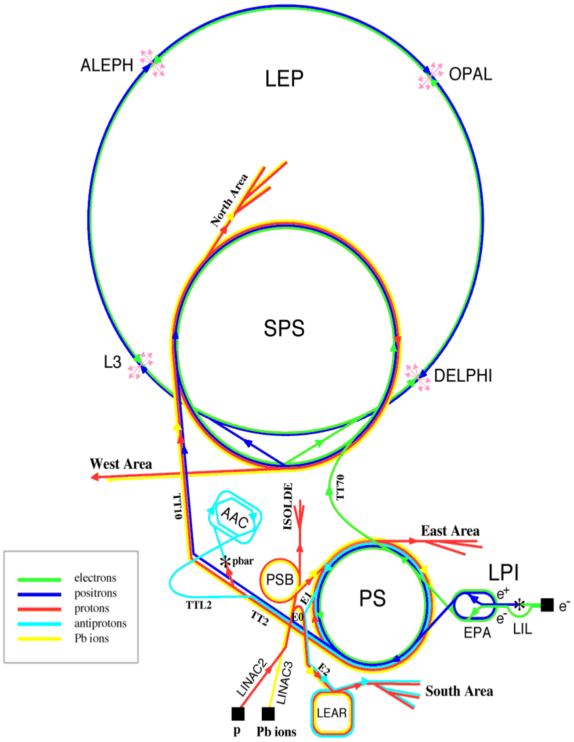

Figure 3.1: The LEP accelerator chain.

are tightly squeezed and brought together in center of the detectors in order to achieve high luminosities. Luminosity $\mathcal{L}$ as one of crucial parameters of an accelerator is defined as:

$$\nu = \sigma \mathcal{L},$$

with ν being the expected event rate of a physical process with the cross-section σ. The luminosity depends on machine parameters in the following way:

$$\mathcal{L} = f_{rev} \cdot k \cdot \frac{N^+ \cdot N^-}{4\pi \cdot \sigma_x \cdot \sigma_y}.$$

Hereby, f_{rev} is the LEP revolution frequency of about 11.25 kHz, k is the number of electron and positron bunches in the ring (4 or 8). $N^{\pm}$ is the number of positrons and electrons per bunch and amounts to about 2.5×10^{11}. $\sigma_y = 10\ \mu m$ and $\sigma_x = 50\ \mu m$ are dispersions of the beam in the vertical and the radial direction, respectively. Beams are focused to these dimensions by a set of quadrupole magnets located in front of the detectors.

From 1989 to 1995 collisions took place at the CMS energy of about 90 GeV. At this energy about 4 million Z^0 decays were collected by each detector. The LEP2 phase started in 1996 with the beam energy risen to 81 GeV and 86 GeV later in the year. In 1997 the beam energy was further increased to about 91.6 GeV. The beam energy was measured using resonant depolarisation for an absolute calibration at lower energies and nuclear magnetic resonance to extrapolate to higher energies [53]. The achieved resolution of the CMS energy is about 60 MeV. The integrated luminosity delivered in the two years is about 25 pb^{-1} and 64 pb^{-1}, respectively. The peak luminosity commonly exceeded 10^{31} $\mathrm{cm}^{-2}/\mathrm{s}$. At the beginning of each year and in the middle of the year 1996 beams were accelerated to 45 GeV in order to collect Z^0 decays used for various calibrations of detectors. In the two years about 40000 and 80000 Z^0 events were collected, respectively.

3.2 The DELPHI Detector

The DELPHI (**De**tector with **L**epton, **P**hoton and **H**adron **I**dentification) detector is one of four detectors used to detect products of e^+e^- collisions at the LEP collider. It is a general purpose detector with the emphasis on a high tracking efficiency and accuracy, good calorimeter performance and particle identification capabilities over an almost full solid angle. A detailed description of the DELPHI detector and its performance can be found elsewhere [55, 56].

As illustrated in Figure 3.2, DELPHI consists of a central barrel region and two forward end-caps on each side. A 5.2 cm radius Beryllium beam-pipe runs along the cylinder's axis. Collisions are taking place in the center of the cylinder. The detector has an overall length and diameter of over 10 m and weighs 3500 tons. The coordinate system of the DELPHI detector is defined as follows: z axis points along the electron beam, x axis points towards the center of the LEP ring, and consequently, y axis point towards the ground. Often, cylindrical or spherical coordinates will be used. They are defined in the standard manner with respect to the cartesian system. In the following we will briefly describe some technical properties and principal aims of all sub-detectors mounted into the DELPHI detector.

3.2.1 Tracking sub-detectors

The purpose of tracking sub-detectors is detection of trajectories of charged tracks. When a charged particle such as $e^{\pm}, \mu^{\pm}, K^{\pm}, \pi^{\pm}$ or p travels through the detector material it produces free charge carriers around its path. Detection and positioning of the produced charge is the primary task of tracking sub-detectors. They should contain as little material as possible in order not to disturb significantly the original trajectory of particles. The main features of DELPHI tracking sub-detectors are summarised below.

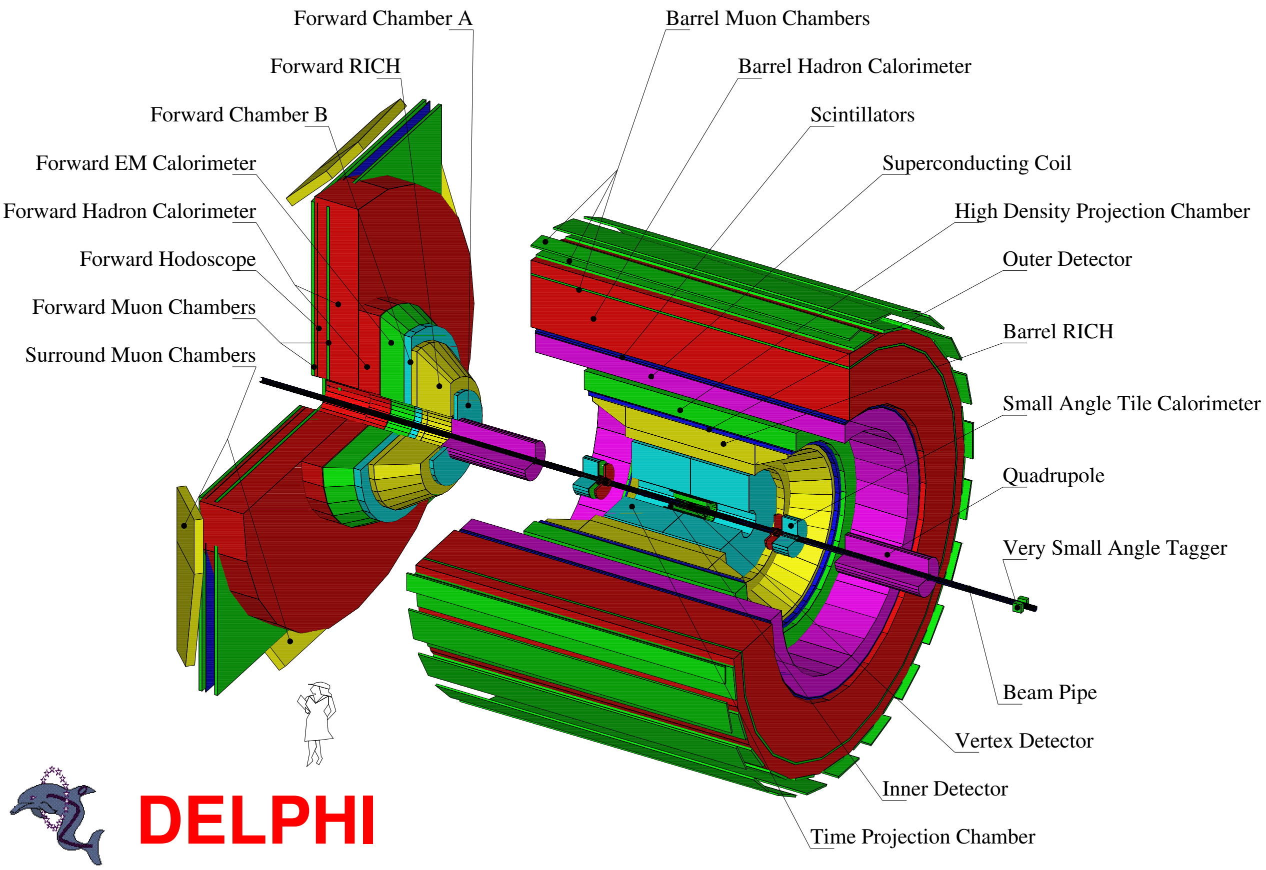

Figure 3.2: A shematic view of the DELPHI detector.

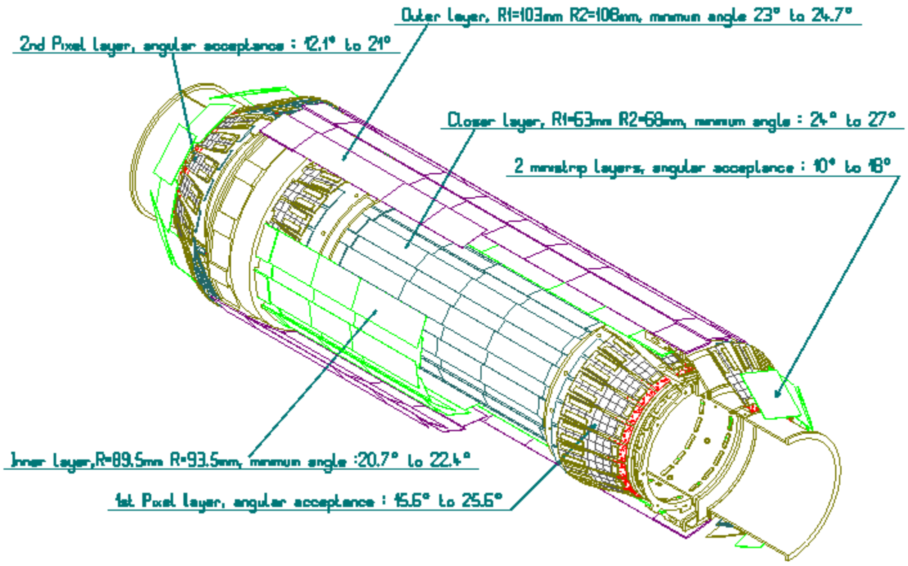

Figure 3.3: A shematic view of the Vertex Detector and the Very Forward Tracker.

Vertex Detector (VD)

The Vertex Detector consists of three coaxial cylindrical layers of silicon strip detectors at radii of 6.3, 9.0 and 10.9 cm. Since an upgrade in 1996 the sub-detector covers the polar angle from about 25^0 to 155^0 [59]. One side of a layer has strips arranged parallel and the other side concentric with respect to the beam axis. Strips are spaced at 25 μm intervals along z axis and somewhat larger non- equidistant intervals in the $R\Phi$ direction. The achieved resolution in one layer is about 8 μm in the $R\Phi$ plane and maximum of 9 μm in the z direction when the track is perpendicular to the z axis.

Very Forward Tracker (VFT)

The sub-detector consists of two layers of silicon strip and two layers of silicon pixel detectors. The layers are tiled with respect to the beam axis so that particles penetrate approximately perpendicular trough them. The ministrips have a 100 μm pitch while the dimension of pixels is 330×330 μm. The aim of the VFT is to improve the tracking efficiency and resolution in polar angles between 10^0 to 25^0 and 155^0 to 170^0. The complete Silicon tracker that includes the VD and the VFT is shown in Figure 3.3.

Inner Detector (ID)

The 1 m long Inner Detector is situated along the VD at radii between 12 cm and 28 cm. It consists of a Jet Chamber surrounded by 5 cylindrical Multi-Wire-Proportional-Chambers (MWPC). The Jet Chamber is divided into 24 sectors filled with the drift gas.

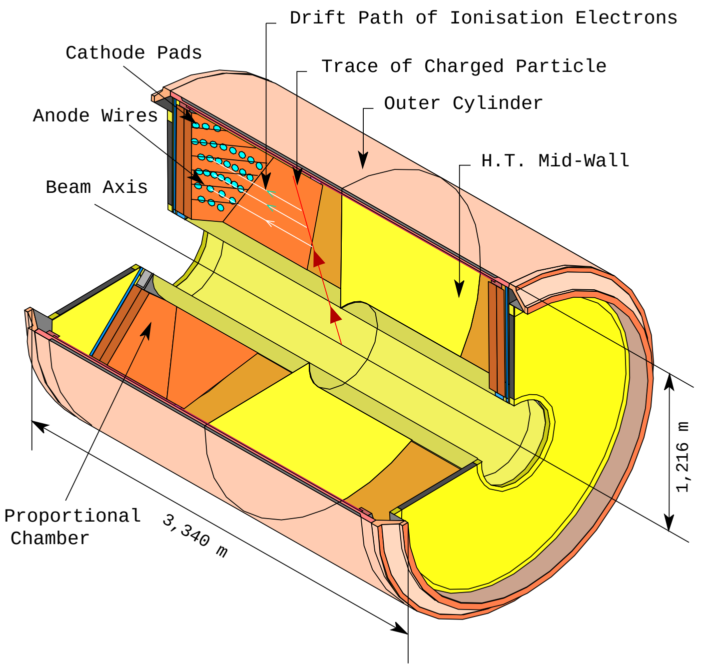

Figure 3.4: A shematic view of the DELPHI TPC

Each sector contains 24 anode wires radially mounted in a row and stretched along z, thus providing $R\Phi$ positioning. The single wire resolution for isolated tracks is about 50 μm in the $R\Phi$ plane. Every MWPC layer consists of 192 sense wires and 192 field-shaping wires spaced by about 8 mm in the $R\Phi$ plane. MWPC is mostly used for fast triggering and for resolving a left-right ambiguity of the Jet Chambers.

The Time Projection Chamber (TPC)

The TPC is the main tracking device in the DELPHI. It extends in radius from 29 to 122 cm and is 334 cm long (Figure 3.4). The two drift volumes are separated in the center of the detector by a high voltage plate producing an electric field of 150 V/cm. A charged particle crossing the TPC produces around 70 electrons per cm of gas (80% Ar + 20% methane). In the presence of the electric field produced electrons drift to the MWPC's at each side of the sub-detector. The MWPC's are segmented in Φ in 60^0 sectors having 192 radially stretched anode wires and 16 concentric cathode rows. The z direction of produced ion pairs is determined by the timing of electronic pulses. For this purpose the drift velocity is permanently measured with a relative uncertainty of 2×10^{-4}. The single wire resolution is about 250 μm in the $R\Phi$ and 880 μm in the Rz plane. The specific ionisation of particles (dE/dx) is obtained from the distribution of charges collected on the sense wires.

Outer Detector(OD)

The Outer Detector lies between the barrel RICH and the electromagnetic calorimeter (described later) at radii 197 cm to 206 cm. It is essential to improve the momentum resolution of fast particles. It consists of 5 layers of drift tubes, operated in the limited streamer mode. All layers provide $R\Phi$ measurement with the precision of 110 μm. Three layers enable also measurement of the z position by timing the signals at the ends of the anode wires. The precision is about 3.5 cm.

Forward Chamber A (FCA)

Three modules of FCA are mounted on each end of the TPC. They cover polar angles between 11^0 and 32^0. One module consists of 2 planes of drift tubes, operated in the limited streamer mode. Each plane of wires is rotated by 120^0 with respect to the previous set. The single wire resolution is about 190 μm in the $R\Phi$ plane.

Forward Chamber B (FCB)

The FCB is a drift chamber at an average distance $|z| = 275$ cm from the interaction point. The chamber consists of 2 modules of 12 readout planes of wires. Again, each wire plane is rotated by 120^0 to the previous one. Single wire residuals have an average of 300 μm.

The Solenoid

The tracking system, together with the RICH counters and the electromagnetic calorimeter, is enclosed within the super-conducting solenoid which is 7.4 m long and has a diameter of 5.2 m. The solenoid generates a magnetic field of 1.2 T along the z axis. The relative inhomogenity of the magnetic field is of the order of 10^{-4}. Bending of charged tracks in the magnetic field enables measurement of particle momenta.

3.2.2 Calorimetry

Calorimeters are used to measure the energy of particles. Therefore, particles should deposit all their energy in calorimeters.

Electromagnetic Calorimeters

Photons should not interact in the tracking sub-detectors. They will convert into an electron-positron pair only in presence of a dense material of which the electromagnetic calorimeters consist. The produced electrons and positrons lead to new photons via bremsstrahlung. The new photons in turn again convert into e^+e^- pairs. This cascade process leads to a shower of low energy photons and electrons that deposit their energy by the ionisation, absorption, and other reactions with the material. A shower similar to that of photons is produced also by electrons. Other particles escape the electromagnetic calorimeters by loosing only a small fraction of their energy by the ionisation or strong interactions.

High Density Projection Chamber (HPC)

The barrel electromagnetic calorimeter consists of 144 modules arranged in a cylindrical layer. Each module is a small TPC with lead layers separated by gas gaps. The lead plates serve as converters and simultaneously provide the drift field. The total converter thickness is 18 absorption lengths of photons. Proportional wire chambers at the edge of the drift volume enable a three dimensional reconstruction of produced charge. For fast triggering purposes, a plane of scintillators is inserted into one of the HPC sampling gaps. The energy calibration is performed by using reconstructed π^0 mesons from $\pi^0 \to \gamma\gamma$, converted photons from $\gamma \to e^+e^-$, and electrons from $Z^0 \to e^+e^-$. The relative precision of the measured energy (E) is:

$$\sigma(E)/E = \sqrt{0.043^2 + 0.33^2/E(\mathrm{GeV})}.$$

The angular precision of the point of photon incidence is about 1 mrad in the azimuthal direction and 1.7 mrad in the polar angle.

Forward Electromagnetic Calorimeter (FEMC)

The FEMC is built up by 4532 lead glass blocks covering the polar angles from 8^0 to 35^0 and 172^0 to 145^0. Charged particles inside the electromagnetic showers emit Čerenkov photons. The produced Čerenkov light is read-out by photomultipliers for each block separately. The sub-detector is calibrated with Bhabha events. The achieved relative precision of the measured energy can be parametrised as:

$$\sigma(E)/E = \sqrt{0.03^2 + 0.12^2/E(\mathrm{GeV})}.$$

Small Angle Tile Calorimeter (STIC)

STIC is a sampling lead-scintillator calorimeter placed on either side of the DELPHI detector at the distance of 220 cm from the interaction point [57]. It covers polar angles between 29 mrad and 185 mrad. Each side consists of 47 lead-scintillator layers placed in the $R\Phi$ plane. The light is collected with 1600 wavelength shifting optical fibres threaded through the layers. Additional two layers of scintillator planes are placed in front of the calorimeter to enable separation between charged and neutral particles. The relative energy resolution for a particle of 45 GeV energy is 2.7%.

Hadron Calorimeter (HCAL)

Neutral hadrons interact only via the strong interaction with nuclei in the material. Their average free path in the iron is about 18 cm. Therefore, hadrons mostly escape the electromagnetic calorimeter unobserved. The HCAL is installed in the iron return yoke of the DELPHI Solenoid. It covers almost the full solid angle from 11^0 to 169^0. The calorimeter consists of 20 layers of limited streamer tubes sandwiched between 5 cm iron plates. In total, there are more than 19000 streamer tubes varying in length between 40 to 410 cm. The standard calorimetry relies on the signal read-out from cathodes of individual streamer tubes. The energy calibration at LEP2 mostly relies on charged hadrons associated with showers in HCAL. The relative energy resolution is found to be:

$$\sigma(E)/E = \sqrt{0.21^2 + 1.12^2/E(\mathrm{GeV})}.$$

3.2.3 Muon chambers

Muon as much heavier leptons than electrons loose their energy mainly by the ionisation in the material and can therefore escape even the hadron calorimeter. To detect and identify these muons the Muon chambers are installed behind the hadron calorimeter.

Barrel (MUB) and Forward (MUF) Muon Chambers

The sub-detector MUB consists of three layers divided into 24 azimuthal sectors. The inner most layer lies 20 cm inside HCAL. Each layer consists of a number of drift tubes arranged in two planes. The electric field is produced between the central anode wire and cathode strips that run along z at the surface of the drift chamber. The $R\Phi$ position is determined by the timing of the signal on the anode wire. One of the cathode strips is used as a delay line, thus providing the z co-ordinate of the track passage.

The MUF consists of two detection layers of drift chambers operating in the limited streamer mode.

Gaps between MUB and MUF at around 45^0 are covered by one layer of Surrounding Muon Chambers (MUS). In this way, the complete muon detection system covers polar angles between 20^0 and 160^0.

3.2.4 Ring Imaging Čerenkov Detectors (RICH)

A charged particle traveling through a medium with a velocity higher than the velocity of light in that medium emits Čerenkov photons. Microscopically, the emission of Čerenkov photons is a consequence of a coherent polarisation of media around the charge moving faster than the speed of light in the given medium. The Čerenkov angle θ_C, as the angle between the Čerenkov photon and the direction of the particle, is given by:

$$\cos\theta_C = \frac{1}{\beta n}, \tag{3.1}$$

with n being the refractive index of the medium and $\beta = v/c$. Given momentum of the particle and the Čerenkov angle one can calculate the mass m of the particle using the relation $m^2 = (p/c)^2(1-\beta^2)/\beta^2$. The calculated mass can then be used to distinguish between different particles [70]. As β approaches unity, the Čerenkov angle converges to a maximal value θ_C^{max}:

$$\theta_C^{max} = \arccos(1/n).$$

Once the difference in the expected angles between two particles of different masses is smaller than the resolution of the measured Čerenkov angle the separation becomes impossible. Therefore, there is a certain momentum window in which particles of different masses can be separated in a given medium.

The number of emitted photons per unit length L and unit energy of photons E_C is given by:

$$\frac{d^2N_{ph}}{dL(\mathrm{cm})dE_C(\mathrm{eV})} = 370\cdot\sin^2\theta_C. \tag{3.2}$$

Since the number of emitted photons depends on the Čerenkov angle, it can be used as an additional information to identify particles of different masses. Practically, photons are available only in the energy spectrum from about 1 eV to 10 eV. Photons of lower energy are difficult to detect while those of higher energies will be absorbed in the media before detected. Another important factor that limits the energy window is the chromatic dispersion of the refractive index.

The Barrel and the Forward RICH counters

The DELPHI RICH counters consist of a barrel (BRICH) and a forward (FRICH) part. The barrel part is placed next to the TPC at radii between 123 cm and 196 cm. The FRICH is sandwiched between the FCA and the FCB. Together they cover polar angles from 15^0 to 165^0 with about 5^0 gaps around 45^0 and 135^0. Each side of BRICH is divided into 24 identical sectors in $R\Phi$. The forward region is divided into 12 sectors in $R\Phi$ on

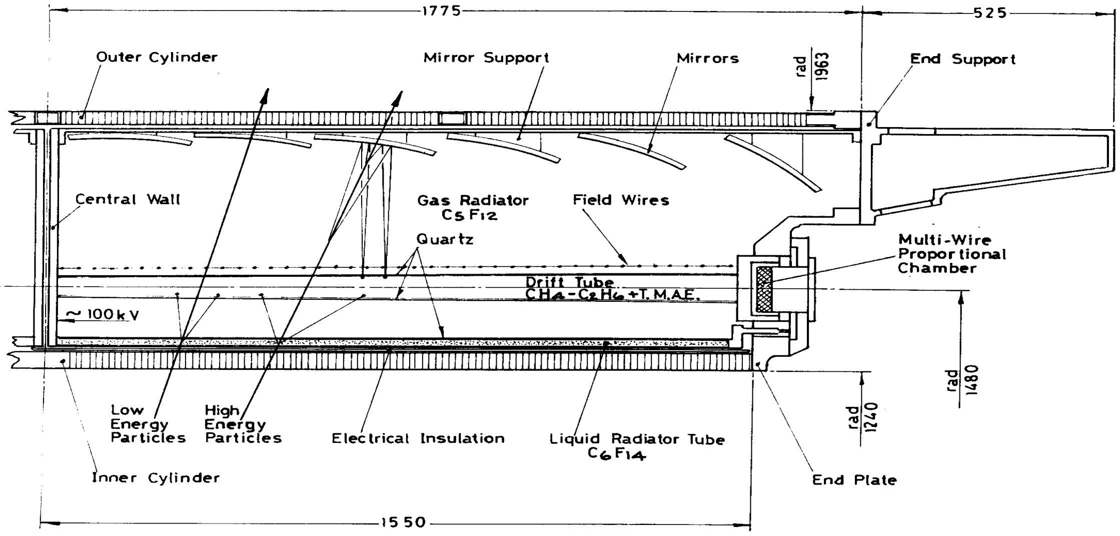

Figure 3.5: A side view of the barrel RICH sector.

each side. A shematic view of the barrel and the forward RICH sector is illustrated in Figure 3.5 and 3.6, respectively.

The RICH counters are designed for a charged particle identification in a wide momentum range between 0.7 GeV/c and 40 GeV/c [64]. Two radiator media, liquid and gaseous, are combined to achieve this [65].

The liquid radiator consists of a 1 cm thin layer of perfluorohexane (C_6F_{14}) in front of a quartz window. The refractive index of the liquid radiator is about 1.283 corresponding to the maximal Čerenkov angle of about 39^0. The radiators are placed in front of a 5 cm thick photon detector. The distance between the two systems is about 115 mm in the barrel region and 180 mm in the forward part. In the forward part, each sector consists of 3 boxes of liquid radiators.

The rest of the RICH volume is filled up by the gas radiator C_5F_{12} ($n = 1.00172$, $\theta_C^{max} = 3.36^0$) and C_4F_{10} ($n = 1.00155$, $\theta_C^{max} = 3.19^0$) in the barrel and in the forward part, respectively. The BRICH is kept at a constant temperature of 40^0 in order to prevent condensation of the gas radiator. The temperature of the FRICH is maintained only at around 30^0 because of a lower boiling temperature of C_4F_{10}. The average path length of particles in the gas radiator is 60 cm and 40 cm in the BRICH and FRICH, respectively. Focusing mirrors placed at the exit side of the sub-detector reflect photons radiated in the gaseous radiator back onto the photo-detection plane. Each sector in the barrel part consists of 6 parabolic mirrors mounted in a row along z. In the forward there are 5 spherical mirrors per sector. The refractivity of mirrors is about 90%. The shape

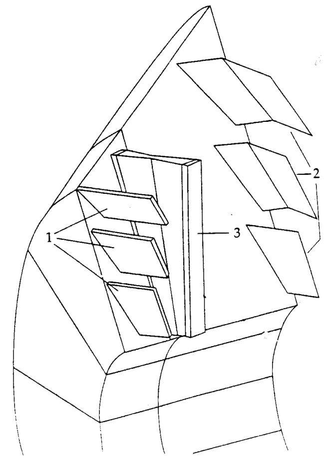

Figure 3.6: An illustration of the forward RICH sector: 1. liquid radiators, 2. mirrors, 3. photo-detector.

and the focal length of mirrors are chosen such that they focus parallel photons from the same particle approximately into the same point on the photo-detection plane (Figure 3.5). Therefore, photons emitted in the gas radiator are expected to be arranged in a ring on the photo-detection plane.

The photo-detector is a segmented TPC with UV graded quartz windows. In the barrel part the direction of the drift field of 0.35 kV/cm is parallel to the magnetic field. Homogenity of the field is assured by conductive strips on the quartz windows of drift boxes. The drift gas is a mixture of 75% methane and 25% ethane. It contains an admixture of TMAE used as a converter of photons with an energy above 5.64 eV into electrons. The upper bound of around 7.5 eV is set by the transparency of quartz windows and the gas radiator (Figure 3.7). An average quantum efficiency in this energy window is about 0.35. Produced photoelectrons are drifting along z towards MWPC's placed on each side of the barrel part. The chambers are equipped with an anode-wire and a cathode-strip readout (Figure 3.8). These in combination with the recorded drift time provides a 3D positioning of the photon-conversion point. The mean free path of photons in the photo-detector is about 18 mm. A smaller conversion depth with respect to the thickness of the photo-detector enables a separation between photons coming from the gas radiator and photons coming from the liquid radiator (Figure 3.5). The principle of the photo-detector in the FRICH is similar to the BRICH except for different geometry (Figure 3.6). In the FRICH the electrical field is perpendicular to the magnetic field. Therefore, there is the Lorentz angle of about 50^0 between the drift direction and the

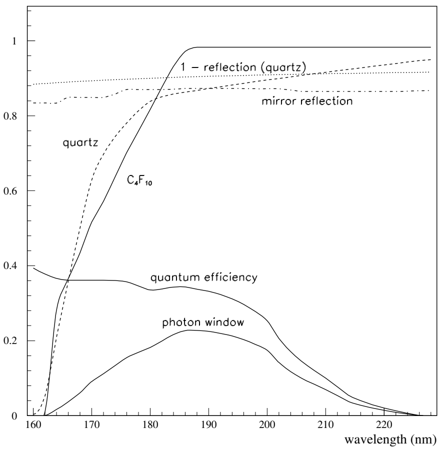

Figure 3.7: Transmission coefficients of photons emitted in the gas radiator in FRICH as a result of quantum efficiency of TMAE, transparency of C_4F_{10} and quartz window, reflection on the quartz surface, and mirror reflection.

	B. liquid	B. gas	F. liquid	F. gas
N_{photons}	14	9	6	6
$\sigma(\theta_C)$ (mrad)	13.5	4.5	11.4	2.6

Table 3.1: The number of associated photoelectrons per track and the resolution of measured Čerenkov angles for muons from $Z^0 \to \mu^+\mu^-$.

direction of the electrical field.

Monitoring [66] and a stable operation of all subsystems is of particular importance for a good data quality. All pressures are monitored and kept stable to ± 0.7 hPa. The temperature is also controlled and stabilised to about 0.2^0. The perfluorocarbons are recirculated after removal of oxygen and water vapour. Their transparency is measured by a monochromator. Because of a persistent leaking between the gas and the liquid radiators, the media are distilled in a distillation plant in order to keep the relative admixtures and thereby the refractive indices constant. Each photo-detector is equipped with a matrix of UV calibration fibres. UV light from a central lamp is distributed via quartz fibres that project the light onto the photo-detector at well defined spots. Thereby, the drift velocity can be calculated from a known z position of the photo-conversion and the drift time. The uncertainty of the drift velocity is smaller than 0.02%. The UV calibration lamps also serve for a measurement of the Lorentz angle.

All relevant parameters and changes are stored in the data base and are later used by the off-line reconstruction program of Čerenkov angles. Each detected photoelectron is associated to all tracks that result in a physically allowed Čerenkov angle. Though the

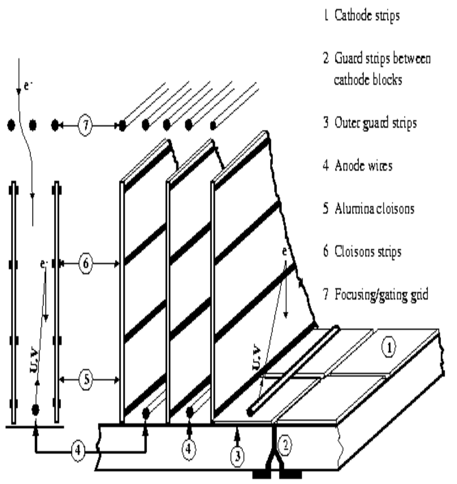

Figure 3.8: A shematic view of the MWPC in BRICH.

initial number of produced Čerenkov photons is relatively high (Eq. 3.2), the number of detected photons is only a small fraction of it. Some photons are absorbed in the radiators or totally reflected on the quartz surface. An important loss factor is the quantum efficiency of TMAE. Photoelectrons can further be absorbed in the drift gas or missed by the MWPC. The number of detected photons for isolated muons with momenta of 45 GeV/c is given in Table 3.1 together with the resolution of Čerenkov angles. There are various factors influencing the resolution: short time variations of the refractive index caused by pressure and temperature changes, chromatic dispersion of the refractive index, spread of the photon-emission point, deflection in the quartz, uncertainty of the track position, bending of tracks in the gas radiator, mirror imperfections and their geometry, uncertainty of the drift velocity, diffusion during drifting, field imperfections, resolution of MWPC's, electronic noise and alignment effects. A more detailed description of the off-line analysis of data from the RICH counters and methods used to identify particles will be given in Section 4.7.4.

3.2.5 Other sub-detectors

We will only briefly mention remaining sub-detectors as they are not of primary importance for the presented analysis.

- The Time of Flight (TOF) counters in the barrel part are scintillator detectors that provide fast triggering and rejection of cosmic rays. In the forward region scintillator Hodoscopes (HOF) serve for the same purpose.

- The Very Small Angle Taggers (VSAT) are calorimeters covering polar angle between 5 and 7 mrad. They are used for luminosity measurements.

- Cracks around 90^0 and 40^0 in the electromagnetic calorimeter are covered by supplementary photon taggers. Thus, an almost complete hermeticity of the detector is obtained.

3.2.6 Trigger

The DELPHI trigger system is composed of four successive levels of increasing selectivity [58]: T1, T2, T3 and T4. The first two trigger levels are synchronous with respect to the Beam Cross Over signal (BCO). With eight bunches in the storage ring the beam crossing interval is 11 μs. The trigger decisions T1 and T2 are taken 3 and 39 μs after the BCO signal, respectively.

T1 decision is supported by the sub-detectors with fast read-out times such as: ID, OD, FCA, FCB, TOF, HOF, MUB and HPC scintillators. The decision is taken on the basis of individual sub-detector information. Typical rate of T1 trigger is 700 Hz.

T2 verifies information also from the slow drift sub-detectors TPC, HPC and MUF and includes correlation from different sub-detectors. A positive T2 decision triggers the acquisition of data collected by the electronics. The trigger rate is typically 5 Hz.

T3 repeats the logic of T2 using more detailed detector information. This trigger halves the T2 rate.

T4 relies on the modified DELPHI tracking algorithm and reject events without tracks pointing to primary interaction point or significant energy deposits in the calorimeters. Its rate is approximately 1 Hz.

The trigger efficiency for multi-hadronic events as well as leptonic events is hardly distinguishable from 100%.

3.2.7 Data flow

The Data Acquisition System stores all events triggered at the T3-level as 'raw-data' and writes them to a disk or to a tape. The off-line data analysis is then used to perform the final reconstruction. The central component of this processing is the analysis program DELANA ([50]) that performs calibrations, pattern recognition, and track fitting. Some standard particle identification algorithms are also performed at this stage. The output of DELANA is a Data Summary Tape (DST). The information stored on the DST is used for specific physics analyses. For some of sub-detectors an additional fine tuning and calibration is performed at the level of the DST. This corrects for possible unexpected effects not taken into account during the production of DST.

4

General off-line analysis of data

4.1 Detector simulation

The DELPHI simulation package DELSIM ([48]) aims to produce simulated (Monte Carlo) data on the level of real raw data. The simulated data are then passed to the reconstruction program DELANA and to analysis programs in exactly the same way as the real data. They can be used to study the response of the DELPHI detector for a particular physical process. DELSIM is based on three main components: the event generator, the description of particle trajectory, and the detector response.

Event generators

Event generators [37] produce a full set of particles that result from a given physical process. An event generator consists of three main stages: the hard process, the parton shower, and the fragmentation of quarks and gluons into hadrons and their decay products. In our case, the main hard process is the reaction $e^+e^- \rightarrow W^+W^- \rightarrow f_1\bar{f}_2f_3\bar{f}_4$. To simulate the process, the matrix elements are used at the tree level. Corrections to the leading diagrams are usually difficult to express in a gauge invariant form. Therefore, in most of event generators, processes like the initial state radiation, gluon emission, etc., are added independently. This often leads to divergences that have to be considered carefully and require some cut-offs at small momenta and small angles.

For the presented analysis we have chosen PYTHIA/JETSET7.4 [32] as the main event generator for the W^+W^- events and background processes. The chosen generator is tuned to LEP1 data collected with the DELPHI spectrometer [47]. The emphasis of the selected generator is on the modeling of perturbative parton showers, non-perturbative fragmentation processes, and decays of unstable hadrons. Electroweak calculations are normally restricted to the improved Born level. They include the initial and the final state radiation of photons and the Coulomb interaction.

The fragmentation model used is the Lund string scheme. It is based on an iterative approach. Given an initial quark q_0, it is assumed that a new $q_1\bar{q}_1$ pair may be created, such that a meson $q_0\bar{q}_1$ is formed, and q_1 is left behind. This q_1 may at a later stage pair off with a $\bar{q}_2$ and so on. We have to provide relative probabilities to produce various flavour pairs $u\bar{u}, d\bar{d}, ...$, and relative probabilities that a given $q_{i-1}\bar{q}_i$ pair combination forms a specific meson. The relative probabilities for the creation of flavour pairs off the vacuum state are: $u : d : s : c \sim 1 : 1 : 0.3 : 10^{-11}$. They depend primarily on the quark masses. If a coloured $q_i\bar{q}_j$ pair is picked up by another quark $\bar{q}$, a baryon will be produced. Produced mesons and baryons may be unstable and will further decay into stable particles. Possible decay channels and their branching ratios are usually obtained in measurements. They are not always well known, in particular for hadrons composed of heavy quarks such as c and b. Polarisation of hadrons is in general not taken into account. The procedure of event generation is thus phenomenological and includes a number of other tunable parameters determined empirically. Features of resulting jets of particles are usually well described as far as inclusive quantities are concerned. However, for more exclusive and detailed studies one has to be aware of the above limitations and assumptions. For instance, the chosen event generator does not include interconnection phenomena like the Bose-Einstein correlation or the colour reconnection.

The generator PYTHIA/JETSET7.4 does not offer the possibility to calculate matrix elements of all four-fermion processes coherently. This is provided by the event generator EXCALIBUR [31] which was used to estimate possible systematic shifts due to neglected interferences. For cross-checks of the modeling of fragmentation process we used the ARIADNE [33] event generator that comprises a different model.

Description of particle trajectory

Particles arising from primary processes are passed trough all components of the DELPHI detector. The program is equipped with a detailed description of the material including the magnetic field. The tracking of particles accounts for the specific energy loss, multiple scattering, and the following secondary processes: photoelectric effect, emission of δ rays, bremsstrahlung, positron annihilation, pair production, Compton scattering, weak decays and strong interactions.

Detector response

For every particle crossing the sensitive volume of a sub-detector a response in the form of electronic signals is computed. This part is specific to every sub-detector and incorporates efficiencies, possible background, resolution, and other parameters needed to simulate a reliable response.

Agreement between the simulated data and real data for well known processes is satisfactory. However, some discrepancies may still exist. They are mostly due to occasional changes in the detector performance, alignment problems, and other unexpected effects. Usually, it is difficult to correct for these scenarios by changing DELANA and DELSIM procedures, in particular, if the reason for discrepancies is not well understood. Instead, an additional fine tuning and calibration of data is often performed on the DST level. It corrects for remaining discrepancies on a more empirical level.

4.2 Luminosity measurement

The luminosity is determined by the number of tagged Bhabha events in the STIC calorimeter. Bhabha events are well known and, in addition, have a large cross-section (Section 2.4). They are selected by requiring a coincidence of two coplanar electromagnetic showers, each with the reconstructed energy larger than 65% of the beam energy. The total systematic error of the luminosity measurement is about 0.5% with the main contribution arising from the uncertainty of the acceptance of the STIC sub-detector. The theoretical uncertainty of the Bhabha production amounts to about 0.25%.

4.3 Reconstruction of tracks

The reconstruction of tracks is implemented within the DELPHI off-line analysis program DELANA ([50]).

The first stage of the reconstruction procedure is performed independently for each sub-detector. Recorded space points (hits) are analysed, calibrated, and a local pattern recognition is performed for some of sub-detecors. The output of this stage is a set of track elements (TE) that can be single points, energy clusters from calorimeters, or fully reconstructed track segments as in the case of the TPC.

The main track search procedure used in the barrel region starts with the track elements seen in the TPC. These track segments are extrapolated to other sub-detectors (ID, OD, FCA, FCB) and associated with compatible track elements. There are also other methods for tracks not reaching the TPC, passing by trough the dead zones of the TPC, or escaping in the very forward region. The obtained track strings are then passed through the full fitting process and any remaining ambiguities are resolved. The fitting procedure accounts for multiple scattering and ionisation [51].

The fitted tracks are then extrapolated through the whole detector. At this stage VD hits are also associated to the tracks. The tracks are then refitted and the search is made over remaining track elements not associated to any track.

At the last stage energy clusters seen in the calorimeters are associated to the reconstructed charged tracks. The remaining energy clusters create neutral tracks. Hits in the Muon Chambers are also associated to charged tracks at this stage.

The efficiency and the resolution of reconstructed track parameters depend on track momentum, its direction, sub-detectors used in the reconstruction, and isolation from other tracks. For muons from $Z^0 \to \mu^+\mu^-$ the resolution of track momentum of

$$\sigma(1/p) = 0.57 \times 10^{-3} \text{ c/GeV}$$

is obtained, if the tracks contain an information from VD, ID, TPC and OD ([56]).

4.4 Alignment of the detector

The global alignment of the DELPHI detector mainly uses $Z^0 \to \mu^+\mu^-$ events collected at 91 GeV as well as hadronic decays of Z^0 bosons to assure enough tracks for a more refined alignment. The alignment is an iterative procedure with a step by step alignment of each sub-detector starting with the OD as a reference. The wire positions of OD are known to about 30 μm from optical and mechanical surveys. In the first step the VD position is determined by assuming colinearity of two muons. Subsequently other sub-detectors are aligned on the reference tracks formed by OD and VD. The forward part is aligned with tracks that pass the TPC and the forward chambers.

4.5 Jet reconstruction

Jet is a cluster of particles that are assumed to arise from the same primary particle. The primary particle is then characterised by the jet four momentum which is the sum of four momenta of all tracks belonging to this jet. In the case the primary particle is a quark, the corresponding jet should contain all detected particles produced in the fragmentation process and decays of secondary particles. The number of reconstructed particles in quark jets is on average about 12 at the LEP2 CMS energies.

There are several algorithms and criteria to cluster particles in jets. We have chosen the LUCLUS [32] algorithm which is designed for e^+e^- interactions. Among others that have been tested, LUCLUS enables the best separation between the W^+W^- events and the background events [74]. LUCLUS defines the distance d_{ij} between two particles or clusters as:

$$d_{ij} = \frac{4|\mathbf{p_i}|^2 \cdot |\mathbf{p_j}|^2 \cdot sin^2(\theta_{ij}/2)}{(|\mathbf{p_i}| + |\mathbf{p_j}|)^2},$$

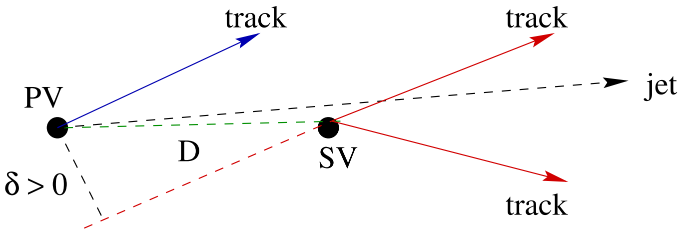

Figure 4.1: An illustration of a D meson decay. Decay products of the D meson (red tracks) have positive impact parameters δ with respect to the primary vertex (PV) and the jet direction. The track in blue arises from the primary vertex (PV).

where $\mathbf{p_i}$ and $\mathbf{p_j}$ are momenta of clusters and θ_{ij} the angle between them. Initially, each particle is assumed to be a cluster by itself. Then, two clusters with the smallest distance are found and joined to one cluster if the distance is smaller than a certain value assigned as d_{join}. This is repeated until the distance between any two clusters is smaller than d_{join}. The remaining clusters represent jets.

4.6 Impact parameters and fine tuning of Vertex Detector

At the LEP CMS energies hadrons composed of b and c quarks travel on average about 2.5 mm and 2 mm, respectively, before they decay. The estimate is very rough because the decay length depends on the actual type of the hadron and its momentum. The displaced decay point (secondary vertex) of a heavy flavour hadron can be assessed by using impact parameters of its decay products [61]. The impact parameter is defined as the distance of the closest approach of a particle to the primary interaction point (primary vertex) (Figure 4.1). A sign is also attributed to the impact parameter. It is defined with respect to the jet direction to which the given track belongs. The sign is positive if the angle between the vector joining the primary vertex to the point of the closest approach and the jet direction is less than 90^0. Particles arising from heavy flavour hadrons produce an excess of positive impact parameters. On the other hand, particles from the primary vertex contribute both positive and negative impact parameters due to measurement errors. Since heavy quarks are practically not produced in the fragmentation process, the impact parameters can be used to identify primary heavy quarks such as b or c.

In order to calculate the impact parameters from the measured tracks parameters the position of the primary vertex has to be known. The primary vertex is reconstructed for every event using the measured tracks and the beamspot position as a constraint. The beamspot is determined as an average primary vertex of about 200 successive hadronic events. In practice, the importance of the beamspot position is limited by the beam size which is about 100 μm in the horizontal direction and 25 μm in the vertical direction.

The primary vertex is fitted by using charged tracks with at least 2 hits in the VD. In addition, the tracks should be close to the beamspot in terms of d/σ_d, where d is the distance from the track to the beamspot and σ_d is the corresponding error that includes the tracking error and the beamspot size. Determination of the primary vertex is an iterative procedure in which at each step the track with the worst χ^2 contribution to the fit is removed until all tracks have a reasonable small χ^2. Typically, about 6 charged tracks per jet contribute to the fit leading to the uncertainty of the fitted primary vertex of about 30 μm in the hadronic Z^0 events.

A reliable simulation should well describe distribution of impact parameters, their resolution, the efficiency of VD, and the global tracking performance. Any disagreement in these quantities can result in a large discrepancy between data and simulation in a separation of heavy flavour jets. The standard DELPHI simulation procedure is usually not reliable for precise measurements, hence an additional fine tuning is used on the level of the DST. At LEP2 the tuning is based on hadronic Z^0 decays collected at 91 GeV [62]. Comparison between real data and simulation for the number of tracks having at least one VD hit associated and the number of associated hits in the VD is shown in Figure 4.2. The agreement of the latter is particularly good implying that the efficiencies of VD modules are well determined. The number of tracks having VD hits is essentially a result of general tracking performance and there some difference between real data and the simulation may be observed.

Resolution of the measured impact parameters mainly depends on the VD as the closest and the most accurate tracking sub-detector. It is convenient to project impact parameters onto the transverse plane and the z direction because of different resolutions. The uncertainty of the impact parameter σ_δ as a function of the polar angle θ and momentum p can be parametrised as follows [60]:

$$\begin{aligned} {\sigma_\delta^{R\Phi}}^2 &= {\sigma_{pv}^{R\Phi}}^2 + {a^{R\Phi}}^2 + {b^{R\Phi}}^2 \frac{1}{p^2 \cdot \sin^3\theta}, \\ {\sigma_\delta^{z}}^2 &= {\sigma_{pv}^{z}}^2 + {a^{z}}^2 + {b^{z}}^2 \frac{1}{p^2 \cdot \sin^5\theta}, \end{aligned} \tag{4.1}$$

where $\sigma_{pv}^{R\Phi}$ and σ_{pv}^{z} are uncertainties of the primary vertex position, $a^{R\Phi} \sim 22$ μm and $a_z \sim 39-100$ μm represent the intrinsic resolution of the tracking system, while the terms with $b^{R\Phi} \sim 65$ GeVμm and $b^z \sim 71$ GeVμm reflect the influence of multiple scattering. To estimate the parameters in Eq. 4.1 tracks with negative impact parameters are used. In this way, the probability of choosing a track from a long lived meson is highly suppressed. The coefficients a and b in Eq. 4.1 are determined by the likelihood fit. Since the resolution of impact parameters depends on the number of associated hits in the VD, the fit is performed for any possible hit pattern, separately. Tracks having no VD hits are not

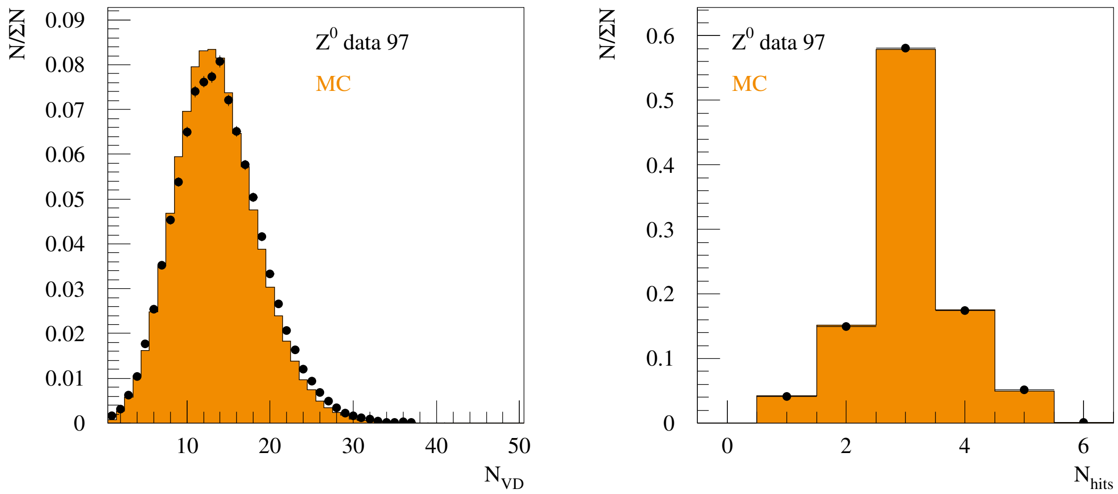

a) b)

Figure 4.2: Comparison between real data and simulation (MC) for the number of tracks with associated VD hits **a)** and the number of VD hits per track **b)**.

considered here. Usually, the untuned simulation overestimates the resolution of impact parameters. To achieve an agreement with the real data, the simulated impact parameters are increased proportional to the observed difference between resolutions. Comparison of impact parameters projected onto the $R\Phi$ plane, before and after this correction, is shown in Figure 4.3 a). There is a large tail in the distribution of negative impact parameters. It is mainly due to badly reconstructed tracks or tracks arising from the secondary interactions in the detector material. The tail in the simulation is corrected by a random smearing of a fraction of tracks by an exponential function. After this correction the difference between the simulation and real data does not exceeds 10% as shown in Figure 4.3 b).

In the next step the expected uncertainties of impact parameters are corrected according to the observed resolution. This correction is performed for both real data and simulation. In this way, the significance of impact parameters ($S = \delta/\sigma_\delta$) is automatically tuned (Figure 4.4 and 4.5 a)). The significance of impact parameters is the basis in construction of a separating variable used to distinguish the light from the heavy flavour jets. Difference between the significance distributions for tracks arising from light, c, and b quarks is shown in Figure 4.5 b). A detailed description of how this information is used to separate flavours of jets is discussed in Section 7.2.3.

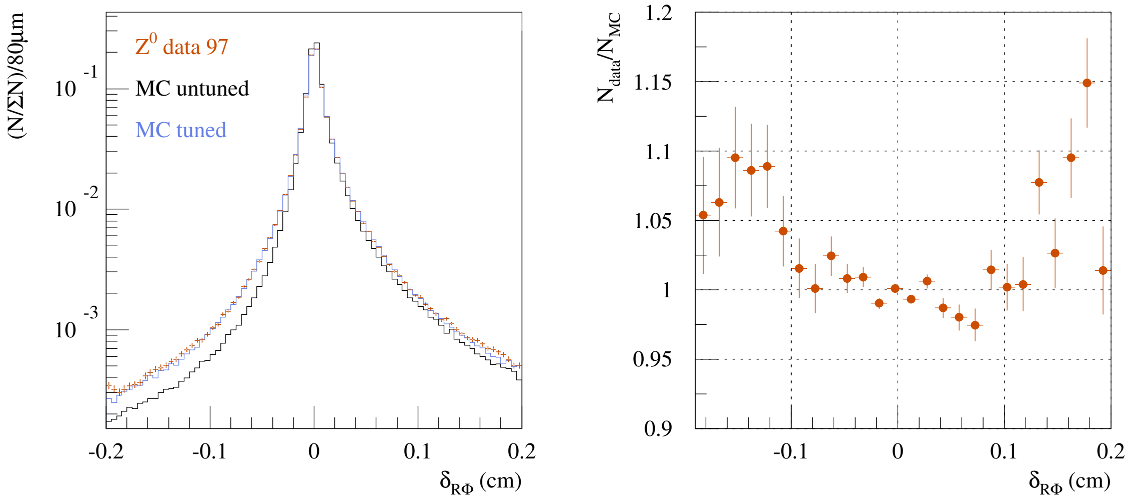

a) b)

Figure 4.3: **a)** Distribution of impact parameters in the $R\Phi$ plane for real data and simulation before and after the tuning. **b)** The ratio between the two distributions from a) after the tuning.

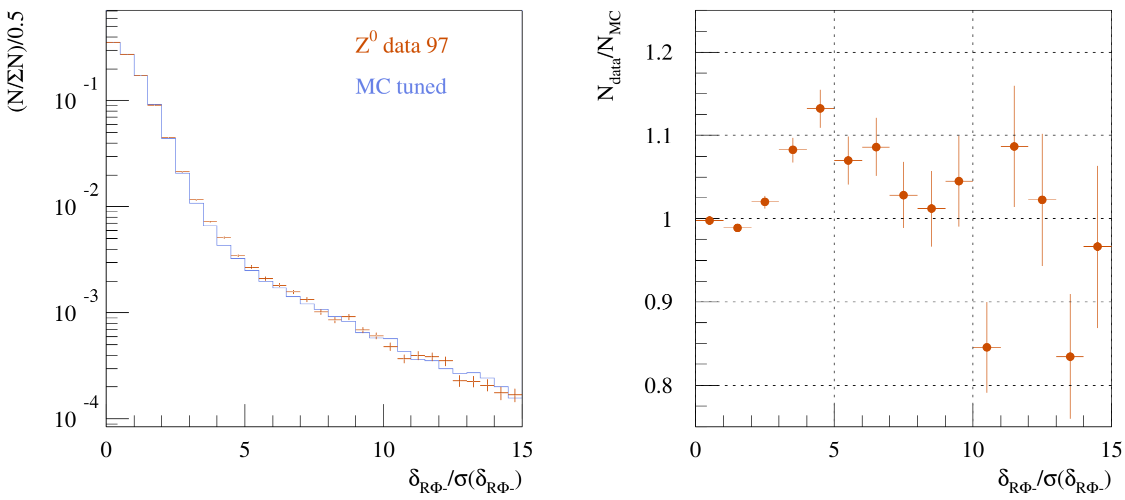

a) b)

Figure 4.4: **a)** Distribution of significance of negative impact parameters in the $R\Phi$ plane for real data and simulation after the tuning. **b)** The ratio between real data and simulation in a).

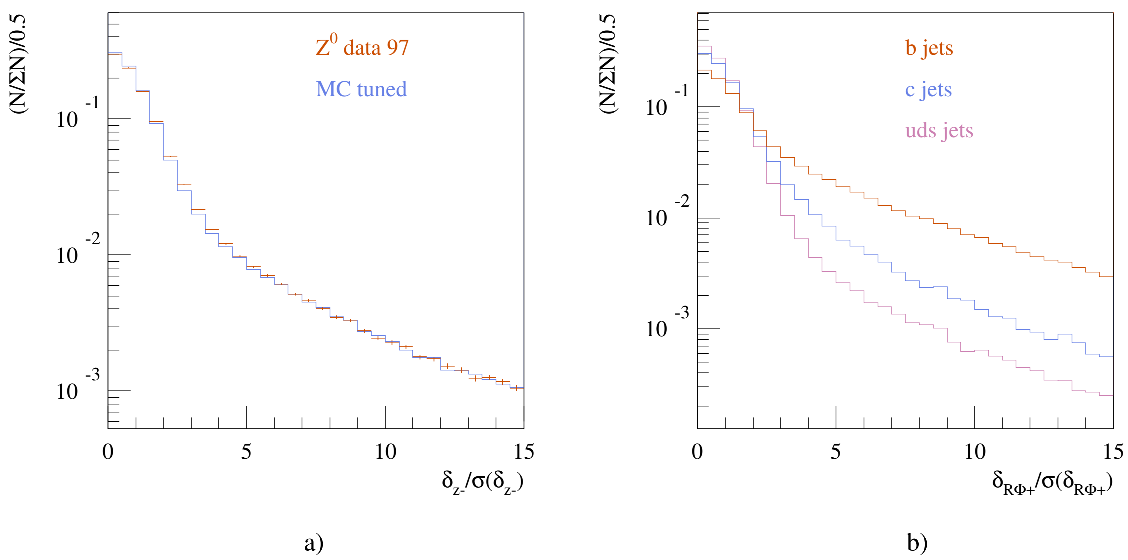

Figure 4.5: a) Significance distribution of negative impact parameters in the z direction after the correction. **b)** The expected distribution of significance for positive impact parameters and different flavour types.

4.7 Particle identification

The identity of particles is another important information that was used at many stages of the presented analysis. In the following, we will briefly describe some algorithms and performances of muon, electron and photon identification. The emphasis is given to the identification of $K^{\pm}, \pi^{\pm}$ and p with the RICH counters.

4.7.1 Muon identification

The iron of the hadron calorimeter provides a filter which enables a separation between muons and hadrons. The bulk of hadronic showers is stopped in the hadron calorimeter, whereas muons of momenta above 2 GeV/c are expected to penetrate to the Muon Chambers. Despite this filtering there is still a residual activity from hadronic tracks; punch-through from hadronic showers, decays in flight, and particles traversing along the HCAL boundaries all contribute to this background. Criterion used to identify muons is placed on the goodness of association between the extrapolated charged tracks and signals in the Muon Chambers. For this purpose a χ^2 fit is performed that accounts for tracking errors and multiple scattering. Based on χ^2 of the fit and the number of associated points in the Muon Chambers four types of muon identification are defined. They are entitled as: very loose, loose, standard, and tight. The identification efficiency has been studied

Tag	Efficiency (%)	Misid. Probability (%)
Very Loose	95.8 ± 0.1	5.9 ± 0.3
Loose	92.2 ± 0.2	1.5 ± 0.1
Standard	84.0 ± 0.2	0.7 ± 0.1
Tight	70.3 ± 0.3	0.5 ± 0.1

Table 4.1: Efficiencies and misidentification probabilities for different types of the muon identification [56]. The values are averaged over momenta and directions of tracks.

Tag	Efficiency (%)	Misid. probability (%)
Loose	85	~ 1.6
Standard	65	~ 0.4
Tight	60	~ 0.1

Table 4.2: Efficiencies and misidentification probabilities for different types of electron and positron identification in multi-hadronic events [56]. The values are averaged over momenta and directions of tracks with $p \geq 3$ GeV/c. The misidentification probabilities are measured with $K_S \to \pi^+\pi^-$ decays.

in real data and simulation mainly using $Z^0 \to \mu^+\mu^-$ and $\tau^+\tau^-$ as well as $\gamma\gamma \to \mu^+\mu^-$ events. The three prong τ decays also help in determination of the muon misidentification probability caused by pions. The latter is obtained by using $K_S^0 \to \pi^+\pi^-$ decays, as well. The average efficiencies of the muon identification are provided in Table 4.1, together with the probability for pions to be identified as muons.

4.7.2 Electron identification

Identification of electrons and positrons relies on a comparison between a reconstructed track and the energy deposition in the electromagnetic calorimeters. A match between the deposited energy and the track momentum is required together with a match of the extrapolated track with the shower position and its direction. The shower shape is required to be compatible with the one expected from electrons. An independent piece of information provides the measurement of the specific ionisation (dE/dx) in the TPC. By combining above criteria three different kinds of electron identification are provided: loose, standard and tight. The average efficiencies and misidentification probabilities for particles with momenta above 3 GeV/c in the hadronic Z^0 decays are presented in Table 4.2. The efficiency as a function of momentum varies within 20%. It is lower for electrons of lower momenta.

4.7.3 Photon identification

Approximately 40% of photons in the barrel region convert into an electron-positron pair before they enter the HPC. The number is even higher in the forward region. These photons can be identified by tracking e^+ and e^- to the associated showers in the electromagnetic calorimeters. If a shower in the HPC cannot be associated to a charged track it is also considered to be a photon. In addition, the shape of the shower should be compatible with an electromagnetic shower in order to reject hadrons producing showers already in the electromagnetic calorimeter. The efficiency of the photon identification for photons with momenta above 20 GeV/c is close to 75 % [56].

4.7.4 Identification of $K^\pm$, $\pi^\pm$, p and fine tuning of RICH counters

Identification of charged hadrons like $K^\pm, \pi^\pm$ and p in an almost full momentum range is achieved by combining the specific ionisation dE/dx measured in the TPC and the Čerenkov photons detected with the RICH counters. The TPC enables an efficient separation of particles with momenta below approximately 1 GeV/c. For particles with higher momenta the RICH counters are more efficient. Since we are interested in an identification of fast particles, we will discuss only the identification based on the RICH counters.

Background reduction

In the first step of RICH data treatment a cleaning algorithm removes detector and track related noise. The most severe sources of noise are: electronic noise, after-pulses, cross-talk, δ electrons, photon-feedback, and electrons produced by ionisation of tracks passing trough the drift tubes. The electronic noise is most efficiently reduced by requiring a time coincidence between the cathode and anode readout. After-pulses appear as an oscillating electronic-signal, usually on the same channel. They are suppressed by requiring a certain time delay between two successive pulses on the same channel. The cross-talk is the electronic signal induced during creation of an avalanche on a neighbouring wire and pad of MWPC's. It is reduced by ignoring pulses that are close in space and time. The photon-feedback is caused by photons emitted during the acceleration of electrons close to anode wires. The emitted photons will be absorbed after about 18 mm and converted into electrons leading to a electronic signal that is delayed in time and usually appears on the same or the neighbouring wires. The bulk of the photon-feedback is removed by the same criteria as used for the after-pulses. A charged track traversing the drift tube produces around 600 ion pairs. Cross-talk, photon-feedback, after-pulses, and other noise induced by electrons from the ion pairs can extend to about 15 cm behind the point of particle passage if investigated in the tube coordinates. Therefore, these region is cut out.

After the cleaning procedure we are left with the ratio between the signal-peak and the noise-level of about 10, whereby the signal loss is about 10%.

The remaining photoelectrons are associated to the extrapolated charged tracks and the Čerenkov angles are calculated. Each photon is associated to every track if the corresponding Čerenkov angle falls within three standard deviations around the expected angle for at least one of five hypothesis: e, μ, K, π or p. A photon can be radiated either in the liquid or in the gas radiator. An average free path of a photon in the 5 cm thick drift tube is 18 mm. Based on the measured radial position of the photo-electron the probability is calculated that the photon arises from a given radiator (liquid or gas).

Alignment and fine tuning

Once photons are associated to tracks and the Čerenkov angles are calculated an alignment procedure is performed. Alignment of the RICH counters at LEP2 uses tracks from the hadronic decays of Z^0 bosons. In the alignment procedure individual parts of the RICH counters are allowed to translate and rotate in all directions to minimise the resolution of the measured Čerenkov angles. This is performed separately for every liquid radiator, photon detector, and mirror. To calculate the expected Čerenkov angles we have to know particle identities. In the gas radiator this is achieved by selecting tracks with momenta between 3 GeV/c and 8 GeV/c (Figure 4.11). Neglecting small fractions of electrons and muons, pions are the only particles that will emit photons in this momentum region. In the liquid radiator particles with momenta above 6 GeV/c are selected. The selected particles are expected to emit photons at the maximal Čerenkov angles, apart from a small fraction of protons that emit photons at somewhat smaller angles. The alignment procedure improves the resolution of Čerenkov angles by about 10%. The final resolution and the number of associated photons for muons from $Z^0 \to \mu^+\mu^-$ decays is presented in Table 3.1.

As in the case of VD and impact parameters a fine tuning of the simulation and real data is necessary in order to obtain accurate predictions. In the following we will consider only the barrel part of the RICH counters because the forward part is not used in our analysis. The fine tuning of the RICH counters is applied to both real data and simulation, whereby each chamber and mirror are in general treated separately. Samples used are the same as those in the alignment procedure. Thus, the expected Čerenkov angles are known.

Real data are tuned to be self-consistent. This essentially means that the expected Čerenkov angles, their resolution, and the expected number of photons agree with the measured values. The expected values are calculated from the permanently monitored drift velocities, conversion depth, absorption length in the drift gases, transparencies of radiators, and refractive indices. An offset between the expected and the measured Čerenkov angles is corrected by changing the initial value of the refractive index measured by the sound velocity in radiators. A match of the resolution and the number of photons is obtained by scaling the expected errors and the number of expected photons. The expected errors $\sigma(\theta_C^{expected})$ are multiplied by such a factor that the standard deviation of the Gaussian part of the *pull* distribution equals 1, where:

$$pull = \frac{\theta_C^{expected} - \theta_C^{measured}}{\sigma(\theta_C^{expected})}.$$

On average, the expected errors are found to be underestimated by about 20%. The rescaling of the expected errors is applied to overall samples without examining any detailed topological dependencies. Subsamples were also checked and some quite large discrepancies were observed for certain topologies. In Figure 4.8 a) $\sigma(pull)$ as a function of direction (Φ) of the emitted photon in the liquid radiator is shown. Definition of the direction of the emitted photon is illustrated in Figure 4.6. $\sigma(pull)$ increases as the path of photons to the photo-detector increases. (i.e. increasing Φ). The effect is likely to be due to an underestimated chromatic dispersion. Namely, the relative contribution of the chromatic dispersion to an overall resolution of Čerenkov angles increases by increasing the photon path. The reason is geometrical. There is also a possibility that short time variations of refractive index would lead to such behaviour. In this case, correlation between photons coming from the same liquid radiator and event is expected. The correlation is not observed, therefore, this scenario is not very likely. To correct for this effect, the initially expected uncertainty due to the chromatic dispersion was multiplied by the factor 2.2 and the problem disappeared (Figure 4.8 a)). The increased chromatic dispersion was reproduced in the simulation by a random smearing of Čerenkov angles proportional to the increase of the overall expected error. In the gas radiator the contribution from the chromatic dispersion cannot be experimentally distinguished from other sources of uncertainty as all photons have approximately the same path and fall almost perpendicular onto the photo-detection plane.

Another interesting observation is shown in Figure 4.8 b) where we see comparison between the distribution of Čerenkov angles for photons that arrive first to the MWPC's to those that arrive later (see Figure 4.7). For the early photons background is larger for larger Čerenkov angles while background for the late photons is larger for small Čerenkov angles. The observed asymmetry is most likely due to the feed-back photons. They are delayed in time with respect to signal electrons. The effect is not predicted by the simulation. A removal of the residual feed-back photons is not efficient without a significant loss of true photons. Instead, we simulated the feed-back photons according to the observed distribution in real data. The probability that a signal photo-electron produces a

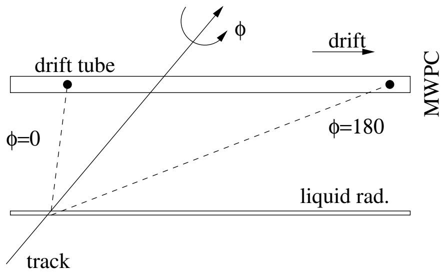

Figure 4.6: Definition of angle Φ in the liquid radiator.

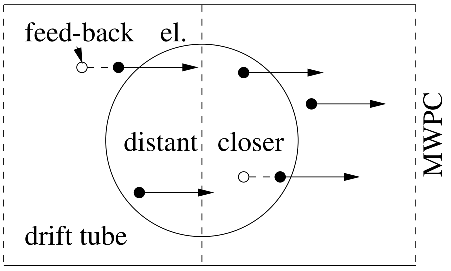

Figure 4.7: Definition of the closer and the distant half of a ring. Open rings represent feedback photons as seen when the pulse is transformed into the space coordinates.

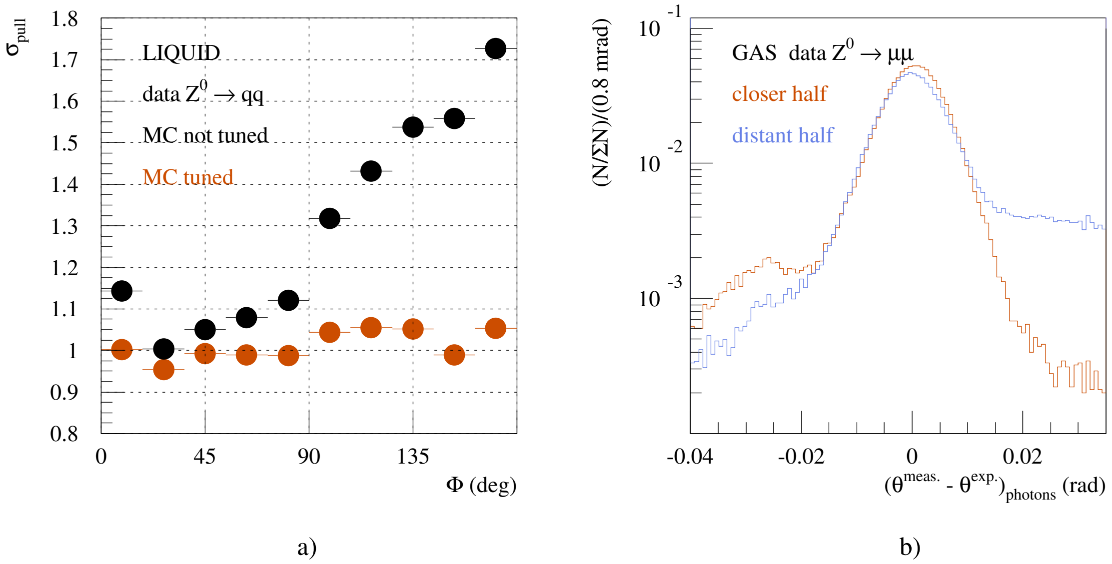

Figure 4.8: a) The standard deviation of the pull of Čerenkov angles in the liquid radiator as a function of the direction of emitted photons (Φ). Larger Φ means larger path to the photon detector. The first interval corresponds to the average over all angles. **b)** The distribution of Čerenkov angles in the gas radiator for photons belonging to the closer and distant halves of rings.

feed-back photo-electron not rejected in the cleaning procedure is found to be about 11%.

Apart from these, many other parameters are tuned in the simulation to agree with the real data. For a reliable simulation the most important quantities are: efficiencies of individual modules, resolution of the Čerenkov angles, resolution of the mean Čerenkov angles belonging to a track, and the number of reconstructed photons. Occasional short malfunctions of chambers were simulated by a random deleting of rich information from these chambers. The number of photons associated to tracks is tuned by a random removal of photons in the simulation which initially provides more photons as observed. Comparison between real data and simulation after the tuning for the number of photons is shown in Figure 4.9. Clusters of Čerenkov photons belonging to the same track and the corresponding mean Čerenkov angle are provided by the RIBMEAN algorithm described later on. Tuning of the Čerenkov angle resolution is performed in two ways. The simulated Čerenkov angles are randomly smeared proportional to their expected errors in order to match the measured resolution. This accounts for an overestimated intrinsic resolution of Čerenkov angles in the simulation. In addition, the Čerenkov angles of photons belonging to the same track are coherently smeared proportional to the expected error of the mean angle (i.e. rings are blowed up or shrunk). The latter reproduces correlated effects, in particular short time variations of the refractive index. Proportion of each of two random smearings is chosen such that distributions of the Čerenkov angles and the mean Čerenkov angles simultaneously match. A comparison between real data and simulation after and before the tuning of resolution is shown in Figures 4.9 and 4.10.

The described tuning is performed on the hadronic Z^0 decays collected at the beginning of each year. The stability of the RICH counters during the year was also checked to assure reliability for the high energy runs. We found no deviations, apart from a systematic drift of the drift velocity that was corrected for. A systematic changing of drift velocity with the time has been explained as a systematic changing of performance of flow meters used to control the mixing of the drift gases (ethane and methane).

Particle identification

Several algorithms for particle identification based on information from the RICH counters have been developed so far. The main difficulty is to deal with ambiguities whose shape and level are not known a priori on the single track basis. For the presented work we combined information from two algorithms: RIBMEAN+NEWTAG [67, 68, 72] and HADSIGN [71, 69].

HADSIGN is based on a probabilistic approach. For each mass hypothesis distribution of signal photons is assumed to be normal around the expected Čerenkov angle. The standard deviation is equal to the expected error of each individual photon. For

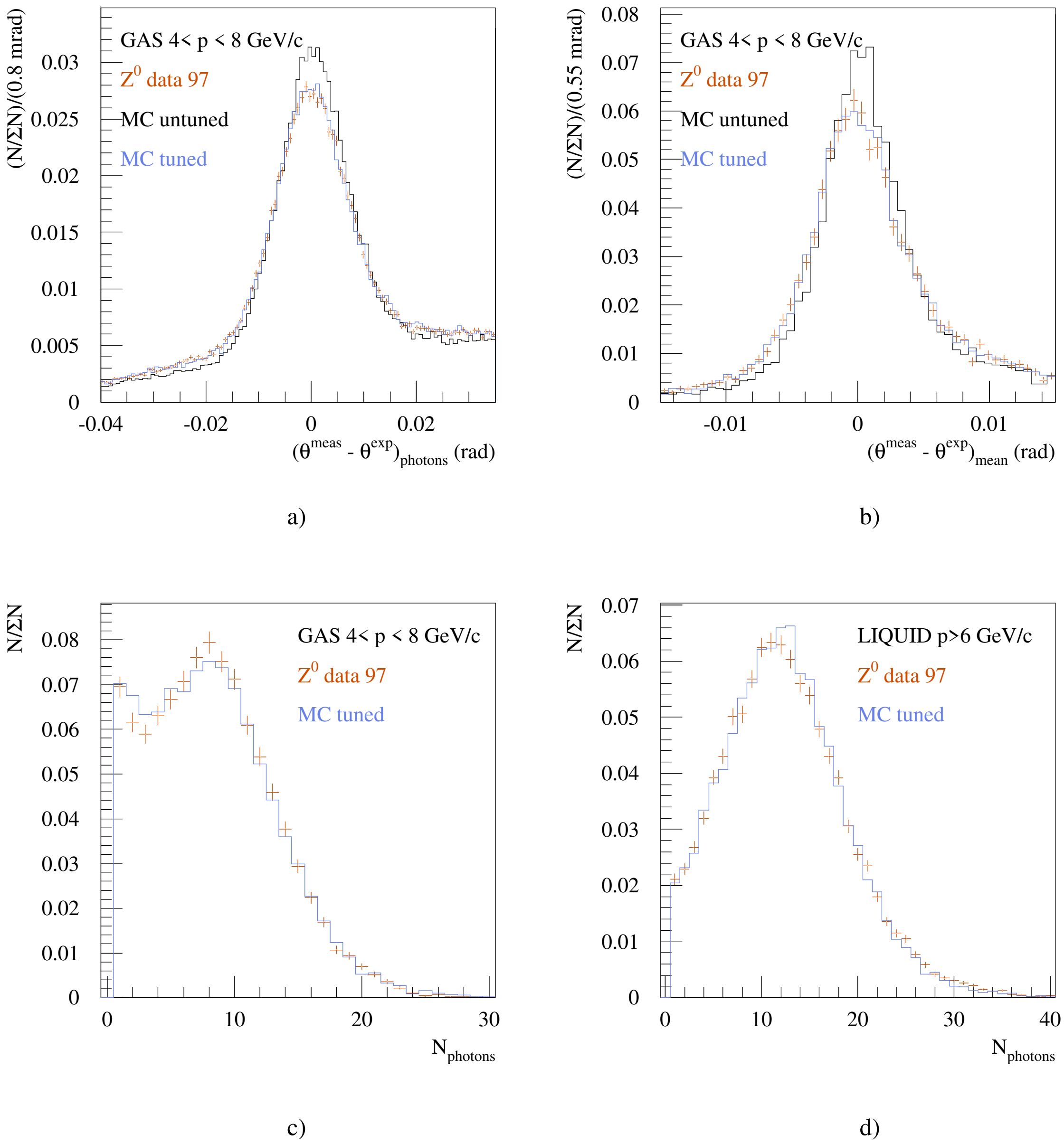

Figure 4.9: a) Distribution of Čerenkov angles in the barrel gas radiator. **b)** Distribution of mean Čerenkov angles reconstructed by RIBMEAN. **c)** The number of photons attributed to tracks in the gas radiator after ambiguities have been resolved.**d)** The same for the liquid radiator.

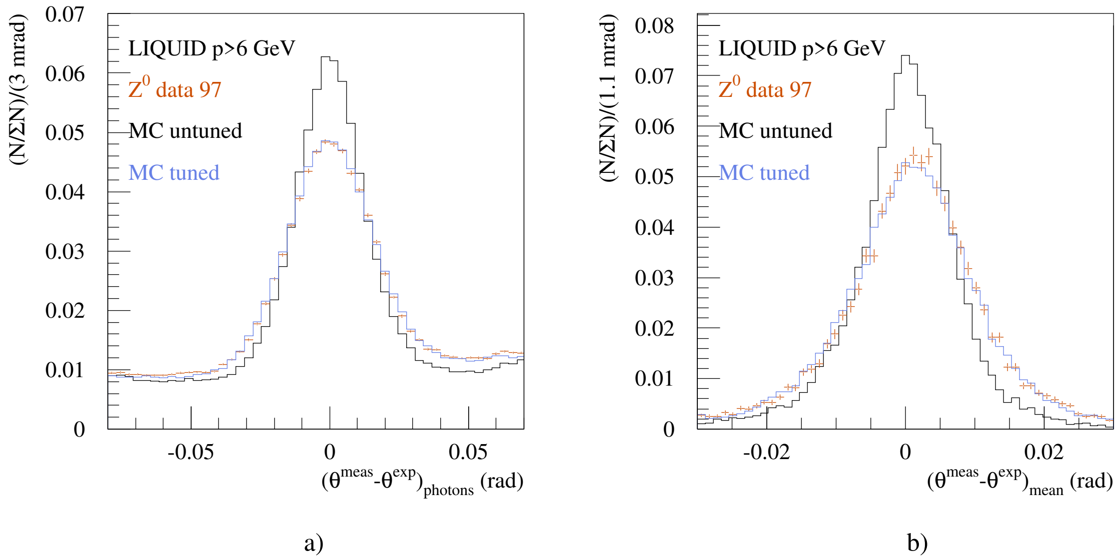

Figure 4.10: a) Distribution of Čerenkov angles in the liquid radiator. **b)** Distribution of mean Čerenkov angles reconstructed by RIBMEAN.

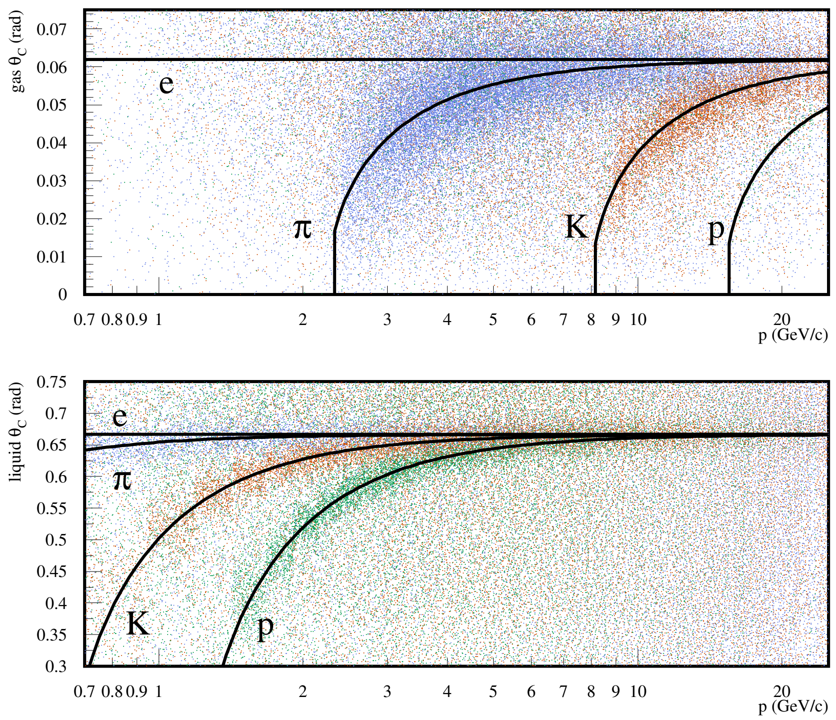

Figure 4.11: The simulated distribution of Čerenkov angles as a function of momenta and different mass hypothesis. The upper plot is for the gas radiator and the bottom plot for the liquid radiator in the barrel. The distributions include all ambiguities.

background an uniform distribution is assumed without an absolute normalisation. Normalisation of background is a free parameter obtained by maximisation of the probability for each mass hypothesis. The probability is parameterised also as a function of the number of associated photons. The number of signal photons is assumed to obey the Poisson distribution with the mean equal to the expected number of photons for a given hypothesis. After the maximisation of the probability the hypothesis with the highest probability is retained as the preferred one. Criterion for goodness of the identification is the relative difference in probabilities between the most likely and the second most likely hypothesis. It is expressed as a flag: loose, standard, or tight

RIBMEAN searches for clusters of photons in the space of Čerenkov angles. Search for the clusters starts around the expected angles for each mass hypothesis and looks for photons about 3 standard deviations away. To every photon a weight is attributed depending on its expected error, quality of the track fit, position, probability to be a background photon, conversion depth, and possible ambiguities with other tracks. Of all clusters found, the one with the highest number of the weighted photons is retained and the mean Čerenkov angle is calculated. To the favoured hypothesis a flag is attributed. It essentially measures how many standard deviations away of the mean angle is the closest neighbouring hypothesis [68].

RIBMEAN and HADSIGN simultaneously combine information from the liquid and gas radiators. Though, almost whole momentum region is covered by the liquid and the gas radiator, the separating power can vary significantly depending on momenta and identities of particles. The simulated distribution of Čerenkov angles in the liquid and gas radiator as a function of particle momenta in the hadronic events is shown in Figure 4.11. Below 1.5 GeV/c protons do not emit photons in the liquid radiator. This is called the liquid veto. If a particle in this momentum region has no photons associated in the liquid radiator, it is a proton candidate. A separation between pions and kaons in the liquid radiator is possible up to about 3 GeV/c. In momentum region between about 3 GeV/c and 8 GeV/c pions are the only particles that emit photons in the gas (gas veto). If there are enough photons attributed to a track in the gas veto region, the particle is identified as a pion, otherwise it is identified as a kaon and a proton with equal probabilities. Above the gas veto region RICH enables a separation between pions and kaons up to about 20 GeV/c, while protons can be separated from the other two up to about 40 GeV/c. A further complication is a momentum dependent particle content in the hadronic jets. On average, there are about 80% $\pi^{\pm}$, 15% $K^{\pm}$ and the rest are mostly protons. However, at momenta above 10 GeV/c there are only about 50% of pions. Due to these inhomogeneities, the obtained efficiencies and purities heavily depend on particle momenta (Figure 4.12). We used the identification that combines the information from HADSIGN and RIBMEAN. HADSIGN has been found to perform

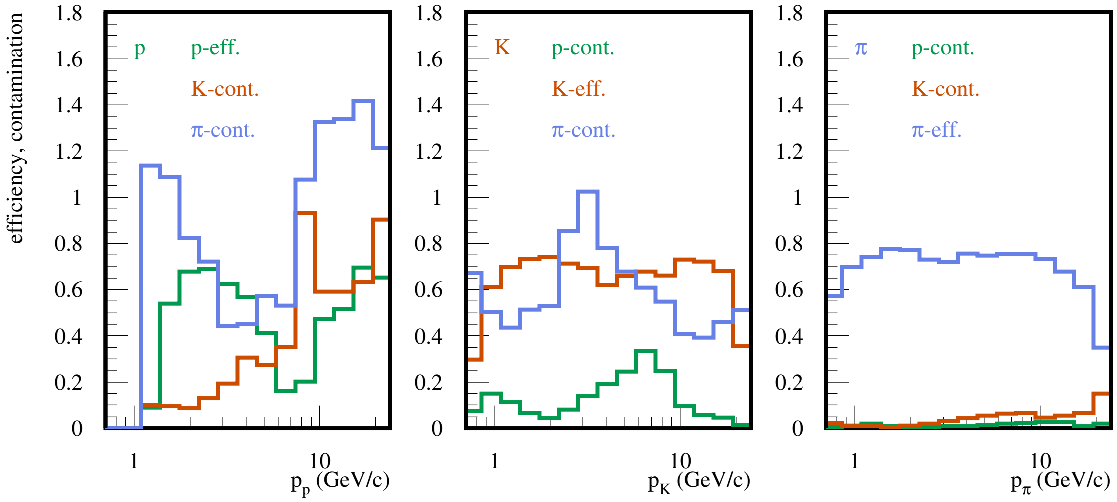

Figure 4.12: Momentum dependent efficiency and contamination of identified $\pi^{\pm}$, $K^{\pm}$ and p in the hadronic Z^0 decays. The efficiency is defined as the fraction of 'true' identifications. The contamination represents the number of identified particles of a given type that are generated as another type divided by the number of 'true' identifications of the considered type.

better in the identification of kaons and protons while RIBMEAN provides a better pion identification, in particular, in the veto region. To combine two algorithms an 'OR' was placed between the flags of the two.

4.8 Kinematicaly constrained fit

The kinematicaly constrained fit is intended to improve the momentum resolution of jets and the association of tracks to jets under an assumed event topology. In a different role it provides a test of an assumed topology by looking at χ^2 of the constrained fit. At LEP the CMS energy equals twice the beam energy while the total momentum is zero. These leads to four kinematic constraints (4C fit). In the case of the W^+W^- production we can further require equal invariant masses of decay products from each of two $W^{\pm}$ bosons (5C fit). Since the mass of the $W^{\pm}$ boson is relatively well measured, we could also fix it to the measured value and by that imposing another constraint (6C fit). The 6C fit imposes 6C very tight constraint and requires a precise parameterisation of measurement errors to perform well. In the analysis we relied on the 5C fit. The fit was performed by the program PUFITC [75] specially designed and tuned for the DELPHI data. Some basic ideas are presented below.

The main input to the program are momenta of reconstructed hadronic jets and leptons. In the case of the 5C or the 6C fit we have to provide also the assumed pairing of jets. The most important is the parameterisation of momentum errors. In the case of muons the errors are obtained directly from the track fit. Usually, they are small compared to errors of other objects. The energy error of electrons depends on the response of the electromagnetic calorimeter while the angular errors are determined from the track fit. Decays of τ leptons result in at least one neutrino which is not detected. For this reason we treat the detected particles arising from τ decays in the same way as hadronic jets. The reconstructed energy of hadronic jets is on average smaller than the true energy. Therefore, the reconstructed energy is first multiplied by a factor depending on the polar angle. The energy error is also parametrised as a function of the polar angle, while the error of the transverse momentum with respect to the reconstructed jet direction is assumed to be constant and amounts to 1.5 GeV/c. If an energetic neutrino as a separate object is expected in the event (i.e. $W^{\pm} \to l\nu_l$), it will reduce the number of degrees of freedom of the fit. The fitted momenta and energies of given objects are simultaneously obtained by the minimisation of χ^2 under the assumed topology and constraints. After the constraint fit has been performed, we re-associate tracks to the fitted jet directions using the LUCLUS distance measure (Section 4.5).

4.9 Effective center of mass energy

In many processes at LEP2, in particular QCD events (Section 2.4), an energetic photon is emitted off the initial e^+e^- system (ISR). The aim of the SPRIME package [73] is to identify the ISR photons and to estimate their energy enabling in this way a determination of the effective center of mass energy of the remaining e^+e^- system ($\sqrt{s'}$). The ISR photon is likely to be emitted at low polar angles, therefore, its identification relies on FEMC and STIC. A candidate should deposit more than 10 GeV energy and must be isolated from charged tracks with momenta above 1 GeV/c in a 0.3 rad cone around the candidate. The remaining tracks are clustered into two jets. Usually, directions of jets and photons are well measured while their energies are worse. Therefore, the angles between each of two jets and the photon are used to determine energy of the photon. Most often ISR photons escape undetected along the beam-pipe and we find a significant missing momentum pointing down the beam-pipe. In this case we assume that the photon was emitted colinear with the beam-pipe. In this approximation the two jets and the lost photon should lie in the same plane. The photon energy is then calculated by using this constraint combined with the known energy and momentum of the whole system.

4.10 Probabilistic approach

The aim of the probabilistic approach is to provide a single separating variable P^i used to separate the state i out of n_s possible states (i.e. separation of c-jets from other jet flavours). P^i is calculated from a set of n_q selected quantities with the measured values $X_1, ...X_{n_q}$ as follows:

$$P^i(X_1, ...X_{n_q}) = \frac{C^i \cdot f^i(X_1, ...X_{n_q})}{\sum_{k=1,...n_s} C^k \cdot f^k(X_1, ...X_{n_q})}, \tag{4.2}$$

where

$$f^m(X_1, ...X_{n_q}) = \prod_{j=1,...n_q} f_j^m(X_j). \tag{4.3}$$

Here, f_j^m is normalised density distribution of quantity j for objects that are in the state m. The distributions are obtained from the simulation. The coefficient C^m is the fraction of states m in the considered sample. If the values $X_1, ...X_{n_q}$ were statistically independent, P^m represents the probability that a given object is in the state m. Usually, this is not the case and P^m is only a combined separating variable without a direct interpretation of its value. The expected distribution of P^m for different states can be obtained from a simulated set that is statistically independent from the one used to extract f_j^m. We will mostly deal with only two states forming a complete system. In this case coefficients C^m are not relevant, since we are interested only in the separating power of P^i.

5

Selection of W^+W^- events

Properties of W^+W^- events depend on decay modes of either $W^\pm$ bosons. Based on this we distinguish three basic topologies:

- $\mathbf{W^+W^- \rightarrow q_1\bar{q}_2q_3\bar{q}_4}$ ($qqqq$) hadronic channel in which each $W^\pm$ boson decays into a quark pair ;
- $\mathbf{W^+W^- \rightarrow q_1\bar{q}_2l\bar{\nu}_l}$ ($qql\nu$) mixed channel in which one $W^\pm$ boson decays hadronicaly and the other one into a lepton and the corresponding neutrino;
- $\mathbf{W^+W^- \rightarrow \bar{l}\nu_l l\bar{\nu}_l}$ ($l\nu l\nu$) leptonic channel where both $W^\pm$ bosons decay leptonically.

According to the SM the corresponding branching ratios are about 46%, 44% and 10% for the hadronic, mixed, and leptonic channel, respectively [23]. For an efficient selection of events a separate method is needed for each of the considered decay channels. Moreover, each of data samples taken at different CMS energies requires its own analysis, although qualitative differences are small. We will usually refer to the 183 GeV sample as the largest one, hence, most important for the final precision of results.

5.1 Data samples, run selection and luminosity.

The analysis exploits data taken in the years 1996 and 1997. More than 95% of events collected by the DELPHI detector fulfill requirements related to statuses of sub-detectors at the time of recording. The requirements are very general and equal for all decay channels and energies; TPC, electromagnetic calorimeters, hadron calorimeters, FCA, FCB, muon chambers, and the barrel RICH were required to be operational in more than 90% while the VD in more than 70%. Furthermore, the CMS energy for a particular fill should not differ from the average energy by more than 2.5 GeV.

Year	1996	1996	1997
Energy (GeV)	161.30 ± 0.06	172.30 ± 0.06	182.7 ± 0.06
$\int \mathcal{L}$ (pb^{-1})	$9.93 \pm 0.04 \pm 0.05$	$9.98 \pm 0.04 \pm 0.05$	$51.58 \pm 0.2 \pm 0.05$

Table 5.1: The integrated luminosities and the luminosity weighted center of mass energies for accepted data. The uncertainty of the energy is mainly due to the uncertainty of the absolute energy calibration based on the resonant depolarisation. The first uncertainty of the luminosity is statistical and the second systematic.

The beam energy and the luminosity were measured as described in Sections 3.1 and 4.2, respectively. The luminosity weighted mean energies and the corresponding integrated luminosities of accepted data are presented in Table 5.1. The simulated samples were generated at CMS energies of 161, 172 and 184 GeV.

At the beginning of each of three periods at higher CMS energies, LEP ran for a short time at the CMS energy of 91 GeV to collect Z^0 decays. They were used for various calibrations and studies of systematic uncertainties, since the physical processes at 91 GeV are well known and measured with a high precision [86].

5.2 Selection of particles

The aim of particle selection is to remove those particles that are badly measured and only deteriorate performance and precision of the measurement.

Selection of charged tracks

Quality and efficiency of the track reconstruction degrade at low momenta. This is mainly due to an increased multiple scattering and a small radius of curvature which is difficult to follow. Hence, all tracks with momenta below 400 MeV/c are rejected.

A measure for the quality of a track is also the relative momentum error $\Delta p/p$ obtained from the track fit. We accepted tracks with the estimated relative momentum error below 1.

About 0.5% of tracks have unphysically high momenta. A simplified and approximate procedure is used to rescale their energies. For low multiplicity events momenta are constrained to the beam energy. If multiplicity is large, momenta of particles exceeding 75% of the beam energy are set to 15 GeV/c. If such track has associated clusters in the electromagnetic or in the hadron calorimeter, the deposited energy is used to determine the momentum.

Tracks with large impact parameters are either badly reconstructed or they arise from hard interactions in the detector material. Only few primary physical processes such as decays of K^0_S could lead to impact parameters larger than few centimeters. For this reason, tracks with impact parameters greater than 4 cm in the $R\Phi$ plane or in the z direction are rejected.

The track length is defined as the distance between the first and the last hit associated to the track. It is required to exceed 15 cm. In addition, tracks that have associated hits only in the VD and the ID are not accepted since the simulation of this tracks is not sufficiently good.

Selection of neutral particles

Neutral particles are rejected if the energy measured in the calorimeters is below 500 MeV or if the relative energy error $\Delta E/E$ exceeds 1.

The level of agreement between the recorded and the simulated tracks was checked in the hadronic Z^0 decays. Figure 5.1 shows distributions of some relevant quantities. The largest disagreement between the simulation and real data was found for the total number of reconstructed charged tracks. The efficiency of the tracking system seems to be overestimated in the simulation. A similar effect was observed also in high energy events presented later on. The disagreement in some other quantities like the track length or the relative momentum error is not as important for the presented analysis. However, it indicates some problems in the simulation.

5.3 Hadronic channel

A computerised visualisation of a hadronic W^+W^- event is shown in Figure 5.2. In the hadronic decays the produced $W^\pm$ bosons fly in the opposite directions with equal absolute momenta if no hard photon is emitted off the initial state. At the CMS energy of 183 GeV momenta of the $W^\pm$ bosons are about 44 GeV/c. Two quarks into which a $W^\pm$ decays are again oriented back-to-back in the center of mass frame of the parent $W^\pm$ boson. With respect to the $W^\pm$ direction they are almost isotropically distributed. A small anisotropy is due to some degree of polarisation of the $W^\pm$ bosons as discussed in Section 2.2.1. In the laboratory frame the colinearity and equal momenta of final fermions are slightly distorted because of the Lorentz boost. Still, one expects an approximately cross-like distribution of quarks in the laboratory frame. The typical momentum of quarks is about 50 GeV/c. A quark will fragment into a jet of about 12 reconstructed particles. If no hard gluon is emitted, we expect four jets in hadronic decays.

The most severe background is expected to arise from the QCD events (see Section

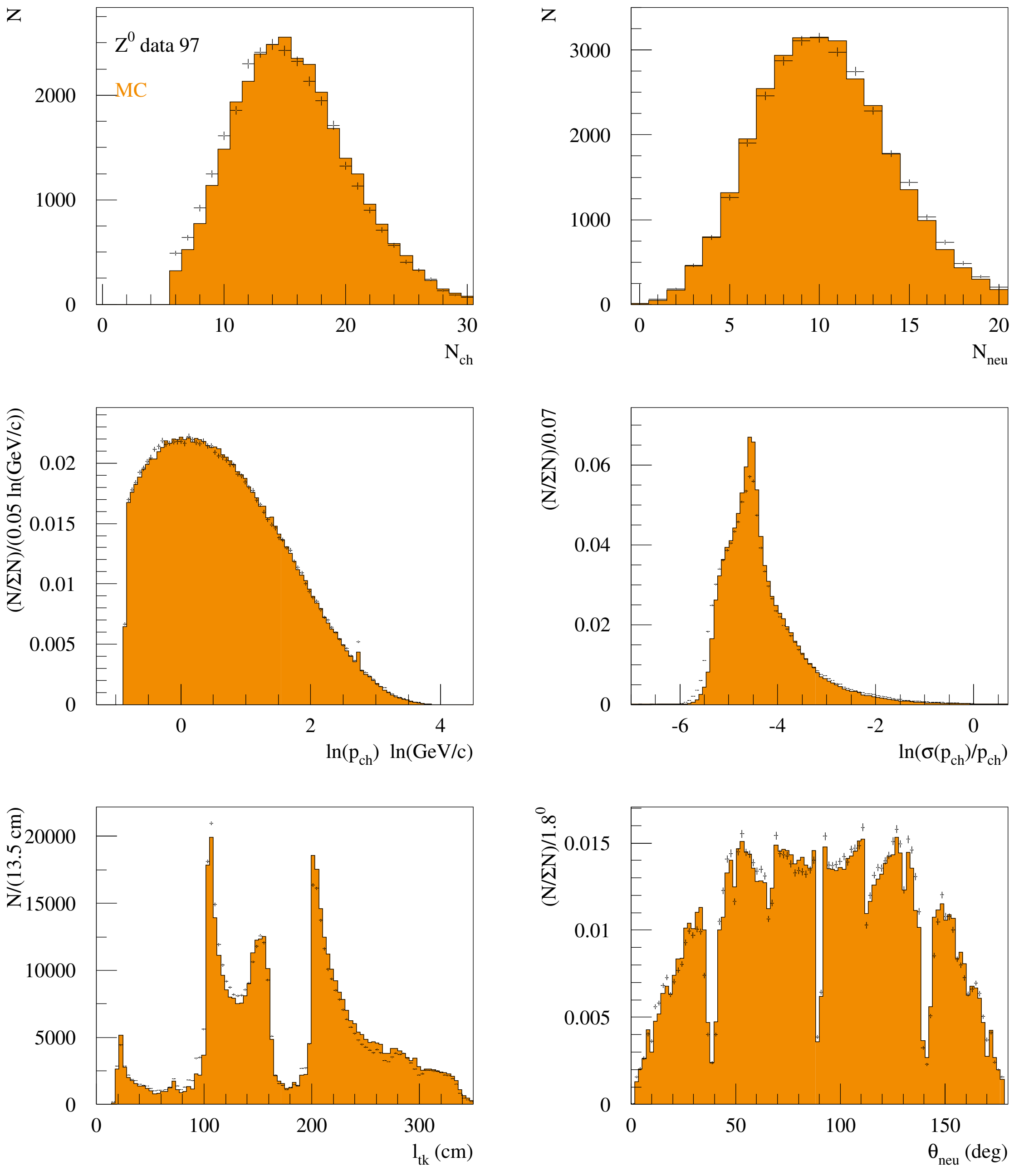

Figure 5.1: Comparison between hadronic Z^0 decays taken in 1997 and simulation for some general quantities related to the tracking. From top left to bottom right there are: the number of charged tracks, the number of neutral tracks, the momentum of charged tracks, the relative momentum error of charged tracks, the track length and the angular distribution of neutral tracks.

Figure 5.2: A computerised visualisation of a hadronic W^+W^- decay reconstructed with the DELPHI detector at the CMS energy of 172 GeV. Two jet pairs, each arising from $W^\pm \to q_1\bar{q}_2$ decay, are clearly distinguishable.

2.4). They can look similar to signal events if one or two hard gluons are emitted off the primary quarks. The probability to emit a hard gluon is about 10%. Notice that the cross-section for QCD events is about one order of magnitude higher than that of the signal events. Rejection of QCD events is the main task of W^+W^- event selection in the hadronic channel. The bulk of other background events is relatively easy removable. Mainly, this is achieved in a preselection of events where loose cuts are imposed on some kinematic quantities. After the preselection the loss of signal events is at the percent level, while background can be reduced by few orders of magnitude. At the second stage of the selection procedure a probabilistic approach is applied using events that survived the preselection. A loose preselection at the first stage has two important advantages; it improves the final separation and lowers the systematic uncertainty.

5.3.1 Preselection of events

The hadronic events are characterised by a relatively large number of tracks and jets that are well separated and isotropically distributed. There are no energetic neutrinos present, therefore, a large fraction of the initial collision energy must be reconstructed. Compared to the QCD events with radiative returns to the Z^0 mass, no energetic photons are expected in the signal events. Preselection criteria listed bellow follow these features.

- A quark jet contains about 12 reconstructed particles. By requiring at least 20 reconstructed tracks in events we shall not loose any good signal event. On the other hand, a huge background arising from $\gamma\gamma$ processes, Bhabha scattering, leptonic decays of produced Z^0 bosons, Compton scattering, and other processes will be rejected. Furthermore, this criterion enables a rather good separation from other decay channels of the W^+W^- events. The two photon processes sometimes also lead to more than 20 tracks, however, they mostly peak in the forward direction because of the boost. By requiring the transverse energy being larger than 50 GeV these events are suppressed. The transverse energy E_T is defined as $E_T = \sum_i \sqrt{{p_{xi}}^2 + {p_{yi}}^2}$, where p_i are momenta of particles and the sum runs over all detected particles.

- The sphericity S [32] is a standard measure of isotropy of events. It is calculated from eigenvectors of the sphericity tensor with elements:

$$S^{\alpha\beta} = \frac{\sum_i p_{\alpha i} \cdot p_{\beta i}}{\sum_i |\mathbf{p}_i|^2},$$

  where α and β correspond to the x, y and z components and the sum runs over all detected particles. An isotropic event approaches S=1 while an event in which particles are arranged around an axis has the sphericity value close to 0. We accepted events with the sphericity greater than 0.1. The expected distribution of the sphericity for signal and background events is shown in Figure 5.3 a). The presented distribution is obtained after the cuts on the multiplicity and the transverse energy have been applied.

- There should be at least three jets reconstructed by the LUCLUS algorithm with the value of the distance measure $d_{join} = 6.5$ (see Section 4.5). The value of d_{join} enables an efficient separation between signal and background events. The same value is used also in other decay channels.

- To test the signal hypothesis, particles are forced into four jets by varying the value of d_{join} until the required number of jets is reconstructed. If any of four jets has less than three particles attributed, the event is rejected (Figure 5.3 b)).

- A suppression of QCD events with radiative returns to the Z^0 mass is achieved by imposing a cut on the effective center of mass energy (see Section 4.9). At the CMS energy of 183 GeV the value of $\sqrt{s'}$ should exceed 120 GeV. In addition, events having neutral electromagnetic clusters with energies above 45 GeV are also rejected.

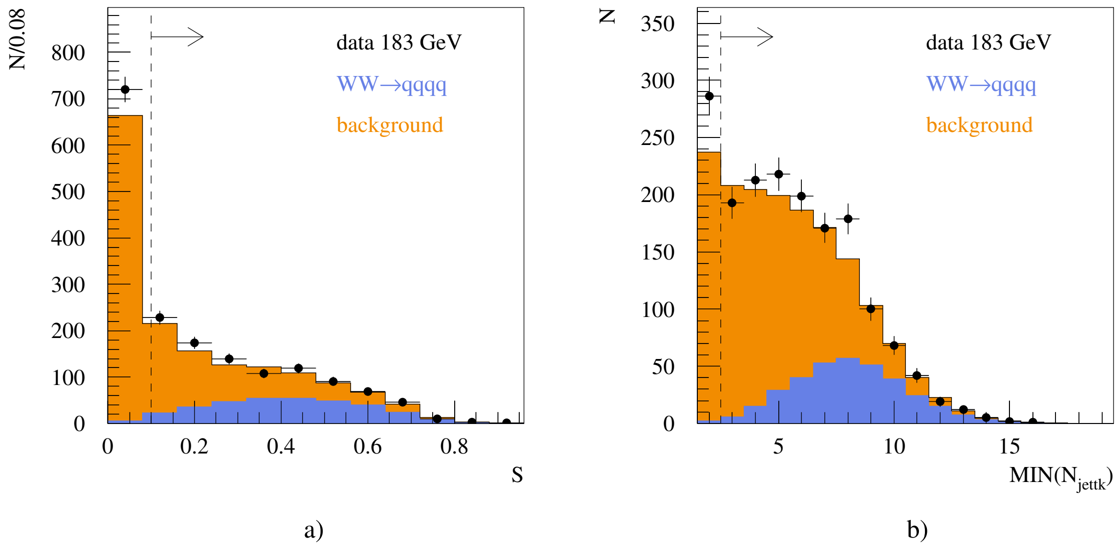

Figure 5.3: Distributions of quantities used in the preselection of hadronic channel at 183 GeV: **a)** sphericity of events, **b)** the minimum number of tracks attributed to one of hadronic jets within an event. The cuts imposed are presented with the vertical line.

5.3.2 Selection of events

After the preselection the number of accepted events is reduced by about four orders of magnitude while the loss of signal events is only about 10%. The remaining background consists mostly of QCD events. A further suppression of background is achieved with a probabilistic approach (see Section 4.10).

In general, many quantities that enable a selection of signal events, can be found. However, they are more or less correlated with each other and the most difficult task is to find a set of them that gives the best performance. The chosen set is presented in the following:

- In order to reject QCD events without an ISR and with no emission of hard gluons the sphericity is selected. This kind of QCD events is expected to have tracks arranged around an axis, thus resulting in a low value of the sphericity.

- The quantity s' is selected to measure the effective center of mass energy. The expected distribution of $\sqrt{s'}$ for background and signal events compared to the measured distribution at the CMS energy of 183 GeV is shown in Figure 5.4.

  If an energetic photon is emitted off the initial state, quark jets in QCD events are not colinear any more. However, if the photon is emitted down the beam pipe, the jets projected onto the transverse plane are still colinear. Therefore, a thrust axis is found in the transverse plane. It is defined as the one that maximises the sum of absolute particle momenta projected onto the axis [32]. As a separating variable the sum of squared transverse momenta of particles with respect to the thrust axis in the transverse plane (Δ_{2jet}) is used (Figure 5.4).

- To test compatibility of events with a four jet topology we used the value of $d_{join}(3,4)$ at the transition between four and three jets (Figure 5.4). As the second quantity of this type the minimum number of tracks attributed to any of the forced four jets is selected.

- The gluon jet is expected to be of low energy and close to the parent quark from which it is emitted. The presence of gluon jets is assessed by the variable D [75]:

$$D = \frac{E_{min}}{E_{min} \cdot (E_{max} - E_{min})} \cdot \theta_{min},$$

  where E_{min} and E_{max} are minimum and maximum energies of four jets and θ_{min} is the minimum angle between any two jets. The value of D is expected to be low for QCD events with hard gluons or other events not compatible with an isotropic four-jet topology (Figure 5.4).

- There are three possible pairings of four jets where a di-jet belongs to one of two $W^{\pm}$ bosons. We imposed the kinematicaly constrained 5C fit on each of the pairings (see Section 4.8). The combination with the smallest χ^2 of the fit is retained. Particles are then reassociated to the corrected jet directions. The achieved angular and momentum resolution of the fitted jets is shown in Figure 5.5. A flat tail in the distributions corresponds to misspaired jets. There are about 20% of them.

Based on the chosen pairing additional separating variables are constructed. The QCD events are expected to have two most energetic quark jets approximately back to back oriented. Since the other two, most probably gluon jets, are of lower energy, the pairing of one low and one high energy jet is likely to give rise to the smallest χ^2. Therefore, the angle between the two fastest jets, each belonging to a different di-jet pair, is expected to be close to 180^0 for QCD events (Figure 5.4).

As already discussed, fermions are approximately isotropically distributed around the direction of the parent $W^{\pm}$ boson in its rest frame. On the other hand, for the background events the phase space in which fermions escape in the forward-backward direction with respect to direction of the fitted boson is preferable. This has to do with the fact that one or two jets in the background events are usually more energetic than

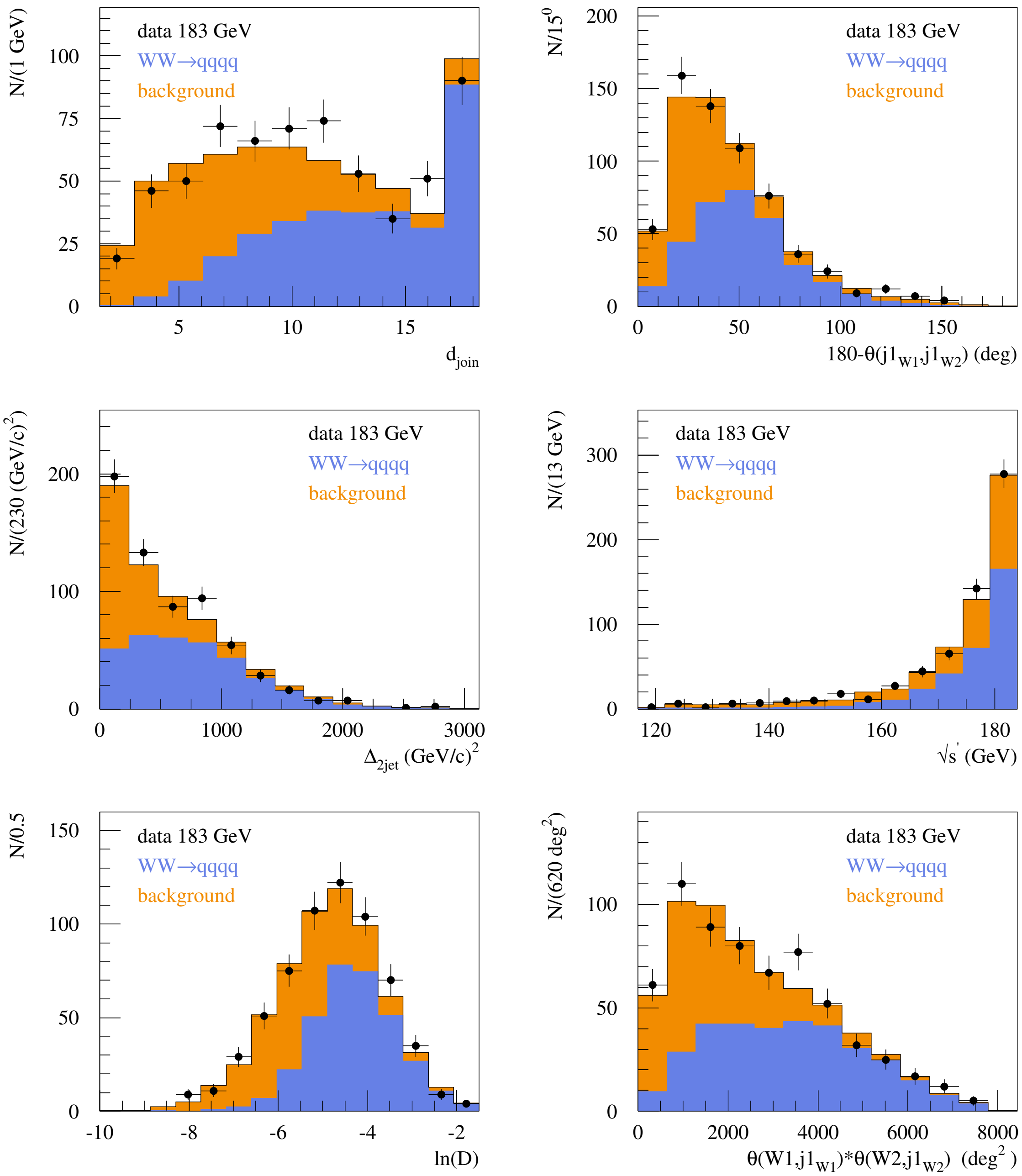

Figure 5.4: Distributions for some of quantities used to select hadronic decays at 183 GeV. From top left to bottom right there are: $d_{join}(3,4)$, the angle between the fastest jets from different $W^{\pm}$ bosons, the sum of transverse momenta with respect to the thrust axis in the transverse plane, the effective center of mass energy, the D variable, the product of angles between the jet and the parent $W^{\pm}$ boson.

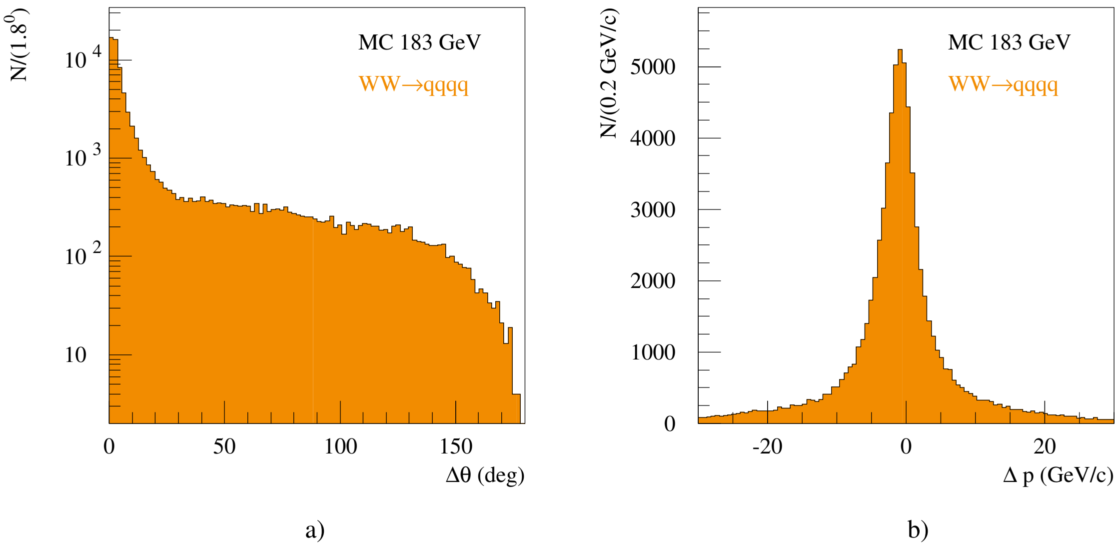

Figure 5.5: a) Angles between the generated and the reconstructed jets for combinations with the smallest χ^2 of the 5C constrained fit. **b)** The momentum difference between the generated and the fitted jet.

the other two. This feature is exploited by using the angle between the forward oriented jet and the direction of the fitted $W^\pm$ boson in its rest frame. The obtained angles from two $W^\pm$ bosons are multiplied as they are independent (Figure 5.4).

The simulated distributions of listed quantities for W^+W^- events and the complete set of background events are used to construct the probability P_{qqqq} that a given event is a hadronic W^+W^- event. In construction of the probability we do not distinguish between different types of background events (see Section 4.10). An event can be simultaneously candidate for more decay channels. To prevent double counting only the channel with the highest probability is retained. Distribution of P_{qqqq} for 183, 172 and 161 GeV samples is shown in Figure 5.6. In Figure 5.6 a) we can also see contributions from different background processes. The background is dominated by QCD events while other processes are almost negligible, as expected. The expected efficiency and purity of the event selection as a function of cut on value of P_{qqqq} is shown in Figure 5.6 d). To calculate the efficiency and the purity the SM cross-section for the W^+W^- production is assumed. The maximum product of efficiency and purity is about 0.62 and 0.60 for samples at 183 GeV and 172 GeV, respectively. At 161 GeV the cross-section for QCD events is higher while the cross-section for the W^+W^- production is already much lower. Therefore, the maximum product of efficiency and purity reaches about 0.36, only.

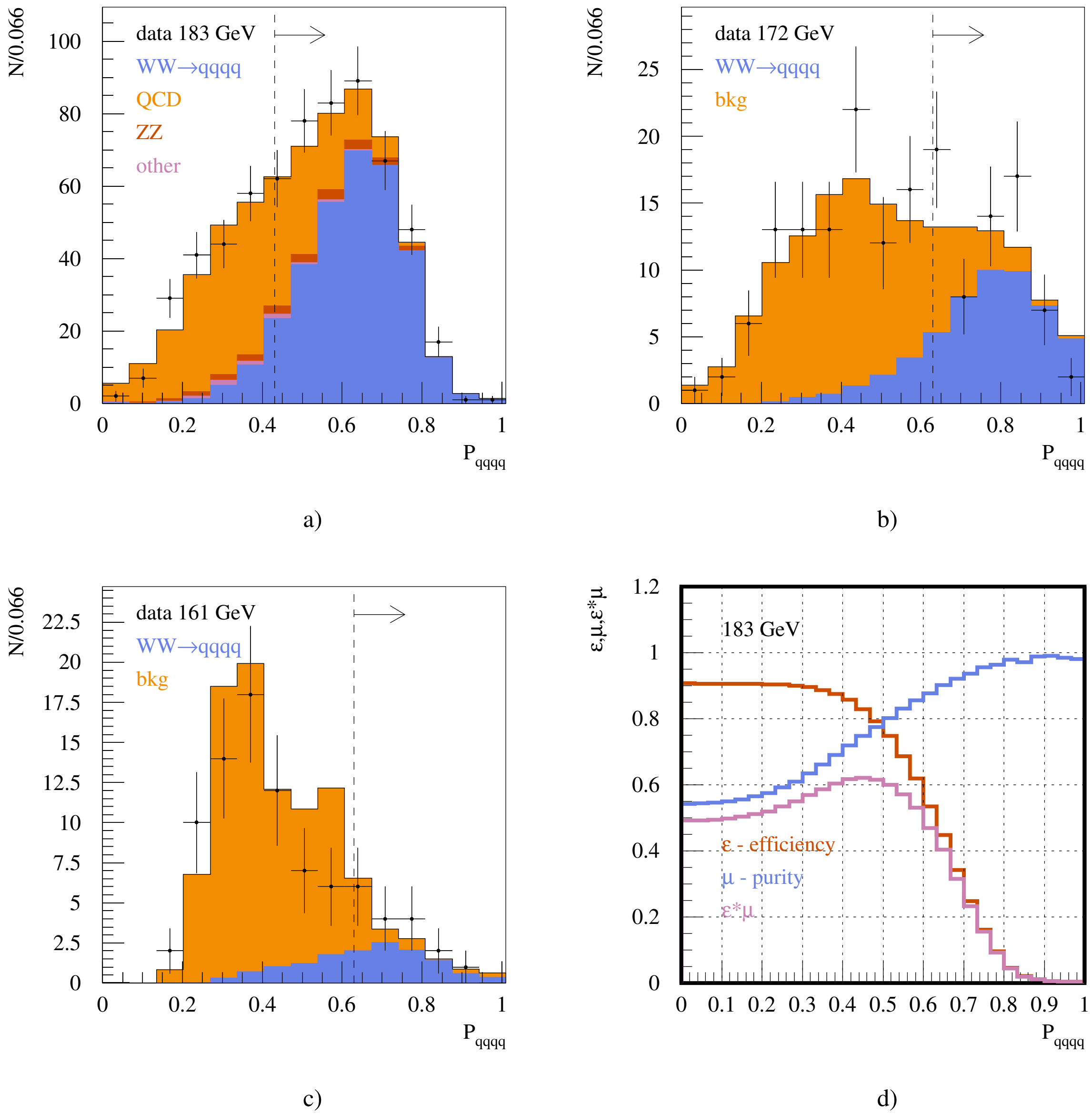

Figure 5.6: a) Distribution of event probability P_{qqqq} for hadronic channel at 183 GeV. The background contribution is divided into three sources: QCD events, Z^0Z^0 events and all the others. **b)** Distribution of P_{qqqq} at 172 GeV. **c)** Distribution of P_{qqqq} at 161 GeV. **d)** The expected efficiency and purity of the selection and the product of the two depending on cut on P_{qqqq} at 183 GeV. The vertical lines show the position of cut on P_{qqqq} which maximises the product of efficiency and purity.

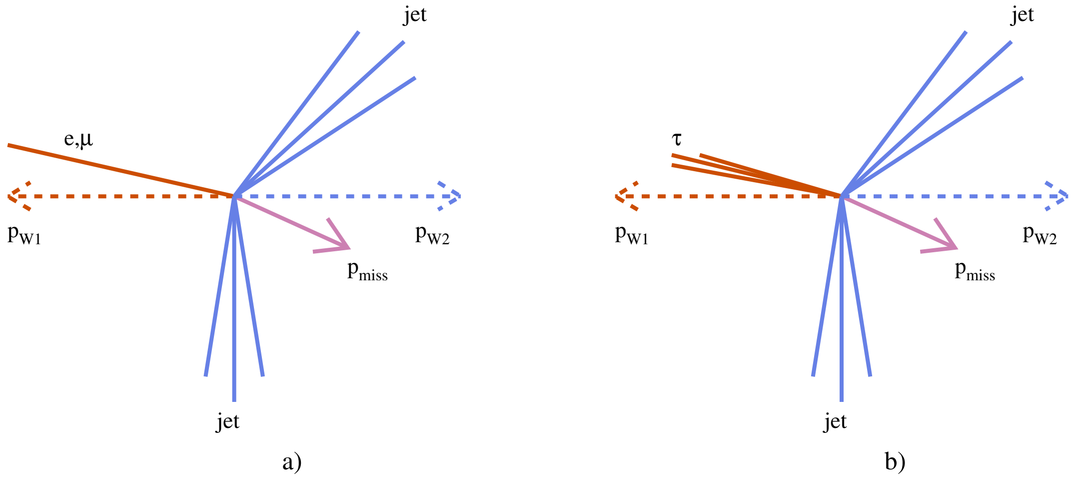

Figure 5.7: A typical topology of the mixed channel: **a)** the electron or muon decay channel and **b)** the τ channel.

5.4 Mixed channel

A typical topology of mixed decays is schematically presented in Figure 5.7 for e, μ and τ mode separately. The $W^\pm$ boson which decays hadronicaly leads to two approximately colinear jets. The neutrino produced in the leptonic decay will escape the detector unobserved. There will be a correspondingly large missing momentum pointing in the neutrino direction. The missing momentum p_{miss} is defined as the negative sum of momenta of all detected particles. The leptons like electrons or muons, are detected as single tracks with large momenta. In about 1/3 of the leptonic decays the τ lepton is produced. The τ lepton is unstable and promptly decays. The main decay modes are: $\tau^- \to \mu^-(e^-)\bar{\nu}_{\mu(e)}\nu_\tau$ ($\sim$ 35%), $\to h^-\nu_\tau$ n(neutrals) ($\sim 50\%$), $\to h_1^- h_2^- h_3^+ \nu_\tau$ n(neutrals) ($\sim 15\%$), where h stands for a charged hadron [11]. Apart from a relatively small fraction of decays with three charged particles in the final state, we expect one charged particle and at least one neutrino potentially accompanied by few neutral hadrons. In the leptonic decays of τ only one electron or muon is detectable while the rest of energy is carried by two neutrinos. These properties of the τ lepton slightly complicate an efficient reconstruction of $W^\pm \to \tau^\pm\nu_\tau$ decays. To achieve a good selection efficiency a separate selection criteria are needed for the τ and the electron or muon mode.

5.4.1 Preselection of events in $e^\pm, \mu^\pm$ channel

First, a $e^\pm$ or a $\mu^\pm$ candidate is selected among the reconstructed particles. In the mixed channel the lepton is expected to have a large momentum and to be isolated from other particles. A good efficiency is achieved if the particle j which minimises $\sum_{i;i\neq j} \sqrt{p_i}/{p_j}^2$ is chosen as the lepton candidate, whereby the sum runs over all other particles inside a 20^0 cone around the selected candidate. The probability for a faulty selection is only about 5%, although, the candidate is even not required to be a charged particle at this stage. This is important because just by coincidence a neutral particle can be selected in many background events. Such events are rejected in the next step by requiring the lepton to be a charged particle. Moreover, the candidate should be identified at least as a loose electron or a loose muon (Sections 4.7.1 and 4.7.2) with momentum larger than 20 GeV/c (Figure 5.8 b)). Events containing charged tracks with momenta above 1 GeV/c within a 5^0 cone around the lepton candidate are also rejected as well as those having a hadronic jet closer than 10^0 to the lepton candidate.

Remaining preselection criteria are related to a general event shape and are listed below:

- In addition to the lepton candidate, there should be at least 2 hadronic jets reconstructed (Figure 5.8 a)). The agreement between real data and simulation is rather poor in particular for lower number of jets. The reason for that might be that the cross-section for some easy removable background is not properly simulated. Namely, the agreement becomes much better once all preselection cuts are applied. It is a common feature of all decay channels that the matching between the simulation and real data becomes better after the preselection.
- To reject a large amount of Bhabha and $\gamma\gamma$ events the number of reconstructed tracks should exceed 12 and the transverse energy should be larger than $E_{CMS}/7$.
- The neutrino is characterised by a large missing momentum that is almost isotropically distributed over the polar angles. Radiative events and the events where the very forward tracks are not detected are expected to have the missing momentum oriented along the z axis. In the preselection the polar angle of the missing momentum of at least 15^0 is required.

5.4.2 Selection of events in $e^\pm, \mu^\pm$ channel

After the preselection the bulk of background represent the QCD events. A small contribution is expected also from $Z^0e^+e^-$, Z^0Z^0, and $W^\pm e^\pm\nu_e$ events (see Section 2.4) while other events are mainly rejected already at the preselection level.

Selection of quantities to be included into the event probability concentrates on three main points: properties of the lepton, the missing momentum due to the energetic neutrino, and a general event topology. The selected quantities are listed below:

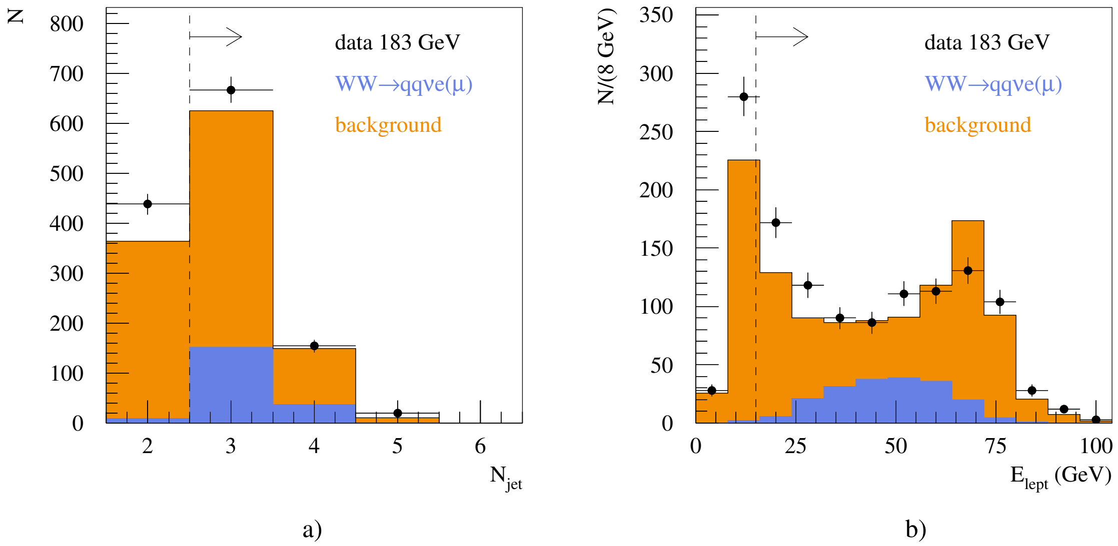

Figure 5.8: Distributions of quantities used in the preselection of $e^{\pm}, \mu^{\pm}$ channel at 183 GeV: **a)** the number of hadronic jets plus 1 for the lepton, **b)** the momentum of the lepton candidate.

- As a measure of the lepton isolation the energy deposited in a 10^0 cone around the lepton candidate is considered (Figure 5.9). The angle between the lepton and the closest charged track of momentum larger than 1 GeV/c serves for the same purpose (Figure 5.9). To enhance purity of the selection the lepton identification is added (Figure 5.9). If the lepton candidate is simultaneously identified as an electron and a muon the highest of either flags is retained.

- As the most important signature for the neutrino serves the polar angle of the missing momentum and the absolute value of the transverse missing momentum (Figure 5.9). Since the lepton and the neutrino are approximately colinear, the angle between the lepton candidate and the missing momentum is selected, in addition.

- Beside the lepton candidate, the remaining tracks are forced into two jets. The two jets and the lepton are the input of the 5C fit. An overall compatibility of events with the topology of mixed decays is accomplished by the χ^2 of the constrained fit (Figure 5.9). The isotropic distribution of final fermions is checked by using the angle between the two hadronic jets as well as the angle between the lepton candidate and the closest hadronic jet.

  The charge of the $W^{\pm}$ boson is efficiently determined by the charge of the lepton candidate. Hence, the polar angle of W^+ is exploited. Its discriminating power steams from a large charge asymmetry expected in the signal events (see Section

2.2.1) and a relatively isotropic distribution of background events.

- The radiative events are rejected by the effective center of mass energy $\sqrt{s'}$. However, $\sqrt{s'}$ is not as efficient quantity as it is in the hadronic channel because of the undetected neutrino in the signal events. Therefore, an additional separating variable to suppress the radiative events is constructed. Events are forced into two jets using only the transverse components of particle momenta. The angle between the two jets is expected to be close to 180^0 if the radiated photon escapes down the beam pipe (Figure 5.9).

Distribution of the probability $P_{qq\nu e(\mu)}$ (when the considered mode is the most probable among all) is presented in Figure 5.10 for 183 and 172 GeV samples. Migrations from the τ decay channel are the most severe non-signal events. They are harmless as we are interested only in the common cross-section for the mixed channel. Neglecting the τ migrations, the maximal product of efficiency and purity is about 0.78 ($\epsilon = 85\%$ and $\mu = 91\%$) at the CMS energy of 183 GeV. The accepted background is composed of QCD events with smaller fractions of $Z^0e^+e^-$, Z^0Z^0, and $W^\pm e^\pm \nu_e$ events.

5.4.3 Preselection of events in $\tau^\pm$ channel

Most of properties of the $\tau^\pm$ decay channel are similar to the $e^\pm, \mu^\pm$ decay channel and so are the preselection and the selection criteria. Since the branching ratio of the τ lepton into three charged particles amounts to only about 15%, the selection criteria are not designed to account for this decay mode. In other decay channels the τ lepton decays into one charged particle potentially accompanied by few neutral particles.

We will characterise the τ lepton by a single particle. This particle is selected as the one which minimises $\sum_{i;i\neq j} \sqrt{p_i}/{p_j}^{0.2}$, where the sum runs over all charged particles in a 30^0 cone around the candidate j. The optimal powers used to weight momenta of particles are obtained from the simulation. Opposite to the lepton selection in the $e^\pm, \mu^\pm$ decay channel, the main weight is placed on the isolation from charged particles while momentum of the candidate has only a weak impact to the sum. Once the candidate has been chosen we require that it is a charged particle with the momentum larger than 10 GeV/c. Events are then forced into three jets and the 5C fit is performed. The jet that contains the τ candidate track is considered as the τ jet. The number of particles attributed to the τ jet should not exceed 7. Since the τ jets are expected to be isolated, events with a hadronic jet closer than 20^0 to the τ jet are rejected.

Most of remaining preselection criteria are similar to those used in the $e^\pm, \mu^\pm$ decay channel. These are: at least three reconstructed jets, the polar angle of the missing momentum larger than 10^0 (Figure 5.11 a)), the reconstructed energy between $E_{CMS}/4.5$ and

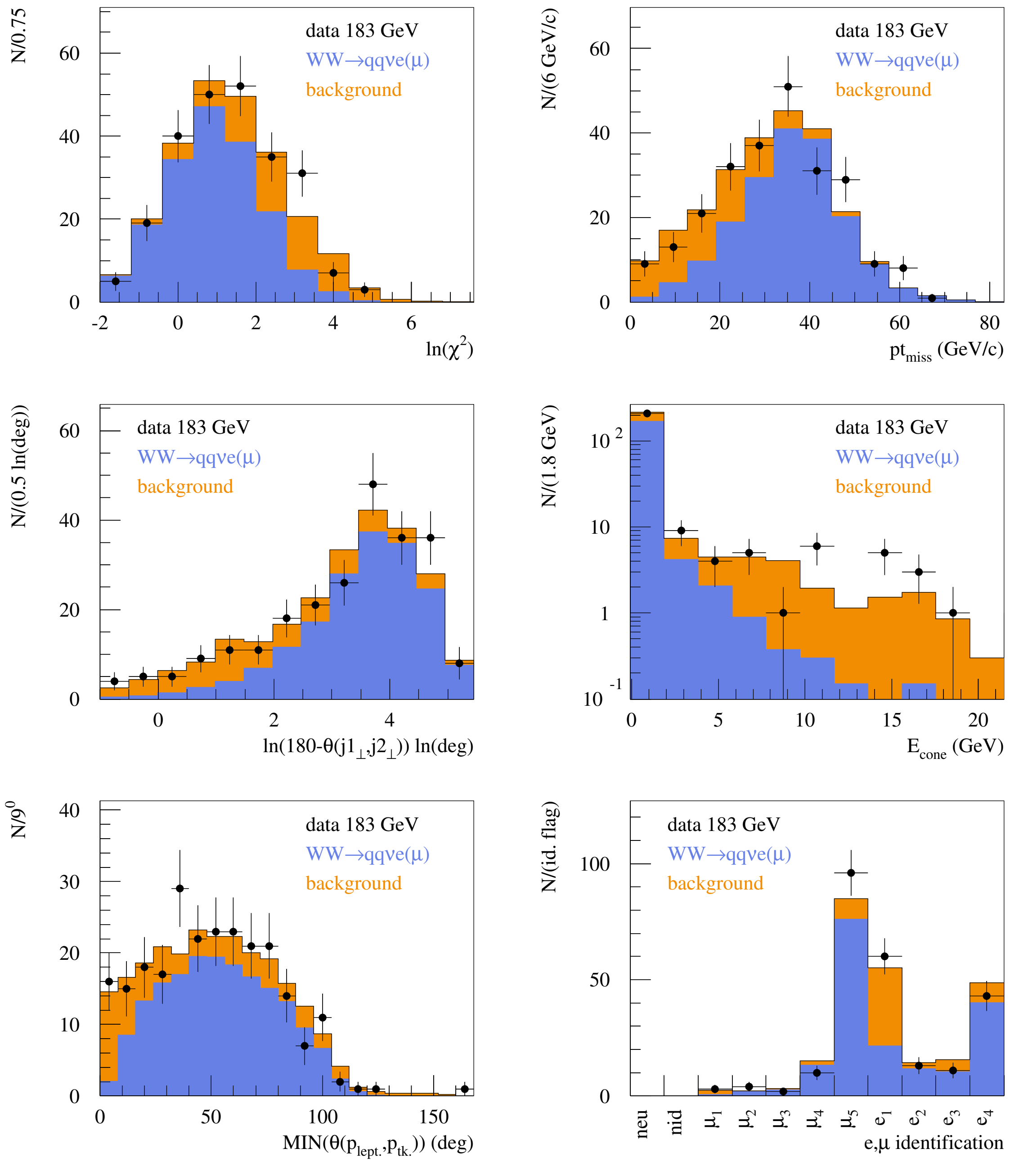

Figure 5.9: Distributions of quantities used to select events in the mixed channel at 183 GeV. From top left to bottom right there are: χ^2 of the 5C fit, the transverse missing momentum, the angle between two forced jets in the transverse plane, the energy in the 10^0 cone around the lepton, the smallest angle between a track of $p > 1$ GeV/c and the lepton, the electron and muon identification (neu=neutral, nid=no identification, $\mu_1 - \mu_5$ are the muon identification flags, $e_1 - e_4$ are the electron identification flags).

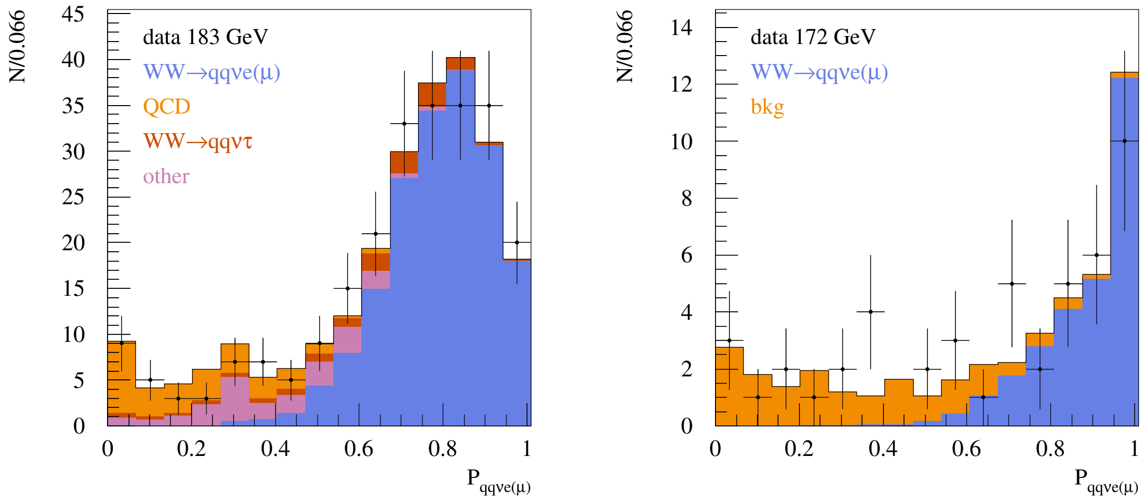

a) b)

Figure 5.10: a) Distribution of the event probability $P_{qq\nu e(\mu)}$ for the mixed channel with an electron or a muon at 183 GeV. **b)** The same for 172 GeV sample.

$E_{CMS}/0.8$, the angle between two hadronic jets larger than 60^0, at least 12 reconstructed tracks, and the transverse energy larger than $E_{CMS}/5$.

5.4.4 Selection of events in $\tau^{\pm}$ channel

Quantities used to construct the event probability are similar to those in the $e^{\pm}$, $\mu^{\pm}$ decay channel. We will briefly list them with an emphasis on differences between two channels.

As a criterion for the isolation of the τ candidate from other charged tracks we constructed the quantity $\sum_{i;i \neq j} \sqrt{p_i}\, cos\theta_{ij}$, where the sum runs over all charged tracks within a 20^0 cone around the τ candidate j. Since the τ jets are expected to contain a small number of particles, the multiplicity of τ jets is also used (Figure 5.12).

Other selected quantities are related to an overall event shape and are as follows: χ^2 of the 5C fit, the number of reconstructed jets, the transverse missing momentum, the sphericity, the aplanarity of event, the effective center of mass energy, the angle between the missing energy and the τ jet, electron or muon identification of the τ candidate, and the polar angle of the W^+ boson, where the charge of the $W^{\pm}$ boson is determined by the charge of the τ candidate. (Figure 5.12 b)). The aplanarity A measures the momentum component out of the event plane. It is defined as $A = \frac{1}{3}\lambda$, where λ is the smallest of three eigenvalues of the sphericity tensor [32]. The QCD events with ISR photons emitted along the beam pipe tend to have $A \sim 0$.

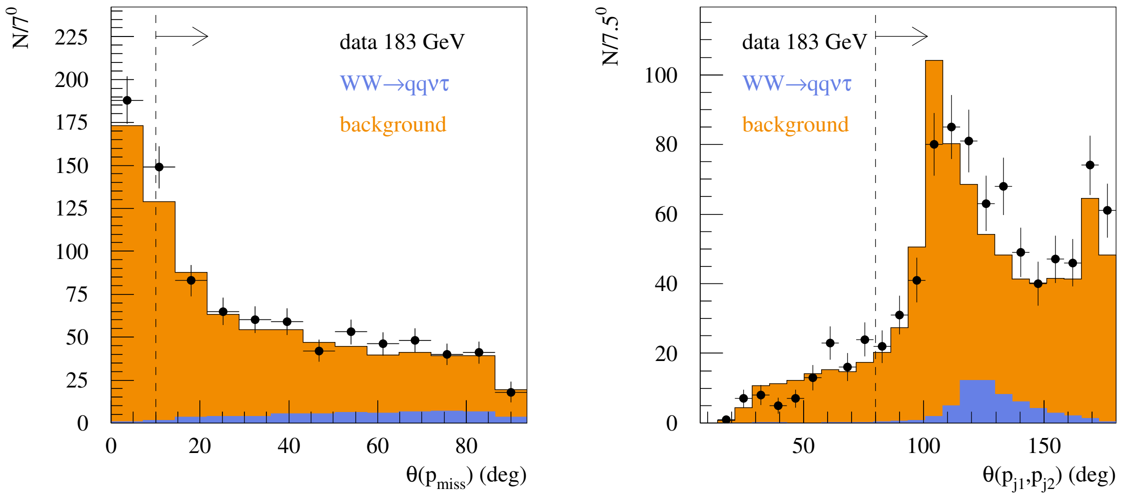

a) b)

Figure 5.11: Distribution of quantities used in the preselection of the mixed channel with the τ lepton at 183 GeV: **a)** the polar angle of missing momentum, **b)** angle between hadronic jets.

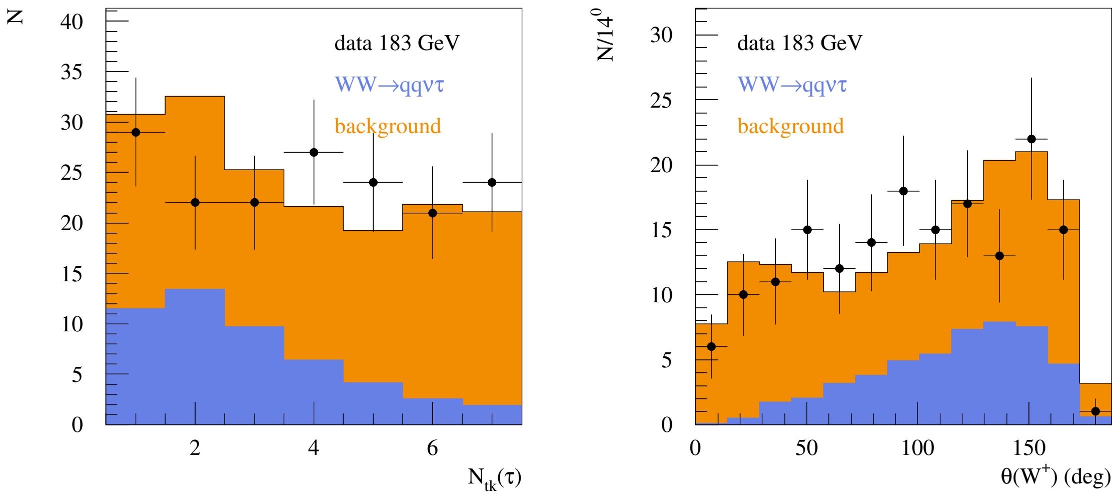

a) b)

Figure 5.12: **a)** The number of tracks attributed to the τ jet. **b)** The polar angle of W^+ boson.

By using the listed quantities in the construction of probability $P_{qq\nu\tau}$ we achieve the maximal product of efficiency and purity of about 0.40, whereby migrations from the $e^\pm, \mu^\pm$ channel are ignored. The QCD background in this channel is expected to be more severe than in the $e^\pm, \mu^\pm$ channel. The sum of two distributions, $P_{qq\nu\tau}$ and $P_{qq\nu e(\mu)}$, for 161, 172, and 183 GeV samples is shown in Figure 5.13 together with the corresponding efficiencies and purities. The maximal expected product of efficiency and purity of 0.65 is found at the CMS energy of 183 GeV. The value is slightly higher than the one in the hadronic channel thanks to a high purity of about 91%.

5.5 Leptonic channel

A shematic illustration of a fully leptonic decay is shown in Figure 5.14. If none of the $W^\pm$ bosons decays into the τ lepton only two highly energetic and acolinear tracks are produced. The presence of the τ lepton introduces a somewhat different topology. Based on the number of produced τ leptons there are three different channels. We shall proceed differently and distinguish three effective modes: muon mode ($l\nu l\nu(\mu)$), mode with two tracks ($l\nu l\nu(2\text{tk})$), and the rest of leptonic decays ($l\nu l\nu(\text{rest})$). The division is based on different separating powers among the selected modes.

5.5.1 Preselection and selection of events

In principle, the topology of leptonic channel provides a rather clean and efficient separation from the background sources. However, the branching ratio is small and there is a certain probability that either of two charged tracks are not observed, in particular, in the very forward region. The first fact lowers the purity and the second one the efficiency of selection.

As opposed to the preceding channels, the QCD background is not the dominant in the leptonic channel. The most severe background is expected to arise from $\gamma\gamma$ events and leptonic decays of produced Z^0 bosons. There is also a large number of Bhabha events that have to be efficiently rejected. As far as $\gamma\gamma$ events are concerned, they are modeled phenomenologically with a large theoretical uncertainty. There is also a lack of measurements of $\gamma\gamma$ events at higher CMS energies to which we could refer. In order to keep the systematic uncertainty due to the simulation of background processes low enough, it is preferred to keep the purity high at the expense of a lower selection efficiency. The preselection cuts are therefore tighter and most of selection is done already at this level. For data collected at the CMS energies of 161 and 172 GeV the number of selected signal events is expected to be below 10. Correspondingly, the number of available simulated events is also relatively low and the construction of probability is subject to large statistical

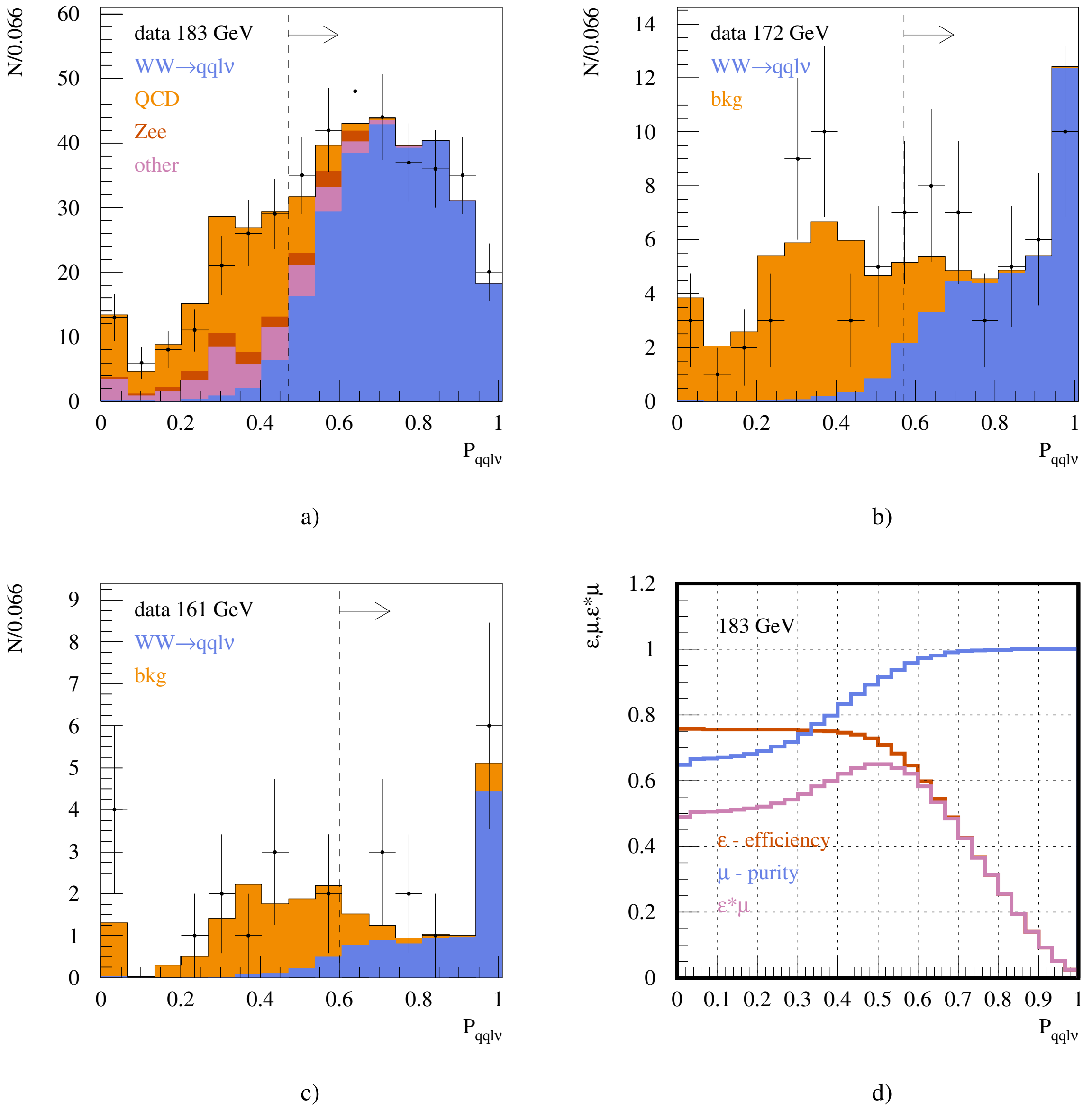

Figure 5.13: **a)** Distribution of event probability $P_{ql\nu} = P_{qq\nu\tau} + P_{qq\nu e(\mu)}$ for the mixed channel at the CMS energy of 183 GeV. **b)** Distribution of $P_{qql\nu}$ at 172 GeV. **c)** Distribution of $P_{qql\nu}$ at 161 GeV. **d)** The expected efficiencies and purities and the product of the two depending on cut on $P_{qql\nu}$ at 183 GeV. The vertical lines show the position of cut on $P_{qql\nu}$ which maximises the product of efficiency and purity.

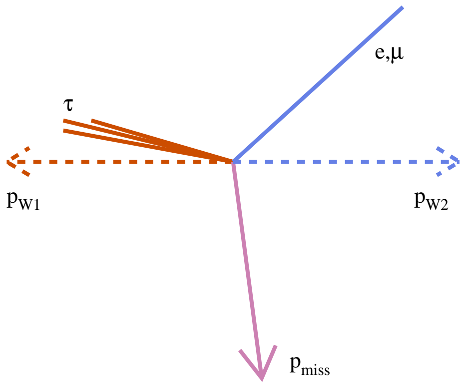

Figure 5.14: A typical topology of leptonic channel.

fluctuations. Therefore, the cuts for 161 and 172 GeV samples are tighter in order to use the number of selected events for the cross-section measurement, without involving the probability.

In the following we will qualitatively describe the quantities used in the preselection as well as those used in the construction of event probability for 183 GeV sample. A more quantitative overview of preselection and selection criteria for all energies and subchannels is displayed in Tables 5.2, 5.3, and 5.4.

In an event with a low number of tracks we require at least two reconstructed charged tracks and exactly two reconstructed jets. In every reconstructed jet the fastest charged particle is chosen to represent the lepton. To reject the background that points into the forward direction the transverse energy must be large. Non radiative Bhabha scattering and leptonic Z^0 decays are rejected by cutting on the interjet angle $\theta(j_1 - j_2)$ (Figure 5.15 a)). Due to two energetic neutrinos in the signal events the missing momentum points in the central region of the detector with a large transverse component (Figure 5.15 b) and 5.16 b)). The most resistant background represent radiative leptonic $Z^0(\gamma)$ decays as well as $\gamma\gamma$ events. The effective center of mass energy is not a very efficient quantity because of a large missing momentum expected in the signal events. However, if a colinear background event is boosted along the z direction, the two jets and the z axis still lie in the same plane. As a measure of the planarity we constructed the quantity $p' = \arccos(|\mathbf{p}_1 \times \mathbf{p}_2| \cdot \mathbf{z})$, where $\mathbf{p}_1$ and $\mathbf{p}_2$ are normalised directions of jets and $\mathbf{z} = (0, 0, 1)$. The value of p' is the angle between the z direction and the vector perpendicular onto the plane spanned by the vectors $\mathbf{p}_1$ and $\mathbf{p}_2$. For most of background events the angle is expected to be close to 90^0. As seen in Figure 5.15 a), p' is a very efficient variable that enables rejection of background over signal events of about 20:1. The same variable is again shown in Figure 5.16 a) for events that survive the preselection in the muon channel.

Apart from the presented general criteria, there are additional requirements specific to every subchannel.

Muon channel

Presence of a loosely identified muon with momentum larger than 20 GeV/c and an additional charged track of more than 10 GeV/c is a signature of the leptonic decay with at least one muon produced. These two requirements are sufficient to obtain a good purity in the preselection. For the calculation of probability the invariant mass of the whole system is used to separate against leptonic Z^0 or Z^0Z^0 decays. Jets produced by decays of τ leptons are expected to be narrow. The broadness of jets is estimated by summing up the squared transverse momenta of particles with respect to the jet direction. The quantity is used in the construction of the probability, too.

Two track channel

If an event is not selected in the muon channel, it is a candidate for the two track mode if it contains only two charged tracks with sufficiently high momenta (Figure 5.15 c)). For the event probability the polar angle of the leading lepton is used to separate against Bhabha events. No other criteria are needed because the accepted events are expected to be very pure. Unfortunately, they represent only about 10% of all selected leptonic events.

The rest of leptonic decays

Leptonic events that are not selected in the preceding channels usually contain at least one τ lepton and no muons. There is no single efficient variable to select these events. Therefore, cuts are made tighter to suppress background that is initially larger in this channel. In addition to the common criteria described above, a relatively large polar angle of the leading track is required in order to further reject background events peaked in the forward region. In the event probability we also take into account the lepton identification of two candidates, the maximal jet broadness of either reconstructed jets, and the aplanarity of event (Figure 5.18).

Results

In the 161 GeV sample only 1 event meets the above criteria. The event is selected in the muon channel. The simulation predicts 0.5 background events and 1.9 signal events in all channels together.

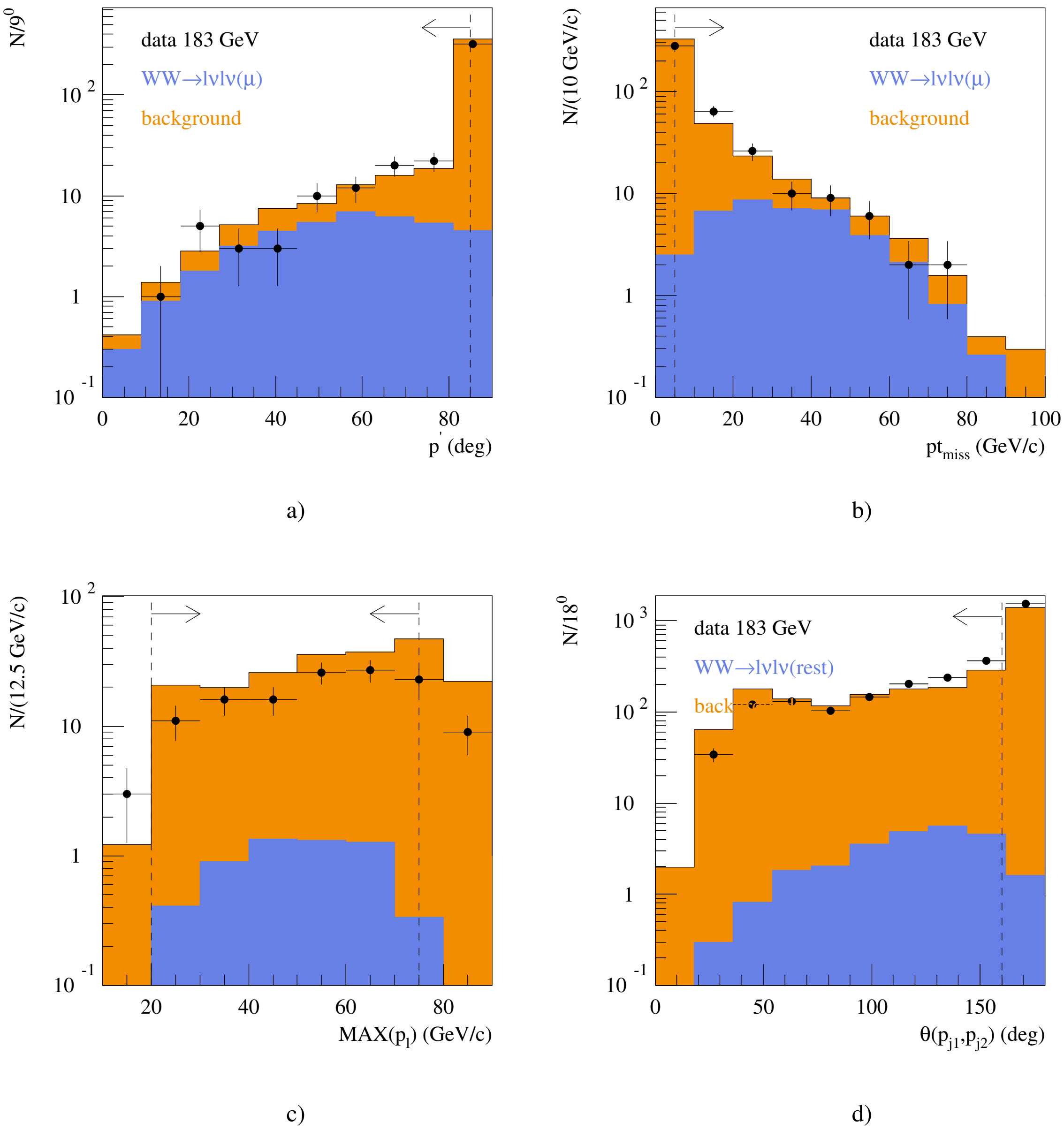

Figure 5.15: Distribution of quantities used in the preselection of the leptonic channel at 183 GeV. **a)** The quantity p' in the muon channel. **b)** The transverse missing momentum in the muon channel. **c)** The energy of the fastest track in the two track mode. **d)** The angle between two jets in the rest of leptonic events.

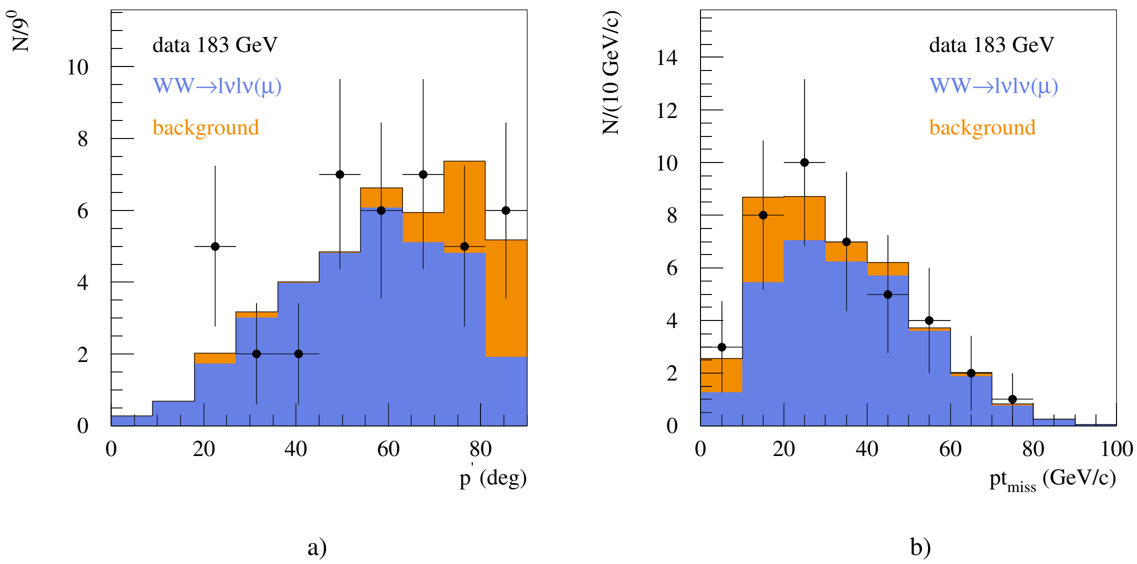

Figure 5.16: Distribution of quantities used to construct the event probability in the muon channel at 183 GeV: **a)** p', **b)** the transverse missing momentum.

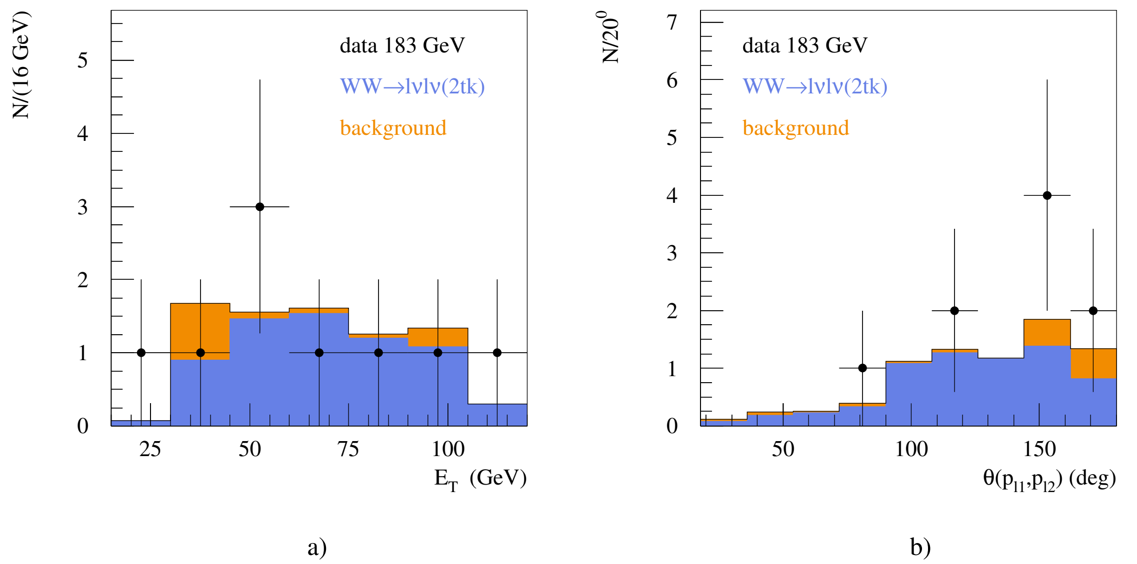

Figure 5.17: Distribution of quantities used to construct the event probability in the two track channel at 183 GeV: **a)** the transverse energy, **b)** the angle between leptons .

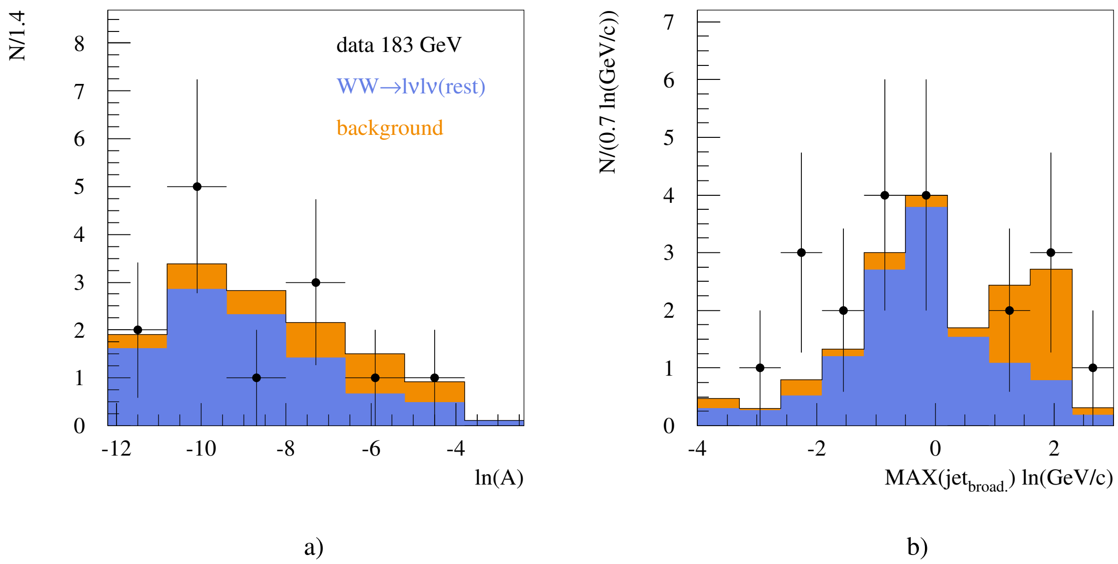

Figure 5.18: Distribution of quantities used to construct the event probability in the rest of leptonic decays at 183 GeV: **a)** the aplanarity, **b)** the maximal jet broadness of either jets.

Variable	161 GeV	172 GeV	183 GeV	$P_{l\nu l\nu(\mu)}$
$\mathrm{N_{tracks}}$	< 8	< 8	< 8	-
$\mathrm{N_{charged\ tracks}}$	> 1	> 1	> 1	-
$\mathrm{N_{jet}}$	2	2	2	-
$\mathrm{E_T}$	$> E_{CMS}/5$	$> E_{CMS}/5$	$> E_{CMS}/9$	-
$\mathrm{p_T^{miss}}$ (GeV/c)	> 5	> 5	> 5	+
$\theta(\mathrm{j_1, j_2})$ (deg)	< 170	< 170	< 170	-
p_μ(GeV/c)	$20 < x < 55$	$20 < x < 65$	$20 < x < 75$	+
p(non μ) (GeV/c)	$10 < x < 55$	$10 < x < 65$	$10 < x < 75$	+
p$'$ (deg)	< 75	< 80	< 85	+
μ identification	tight	tight	loose	-
$\theta(\mathrm{p_{miss}})$	.	.	.	+
jet broadness	.	.	.	+
ident. of second lept.	.	.	.	+
$\mathrm{m_{inv.}}$	.	.	.	+
$\theta(p_\mu, z)$	.	.	.	+

Table 5.2: Quantities and cuts used for the muon channel at 161, 172 and 183 GeV. The probability $P_{l\nu l\nu(\mu)}$ is calculated only for the 183 GeV sample.

Variable	161 GeV	172 GeV	183 GeV	$P_{l\nu l\nu(2tk)}$
$\mathrm{N_{tracks}}$	2	2	2	-
$\mathrm{N_{charged\ tracks}}$	2	2	2	-
$\mathrm{E_T}$	$> E_{CMS}/6$	$> E_{CMS}/6$	$> E_{CMS}/6$	+
$\theta(\mathrm{l_1, l_2})$ (deg)	< 150	< 160	< 175	+
$\mathrm{p(l_{fast})}$ (GeV/c)	$20 < x < 55$	$20 < x < 65$	$20 < x < 75$	+
$\mathrm{p(l_{slow})}$ (GeV/c)	$5 < x < 55$	$5 < x < 55$	$5 < x < 55$	-
$\mathrm{p'}$ (deg)	< 85	< 85	< 85	+
$\theta(\mathrm{p_{miss}})$ (deg)	> 30	> 15	> 10	-
$\mathrm{p_T^{miss}}$	.	.	.	+
$\theta(\mathrm{l_{fast}, z})$	.	.	.	+

Table 5.3: Quantities and cuts used for the two track channel at 161, 172 and 183 GeV. The probability $P_{l\nu l\nu(2tk)}$ is calculated only for the 183 GeV sample.

Variable	161 GeV	172 GeV	183 GeV	$P_{l\nu l\nu(rest)}$
$\mathrm{N_{tracks}}$	< 7	< 9	< 9	-
$\mathrm{N_{charged\ tracks}}$	> 1	> 1	> 1	-
$\mathrm{N_{jet}}$	2	2	2	-
$\mathrm{E_T}$(charged)	$> E_{CMS}/10$	$> E_{CMS}/10$	$> E_{CMS}/10$	-
$\mathrm{p_T^{miss}}$ (GeV/c)	> 10	> 10	> 10	+
$\theta(\mathrm{j_1, j_2})$ (deg)	< 150	< 160	< 160	+
$\mathrm{p(l_{fast})}$ (GeV/c)	$20 < x < 55$	$20 < x < 65$	$20 < x < 75$	-
$\mathrm{p'}$ (deg)	< 75	< 80	< 85	+
$\theta(\mathrm{p_{miss}})$ (deg)	> 15	> 15	> 15	-
$\theta(\mathrm{l_{fast}, z})$	> 30	> 30	> 30	+
$\mathrm{p(l_{slow})}$ (GeV/c)	.	.	.	+
sphericity	.	.	.	+
ident. of $\mathrm{l_{fast}}$	.	.	.	+
ident. of $\mathrm{l_{slow}}$	.	.	.	+
$\mathrm{m_{inv.}}$ of jets	.	.	.	+

Table 5.4: Quantities and cuts used for the rest of leptonic decays at 161, 172 and 183 GeV. The probability $P_{l\nu l\nu(rest)}$ is calculated only for the 183 GeV sample.

At the CMS energy of 172 GeV 8 events are selected, whereby 8.1 are expected from the leptonic W^+W^- decays and additional 1.4 from the background. The expected efficiency of the selection is 62% with the purity of 85%.

Distribution of event probabilities $P_{l\nu l\nu(\mu)}$, $P_{l\nu l\nu(2tk)}$, and $P_{l\nu l\nu(rest)}$ at the CMS energy of 183 GeV is shown in Figure 5.19 together with the corresponding efficiencies and purities. The maximal product of the two is 0.54. This is just slightly higher as it would be obtained if only the preselection was used ($P_{l\nu l\nu} = 0$). However, the purity is higher if the probability is used. This is important because the systematic uncertainty due to the simulation of background processes is expected to be high.

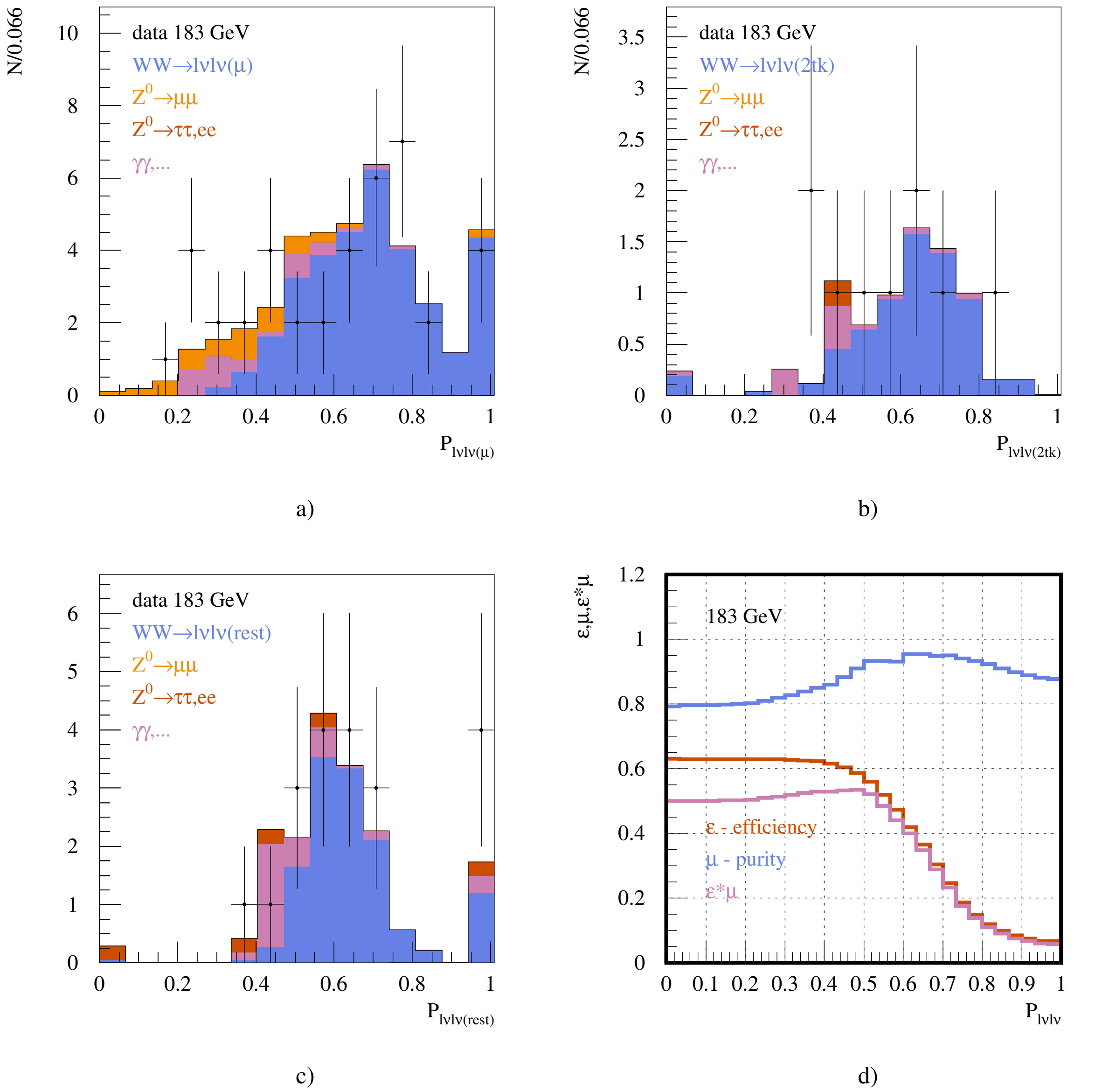

Figure 5.19: **a)** Distribution of event probability $P_{l\nu l\nu(\mu)}$ for the muon channel at 183 GeV. **b)** The probability $P_{l\nu l\nu(2tk)}$ for the two track channel at 183 GeV. **c)** The probability $P_{l\nu l\nu(rest)}$ for the rest of leptonic events at 183 GeV. **d)** The expected efficiency and purity of the selection in all subchannels together and the product of the two depending on cut on $P_{l\nu l\nu} = P_{l\nu l\nu(\mu)} + P_{l\nu l\nu(2tk)} + P_{l\nu l\nu(rest)}$.

6

Interpretation of selected events: σ_{WW}, $Br_{W\to had}$, $|V_{cs}|$

6.1 Likelihood fit and results

Estimates of the W^+W^- cross-section, the hadronic branching ratio of the $W^\pm$ bosons, and consequently $|V_{cs}|$ are obtained by the likelihood fit of the expected to the measured distributions of event probabilities P_{qqqq}, $P_{qq\nu e(\mu)}$, $P_{qq\nu(\tau)}$, $P_{l\nu l\nu(\mu)}$, $P_{l\nu l\nu(2tk)}$, and $P_{l\nu l\nu(rest)}$, presented in Chapter 5. In the leptonic channel at the CMS energies of 161 and 172 GeV the number of selected events after imposing the preselection cuts is used.

The number of observed events in each bin is assumed to obey the Poisson distribution; the probability $P_j^k(\bar{N}_j^k, N_j^k)$ that we measured N_j^k events in the k-th bin and j-th decay channel, if $\bar{N}_j^k$ events are expected, is given by:

$$P_j^k(\bar{N}_j^k, N_j^k) = \frac{e^{-\bar{N}_j^k} \cdot \bar{N}_j^{k\ N_j^k}}{N_j^k!}, \tag{6.1}$$

where the number of expected events is expressed as:

$$\bar{N}_j^k = \mathcal{L}(\sigma_j^k(bkg) + \sum_i \epsilon_{i,j}^k \cdot \sigma_{WW} \cdot \frac{Br_{WW\to i}}{f_i^{CC03}}). \tag{6.2}$$

Here, $\mathcal{L}$ is the integrated luminosity (see Table 5.1) and $\sigma_j^k(bkg)$ is the accepted cross-section for background events in the given bin and channel. $\epsilon_{i,j}^k$ is the probability that an event produced in the i-th channel is reconstructed in the k-th bin of the j-th channel ($i = qqqq$, $qq\nu e$, $qq\nu\mu(\tau)$, $l\nu l\nu$ while $j = qqqq$, $qq\nu e$, $qq\nu\mu$, $qq\nu\tau$, $l\nu l\nu(\mu)$, $l\nu l\nu(2tk)$, $l\nu l\nu(rest)$). The correction factors f_i^{CC03} account for interferences between four-fermion final states that are not taken into account in the simulation (see Section 2.2.2). Values of the correction factors are listed in Table 6.2 for all energies and decay channels. The method used to obtain f_i^{CC03} is discussed in the next section. The branching ratios $Br_{WW\to i}$ can be expressed with the hadronic branching ratio of the $W^\pm$ bosons ($Br_{W\to had}$) as follows (see Eq.

2.19): $Br_{WW\to qqqq} = (Br_{W\to had})^2$, $Br_{WW\to qq\nu e,(\mu),(\tau)} = 2/3\cdot Br_{W\to had}\cdot(1-Br_{W\to had})$, and $Br_{WW\to l\nu l\nu} = (1-Br_{W\to had})^2$. Hereby we assumed the lepton universality which implies almost equal branching ratios regardless of the lepton type. Differences due to different masses of leptons are at the permil level and are neglected. According to Eqs. 2.17 and 2.18 we can further express $Br_{W\to had}$ as a function of $|V_{cs}|$. Thus, we are left with only two independent free parameters σ_{WW} and $Br_{W\to had}$ (or $|V_{cs}|$ instead of the latter) that are determined by maximisation of the likelihood function. The likelihood function $\mathcal{L}$ is the product of probabilities P_j^k (Eq. 6.1) for all bins and channels:

$$\mathcal{L} = \prod_{j,k} P_j^k \tag{6.3}$$

Maximisation of $\mathcal{L}$ is performed numerically by using the program MINUIT [29] from the CERN program library. The fit was performed separately for 161, 172 and 183 GeV samples as well as for the combined likelihood function from all three CMS energies. Results of the fit are presented in Table 6.1.

Apart from σ_{WW}, $Br_{W\to had}$, and $|V_{cs}|$, we can obtain additional quantities by only a slight modification of the expression 6.2. The partial cross-sections $\sigma_{WW\to i}$ for the main decay channels are obtained by replacing the product $\sigma_{WW}\cdot Br_{WW\to i}$ by $\sigma_{WW\to i}$. To measure the total cross-section for the W^+W^- production with the imposed SM branching ratios we insert the SM values of $Br_{WW\to i}$ in Eq. 6.2 and leave σ_{WW} as the only free parameter. These additional results are also presented in Table 6.1. Comparison between the measured cross-sections and the SM predictions as a function of CMS energy is shown in Figure 6.1.

Apart from the statistical uncertainty provided by the MINUIT program, the common systematic uncertainty is also quoted in Table 6.1. A detailed description of the method used to estimate the systematic uncertainty is given in the next section.

6.2 Systematic uncertainty

6.2.1 Selection efficiency

Uncertainty of the selection efficiency is essentially uncertainty of the efficiencies $\epsilon_{i,j}^k$ (Eq. 6.2). The largest contribution is expected to arise from the modeling of detector response and the description of fragmentation processes.

An attempt has been made to account for both contributions with a single approach. This has been achieved by a two-by-two merging of Z^0 events collected at the CMS energy of 91 GeV at the beginning of each year's data taking. By merging two Z^0 decays the W^+W^- topology can be mimicked to a very good approximation.

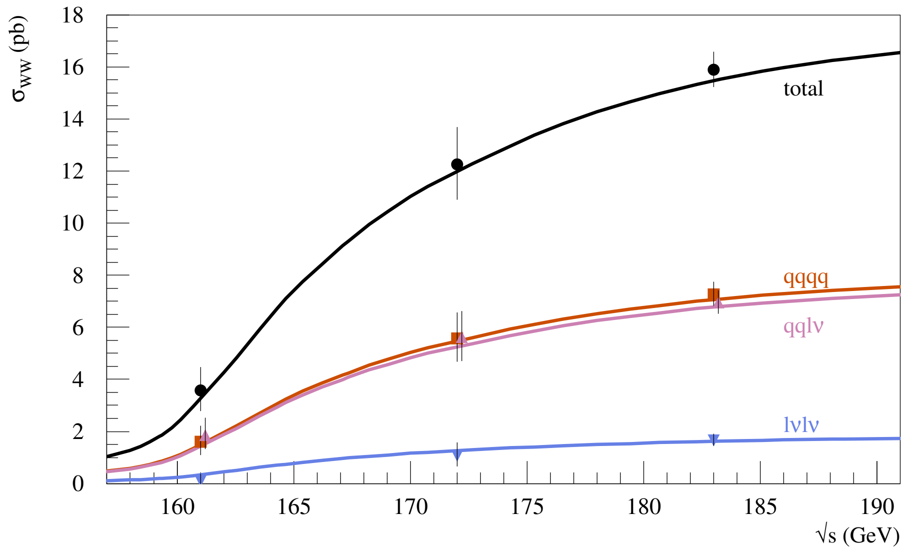

Figure 6.1: The measured partial W^+W^- cross-sections for three main decay channels and the total cross-section at the center of mass energies of 161, 172 and 183 GeV . The results are compared with the SM predictions using the event generator GENTLE [34]. The mixed and the hadronic channels are slightly displaced in energy in order to make comparison easier.

Quantity	161 GeV	172 GeV	183 GeV	combined
σ_{WW} (pb)	$3.57^{+0.91}_{-0.79} \pm 0.16$	$12.26^{+1.44}_{-1.35} \pm 0.34$	$15.89^{+0.69}_{-0.67} \pm 0.38$	
$Br_{W\to had}(\%)$	$70.2^{+7.1}_{-7.1} \pm 1.2$	$68.2^{+3.8}_{-4.0} \pm 0.9$	$67.6^{+1.5}_{-1.5} \pm 0.9$	$67.8^{+1.3}_{-1.3} \pm 0.8$
$\lvert V_{cs}\rvert$	$1.10^{+0.40}_{-0.37} \pm 0.06$	$1.01^{+0.19}_{-0.18} \pm 0.04$	$0.98^{+0.07}_{-0.07} \pm 0.04$	$0.99^{+0.06}_{-0.06} \pm 0.04$
$\sigma_{WW}^{Br=SM}$ (pb)	$3.63^{+0.90}_{-0.79} \pm 0.15$	$12.30^{+1.44}_{-1.35} \pm 0.34$	$15.89^{+0.69}_{-0.67} \pm 0.38$	
$\sigma_{WW\to qqqq}$ (pb)	$1.60^{+0.61}_{-0.51} \pm 0.12$	$5.58^{+0.98}_{-0.90} \pm 0.24$	$7.27^{+0.47}_{-0.46} \pm 0.29$	
$\sigma_{WW\to qql\nu}$ (pb)	$1.87^{+0.66}_{-0.55} \pm 0.09$	$5.62^{+1.00}_{-0.91} \pm 0.22$	$6.96^{+0.46}_{-0.44} \pm 0.22$	
$\sigma_{WW\to l\nu l\nu}$ (pb)	$0.10^{+0.27}_{-0.10} \pm 0.02$	$1.06^{+0.51}_{-0.40} \pm 0.09$	$1.66^{+0.25}_{-0.22} \pm 0.11$	

Table 6.1: Results of the maximum likelihood fit based on the distributions of the event probabilities. The first uncertainty quoted is statistical and the second systematic.

First we select and separate the hadronic Z^0 decays from the leptonic decays, where we further distinguish the $\tau\bar{\tau}$ decays from the electron or muon decays. In order to study efficiencies we shall retain practically all produced Z^0 events by the sorting criteria. For the hadronic channel we require more than five charged tracks and the total reconstructed energy larger than 30 GeV. Remaining events are considered as $Z \to e^+e^-$ or $\mu^+\mu^-$ candidates if there are two colinear jets ($\theta(j_1, j_2) > 160^0$) with exactly one charged particle of more than 20 GeV energy in each of two jets. Events not fulfilling the above criteria are candidates for the $\tau\bar{\tau}$ channel if the reconstructed energy is larger than 15 GeV. The number of charged tracks in each of two colinear jets should be 1 or 3. The lepton identification is not required by the sorting procedure. It could bias the selected events towards a better agreement between the simulation and real data. Some of the selected events are skipped in order to obtain the same angular distribution of jets as in the W^+W^- events. The decision is based on a random number generator. In the leptonic events, all particles belonging to one of jets are ignored to mimic the neutrino in the leptonic $W^\pm$ decays. Finally, two-by-two of the remaining Z^0 events are merged into one event. Track momenta and energies are multiplied by the factor m_W/m_Z in order to match particle momenta in decays of the $W^\pm$ bosons at rest. The rescaled four-momenta of particles are then boosted. Particles that belong to the same Z^0 boson are boosted in one direction and those belonging to the second Z^0 boson in the opposite direction. Energy and direction of the boost correspond to the four-momenta of $W^\pm$ bosons at a given CMS energy.

The described procedure is applied to both the simulated and real Z^0 events. The number of simulated merged Z^0 events is normalised to the number of merged events from the real sample. The merged events are then passed trough the same procedure as the high energy events. The distributions of quantities used to calculate the event probabilities are retained the same as for the high energy events. As a result we obtain the event probabilities $P_{qqqq}, P_{qq\nu e(\mu)}, \ldots$. The event probabilities obtained from the real merged events are compared to those obtained from the simulated merged events for each channel separately. The comparison is shown in Figure 6.2 together with the expected distribution of W^+W^- events. The agreement between the expected W^+W^- distributions and the distributions using the merged Z^0 events is good. A good level of agreement is found also for the individual separating variables. This confirms the prediction that the merged Z^0 events look similar to the W^+W^- events. The relative differences between the real and the simulated merged events in individual bins are used to estimate the systematic uncertainty. The efficiencies $\epsilon^k_{i,j}$ (Eq. 6.2) are multiplied by the relative differences and the likelihood fit was repeated with the selected high energy events as described in previous Section. As an estimate of the systematic uncertainty, the difference between the original and the re-fitted cross-section is used. Statistical uncertainties due to a finite number of merged events are taken into account as part of the systematic uncertainty from this

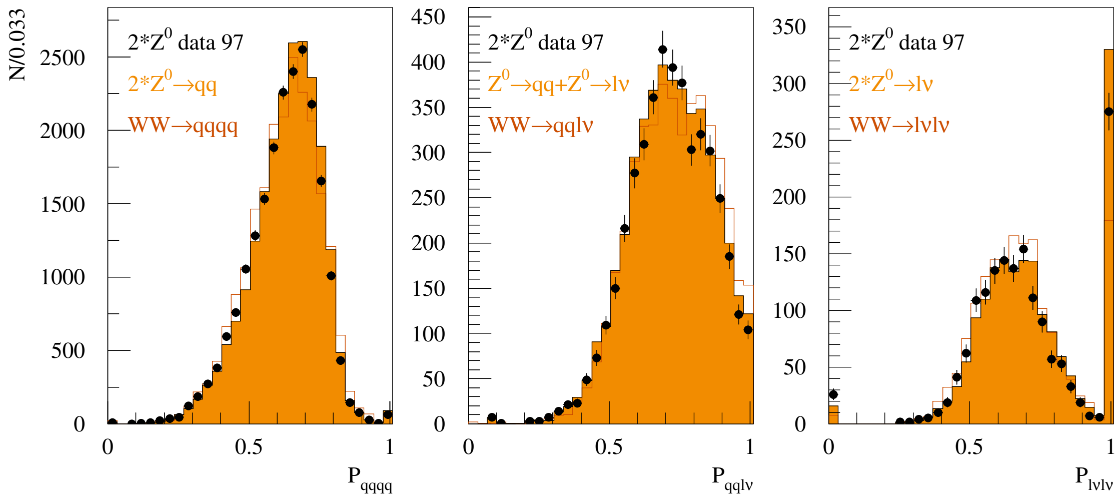

Figure 6.2: Comparison of the event probabilities between the simulated and the real merged Z^0 events collected in 1997. The line represents the expected distribution of W^+W^- events.

source. A common feature of all channels and the CMS energies is that the efficiencies obtained in the simulation of merged events are slightly overestimated with respect to the real merged events (Figure 6.2).

Simultaneously we estimated also the systematic uncertainty due to different center of mass energies used in the simulated and real samples (see Section 5.1). In the merged events, the difference between the CMS energies is reproduced by a different strength of the boost for the simulated and real merged events. The uncertainty due to different CMS energies is therefore included in the total systematic uncertainty estimated from the merged events.

The systematic uncertainties based on the presented method are listed in Tables 6.3, 6.4 and 6.5. Relative to the statistical uncertainty, the largest systematic uncertainty arises in the hadronic channel. A comparison of individual quantities in the merged events indicates that the difference is mainly due to a smaller number of tracks and reconstructed jets in the real merged events. The problem was mentioned already at the beginning of this Chapter (Figure 5.1). Visually, the disagreement between the real and the simulated merged events is the largest in the leptonic channel. The statistical uncertainty is also the largest in the leptonic channel, hence the relative importance of the systematic uncertainty is still the smallest in this channel.

We believe that the presented method incorporates the bulk of systematic effects due to the simulation of detector response and fragmentation of jets, apart from the interconnection phenomena. One of the main assumptions is that the detector performance has not changed significantly since the collection of Z^0 events at the beginning of each year. The stability of the detector was checked by looking at the time dependence of distributions of some general quantities during the high energy runs. No statistically significant effects were observed.

The interconnection phenomena (Section 2.2.2) have been searched for in several analyses performed by all LEP experiments ([39, 40, 46, 45]). Within the current precision the results are compatible with having no interconnection. According to a study performed by the ALEPH collaboration the uncertainty due to the interconnection should not exceed 0.04 pb in the hadronic channel if the current precision of the measurement is regarded. Therefore, we have neglected the interconnection as a possible source of the systematic uncertainty.

The mass of the $W^\pm$ boson is known to about 150 MeV. Though small, the uncertainty is included in the common systematic uncertainty. Its value is estimated by comparing the cross-sections obtained with several simulated samples generated with different $W^\pm$ masses.

6.2.2 Background normalisation

The main uncertainty related to the background is expected to arise from the normalisation of the background processes and from the simulation of the detector response.

Again, we attempted to include many effects in a single method. This was achieved by a direct comparison of the high energy real data and simulation. For every subchannel we selected a region in the event probability distribution where background dominates (Figure 6.3). It seems that the simulation slightly underestimates the levels of background for each of the three considered channels. The relative difference between the number of events in the selected region is assumed to represent the uncertainty of the background level in the whole probability region. The estimated systematic uncertainty is the difference between the original and the re-fitted cross-section where the rescaled background level is used.

Regardless of the channel, the upper bound of the selected region starts at the event probability of 0.5. The lower bound is selected such that the relative statistical uncertainty of the number of expected events in the selected window falls below 5%. In order to ensure enough events the preselection cuts are relaxed. The level of the relaxed cuts and the 5% limit are a compromise between the reliability of comparison and the statistical uncertainty that is influencing the estimate of the systematic uncertainty. Since we are concerned about the high probability region, the selected window should be close to this region. On the other hand, we are limited by the number of background events that

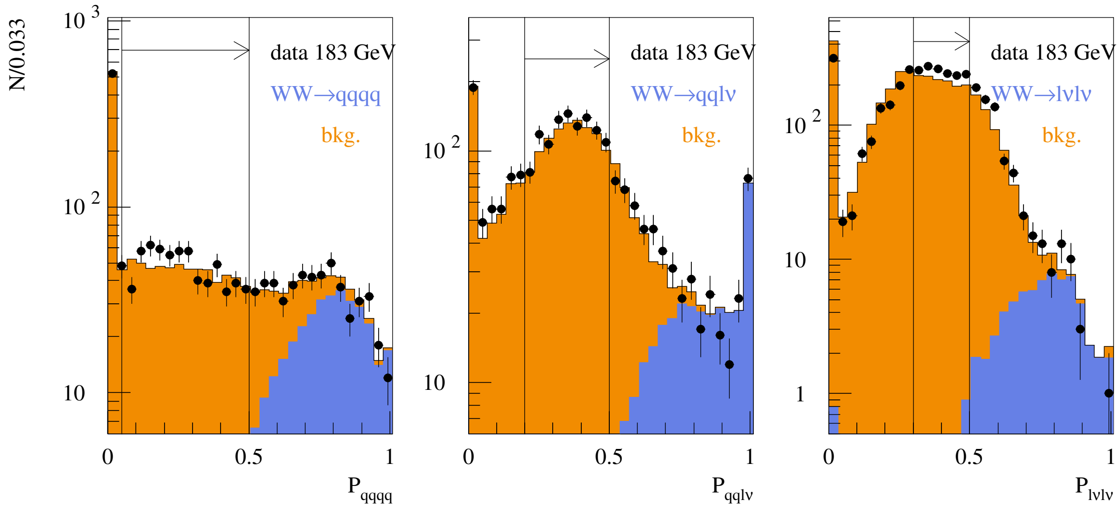

Figure 6.3: Comparison of the event probabilities between data and simulation with the relaxed preselection cuts at 183 GeV. The difference between the number of events in the regions marked by arrows is used to estimate the uncertainty of the background level.

can be increased only by loosing cuts. We found that more the cuts are relaxed the larger is the disagreement. In this respect the estimated uncertainty is rather a conservative one.

The results are summarised in Tables 6.3, 6.4 and 6.5 . The uncertainty due to the background normalisation is smaller than the one due to the selection efficiency. This is true in particular for the 183 GeV sample. Though, the relative difference in the background level is the smallest in the hadronic channel ($\sim$ 5%) it leads to the largest relative uncertainty because of the lowest purity in this channel. On the other hand, the relative difference of about 20% is nearly negligible for the measured cross-section in the leptonic channel.

As a separate test of the modeling of hard gluon radiation we compared real and simulated hadronic Z^0 decays with more than two jets. Large samples are needed to obtain enough multi-jet decays, therefore, we relied on events collected during the LEP1 period. Momenta of tracks from the Z^0 decays are first up-scaled to match those at the LEP2 CMS energies. Events are then passed through the same preselection and selection criteria as the high energy events. The observed relative differences in the distributions of event probabilities are used to estimate the systematic uncertainty due to the modeling of QCD events as the most severe background in the hadronic and mixed channel (Figure 6.4). Since the differences are small, we feel safe to conclude that the modeling of hard-gluon radiation is adequate. The obtained systematic uncertainty was added independently to

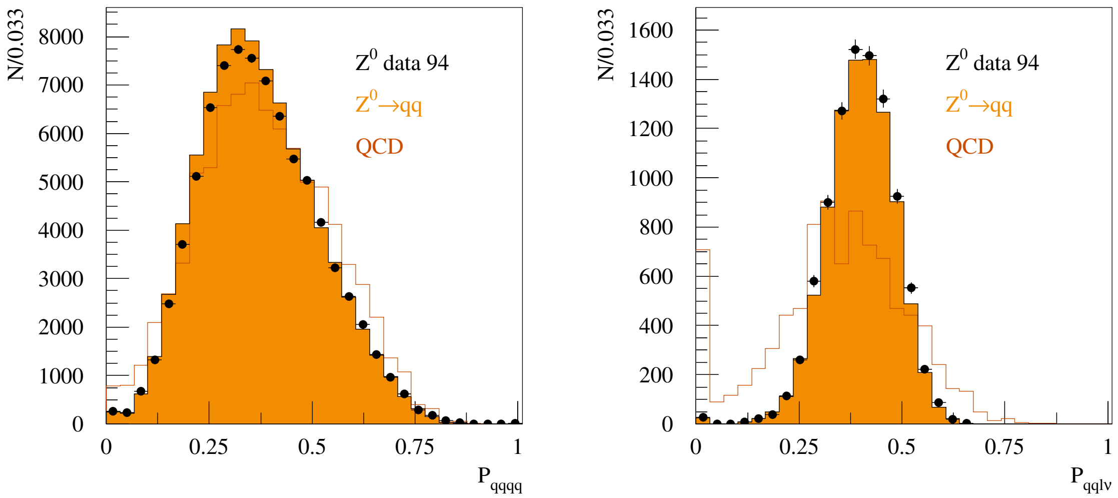

Figure 6.4: Comparison of the event probabilities between real and simulated multi-jet hadronic Z^0 decays collected in 1994. Track momenta are rescaled to correspond to momenta at 183 GeV. The expected distribution of QCD events is presented with the line.

the overall uncertainty despite the fact that it is implicitly taken into account already by the previous method.

6.2.3 Corrections to CCO3 diagrams

Interference terms between four-fermion diagrams are in general not taken into account in the used simulated samples (see Section 2.2.2). There are also other non-resonant diagrams that do not belong to any of explicit channels considered in the simulated samples (Section 2.4). To account for these additional diagrams and interference terms between all four-fermion diagrams we introduced correction factors f_i^{CCO3} (Eq. 6.2). The role of the correction factors is to relate the measured W^+W^- cross-section $\sigma^{meas.}_{WW\to i}$ to the contribution $\sigma_{WW\to i}$ which corresponds to the CCO3 diagrams only (Figure 2.1):

$$\sigma_{WW\to i} = f_i^{CCO3} \cdot \sigma^{meas.}_{WW\to i}. \tag{6.4}$$

Values of the factors are obtained by using the EXCALIBUR four-fermion event generator [35]. This generator incorporates all possible diagrams at the tree level and interferences among them. EXCALIBUR also offers possibility to generate each of the processes separately. This option is used to replace the PYTHIA four-fermion samples to be sensitive only to differences due to the interferences and missing diagrams. The four-fermion sample replaces the real data in the likelihood fit. The correction factor is

Channel	161 GeV	172 GeV	183 GeV
$qqqq$	1.012 ± 0.013	0.980 ± 0.013	1.000 ± 0.010
$qq\nu e$	1.090 ± 0.012	1.019 ± 0.011	1.000 ± 0.020
$qq\nu\mu(\tau)$	1.006 ± 0.016	0.996 ± 0.013	1.000 ± 0.010
$l\nu l\nu$	1.088 ± 0.017	0.980 ± 0.018	1.000 ± 0.010

Table 6.2: Values of the correction factors f^{CCO3} for different decay channels and CMS energies. The values are taken from [35, 76].

the ratio between the fitted cross-section and the one generated with the CC03 diagrams, only (Eq. 6.4). The obtained correction factors are displayed in Table 6.2. The systematic uncertainty of the correction factors is dominated by the statistical uncertainty due to the limited simulated samples. The largest correction factors have been found for the 161 GeV sample where they can extend up to 9% for the mixed channel with an electron produced (Table 6.2). At 183 GeV the factors are already compatible with the unity within the estimated uncertainty. The energy dependence is mainly due to the fact that the CCO3 cross-section increases with increasing CMS energy while the cross-section for many other four-fermion diagrams remains approximately constant or it even decreases with the increasing energy. For this reason, the relative importance of non CCO3 diagrams becomes smaller. The correction factors vary from one decay channel to another. The largest correction is implemented in the mixed channel with an electron produced. In this channel, there is a large interference of the CC03 diagrams with the $W^+e^-\bar{\nu}_e$ diagram and other t-channel diagrams with the same final state. None of the t-channel diagrams can lead to μ or τ in the final state. Therefore, the correction factors are negligible for channels with produced μ or τ.

6.2.4 Other sources

Uncertainty of the measured luminosity was discussed already in Section 5.1. The systematic uncertainty of the cross-section is obtained by varying $\mathcal{L}$ in Eq. 6.2 within the estimated overall uncertainty. Compared to other sources, the contribution appears to be almost negligible (Table 6.3, 6.4, and 6.5). Moreover, the luminosity does not influence the measured value of $Br_{W\rightarrow had}$ and $|V_{cs}|$ as they do not depend on the absolute normalisation.

The statistical uncertainty due to the finite simulated samples is of bigger importance. The contribution to the systematic uncertainty is obtained by simultaneously varying all $\epsilon^k_{i,j}$ and $\sigma^k_j(bkg)$ (see Eq. 6.2) according to the multinomial distribution of statistical fluctuations. The values of changed efficiencies are provided by a random-number

source	at 161 GeV (pb)	at 172 GeV (pb)	at 183 GeV (pb)
selection efficiency	$0.03 \otimes 0.02$	$0.06 \otimes 0.06$	$0.22 \otimes 0.05$
background level	(10%) 0.11	(7%) 0.20	(5%) 0.14
MC statistics	< 0.01	0.03	0.07
f_{qqqq}^{CC03}	(1.3%) 0.02	(1.3%) 0.07	(1.0%) 0.07
QCD bkg.	< 0.01	0.02	0.02
luminosity	(0.5%) 0.01	(0.5%) 0.03	(0.3%) 0.02
W mass ($\pm$150 MeV)	< 0.01	0.02	0.02
total	0.12	0.24	0.29

Table 6.3: Systematic uncertainties of the measured cross-section in the hadronic channel. To estimate the uncertainties the corresponding parameters were varied by the numbers given in brackets. The first uncertainty of the selection efficiency is estimated by using the merged Z^0 events while the second value represents the statistical error of the estimate.

generator. In this way, several simulated samples are obtained. Each sample leads to a different fitted cross-section. The variance of the fitted cross-sections serves as the systematic uncertainty.

6.2.5 Combination of systematic uncertainties

So far we have discussed the systematic uncertainties arising from the individual sources, decay channels, and CMS energies. They are expressed as the uncertainties of the partial cross-sections. For a proper propagation and combination of the uncertainties possible correlation among different contributions have to be considered. The following contributions are assumed to be fully correlated: the mass of the $W^{\pm}$ boson, the luminosity at the same CMS energy, and other contributions at different CMS energies if they belong to the same source and the same channel. Other combinations are treated as fully uncorrelated.

In order to obtain the systematic uncertainty of $Br_{W\to had}$ and $|V_{cs}|$ we varied all parameters in Eq. 6.2 within the quoted systematic uncertainties (Table 6.3, 6.4, and 6.5). The parameters belonging to an individual source and channel are varied separately as uncorrelated at a given CMS energy. The only exception is the mass of the $W^{\pm}$ boson that was coherently changed in all channels. The common systematic uncertainty of $Br_{W\to had}$ and $|V_{cs}|$ is evaluated by summing up in quadrature all changes in values due to each variation performed (i.e. uncorrelated). Since $Br_{W\to had}$ and $|V_{cs}|$ do not depend on the absolute normalisation, the uncertainty of the luminosity is not considered.

The uncertainties of values combined from all three CMS energies were obtained by coherently varying the common sources within the same channel. At the end, the

source	at 161 GeV (pb)	at 172 GeV (pb)	at 183 GeV (pb)
selection efficiency	$0.04 \otimes 0.05$	$0.13 \otimes 0.10$	$0.14 \otimes 0.09$
background level	(10%, 17%) 0.05	(12%, 16%) 0.11	(5%, 8%) 0.06
MC statistics	< 0.01	0.03	0.07
$f^{CC03}_{qql\nu}$	(1.6%) 0.03	(1.3%) 0.07	(1.3%) 0.09
QCD bkg.	0.01	0.03	0.03
luminosity	(0.5%) 0.01	(0.5%) 0.03	(0.3%) 0.02
W mass (±150 MeV)	< 0.01	0.01	0.01
total	0.09	0.22	0.22

Table 6.4: Systematic uncertainties of the measured cross-section in the mixed channel. To estimate the uncertainties the corresponding parameters were varied by the numbers given in brackets. The first and the second number for the background level relate to the e, μ and the τ channel respectively. The first uncertainty of the selection efficiency is estimated by using the merged Z^0 events while the second value represents the statistical error of the estimate.

source	at 161 GeV (pb)	at 172 GeV (pb)	at 183 GeV (pb)
selection efficiency	$0.01 \otimes 0.01$	$0.04 \otimes 0.02$	$0.08 \otimes 0.02$
background level	(10, 20, 35%) < 0.01	(15, 30, 20%) 0.05	(6, 35, 20%) 0.02
MC statistics	< 0.01	0.02	0.04
$f^{CC03}_{l\nu l\nu}$	(1.7%) < 0.01	(1.8%) 0.02	(1.0%) 0.02
luminosity	(0.5%) < 0.01	(0.5%) < 0.01	(0.3%) < 0.01
W mass (±150 MeV)	< 0.01	0.01	0.01
total	0.02	0.09	0.11

Table 6.5: Systematic uncertainties of the measured cross-section in the leptonic channel. To estimate the uncertainties the corresponding parameters were varied by the numbers given in brackets. The three numbers for the background level relate to the sub-channels: muon, two track and the rest. The first uncertainty of the selection efficiency is estimated by using the merged Z^0 events while the second value represents the statistical uncertainty of the estimate.

contributions from the individual sources and channels are summed up in quadrature.

The uncertainty of the total cross-section is calculated in a similar manner as for $Br_{W\to had}$ at a single CMS energy. Here however, the uncertainty of the luminosity is included as fully correlated among all channels.

The assumption about uncorrelated contributions from the same source and different decay channels does not appear to be justified at least as far as the selection efficiency and the background normalisation are concerned. As discussed in Sections 6.2.1 and 6.2.2 the selection efficiency seems to be overestimated while the background level tends to be underestimated for all decay channels. With respect to these observations the uncorrelated combination of uncertainties of $Br_{W\to had}$ and $|V_{cs}|$ is rather a conservative one. As an illustration let us consider the case where the selection efficiency is overestimated in all channels by the same factor. In this case the value of the hadronic branching ratio would not change. In the first approximation, the same is true if the background levels were consistently underestimated in all channels. The uncertainty of the selection efficiency and the background normalisation are assumed to be uncorrelated with each other. Under this assumption we may have also overestimated the systematic uncertainty, since the observed deviations in the selection efficiency and the background normalisation tend to cancel each other.

The estimated systematic uncertainties of σ_{WW}, $Br_{W\to had}$ and $|V_{cs}|$ are presented in Table 6.1. For the collected number of events the statistical uncertainty is still the dominant one for all quantities of interest. Therefore, a more detailed consideration of correlations that would result in a lower systematic uncertainty is of little importance for the overall precision.

7

Flavour tagging of $W^\pm \to cs$ di-jets

As discussed in Section 2.3 the most direct information on the $|V_{cs}|$ element in the LEP2 environment can be obtained by measuring the fraction of cs di-jets in the hadronic decays of the $W^\pm$ bosons. Apart from the cs di-jets ($cs = c\bar{s}$ or $\bar{c}s$) that are expected to be produced in about 45% of the hadronic $W^\pm$ decays, there is approximately equal fraction of ud di-jets. The rest of hadronic decays is shared between us and cd di-jets, while decays into ub or cb di-jets occur at the permil level. This simplifies to some extend a tagging of jet flavour as we need to distinguish only between the jets arising from u, d, c, and s quarks. Once this is achieved, we are able to separate also between different flavour combinations of di-jets from the $W^\pm$ bosons. We can further improve the identification of di-jets by combining some kinematic properties of the W^+W^- events. They enable separation between quarks and anti-quarks of the same flavour as well as up-like quarks and down-like quarks. This reduces the number of possible flavour combinations of di-jets.

7.1 Selection of hadronic $W^\pm$ decays

The hadronic $W^\pm$ decays are common to the hadronic and the mixed channel. The probabilistic approach used to select the W^+W^- events in these two channels was discussed in Chapter 5. For purposes of the flavour tagging we accepted only events with the event probabilities P_{qqqq} and $P_{ql\nu}$ larger than the value where the product of efficiency and purity of the selected sample reaches its maximum (see Figures 5.6 and 5.13). In the further analysis all accepted events are considered with equal weights regardless of the event probability. In total, 480 events are selected in the hadronic channel. Among them 117 are expected to be background events. According to the SM we would expect 353 signal events. In the mixed channel 352 events are selected with 350 expected of which 37 from background.

7.2 Flavour tagging of jets

7.2.1 Charge of $W^{\pm}$ boson

In the mixed channel charge of the $W^{\pm}$ boson can be efficiently determined by looking at charge of the lepton arising from the accompanying $W^{\pm}$ boson. In this way, the charge of the $W^{\pm}$ bosons is determined correctly in more than 95% of the mixed W^+W^- decays.

In the hadronic channel we can look at the detected charge difference between tracks arising from different $W^{\pm}$ bosons. Faster charged particles carry more information about the charge of the parent $W^{\pm}$ boson. Therefore, we weight particle charges with respect to their momenta. The corresponding weighted charge difference $\Delta Q(W_1)$ is defined as: $\Delta Q(W_1) = \sum_{i=1...N_{tk}(W_1)} q_i \cdot \sqrt{p_i} - \sum_{i=1...N_{tk}(W_2)} q_i \cdot \sqrt{p_i}$. A positive value of $\Delta Q(W_1)$ indicates a positive charge of W_1. Quality of the separation based on the charge difference is shown in Figure 7.1.

A more efficient separation of the $W^{\pm}$ charge in the hadronic channel is obtained by using direction of the outgoing $W^{\pm}$ bosons. As discussed in Section 2.2.1, the W^+ bosons mainly fly in the direction of the incoming positron. The separation based on the angular distribution is more pronounced at higher CMS energies. At 161 GeV the charge difference is of approximately equal importance as the angular distribution, while at 183 GeV the angular distribution already provides a much better charge separation (Figure 7.1).

Based on the expected distribution of the charge difference and the angular distribution we calculate the combined probability P^{W^+} that a W boson posses a positive charge. In the mixed channel only the charge of the accompanying lepton contributes to the probability P^{W^+}.

7.2.2 Separation between up-like and down-like quarks

The V-A form of weak interaction allows us to distinguish between the up-like quarks and the down-like quarks emerging from the $W^{\pm}$ decays (see Section 2.2.1). Because of a partial polarisation of the $W^{\pm}$ bosons, the up-like quarks tend to fly at larger angles with respect to the direction of the parent $W^{\pm}$ boson in its rest frame (Figure 7.2). Based on the presented angular distribution we calculate the probability P^{up} that a jet arises from an up-like quark. Again, the separation is more pronounced at higher CMS energies, although, it is relatively weak even at 183 GeV .

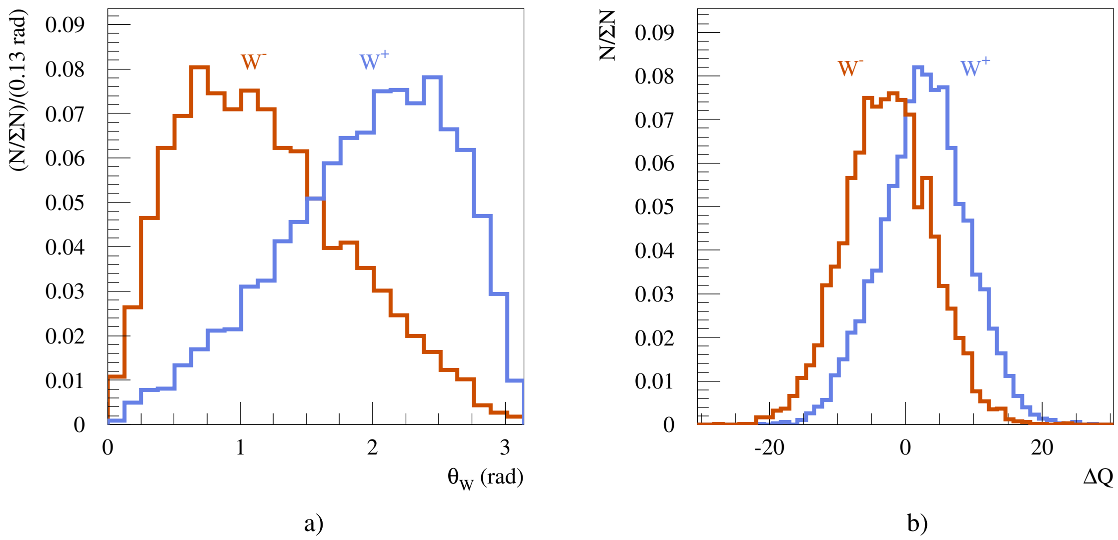

Figure 7.1: a) The expected distribution of polar angles of W^+ and W^- bosons at 183 GeV. **b)** The expected momentum weighted charge difference for the W^+ and W^- bosons at 183 GeV.

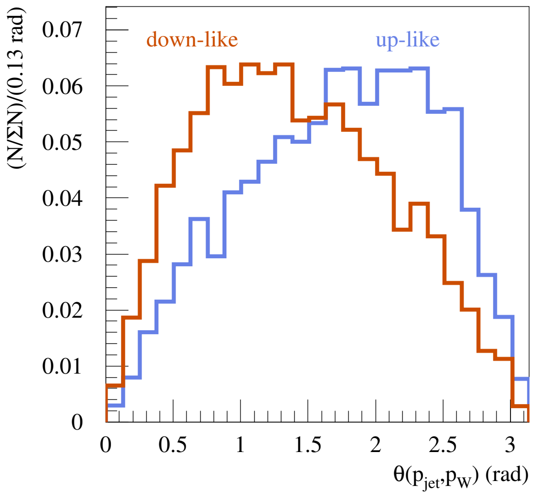

Figure 7.2: The expected distribution of the angle between a jet and the parent $W^{\pm}$ boson in its rest frame for the up-like and the down-like quarks at 183 GeV.

7.2.3 Lifetime tag

Hadrons composed of c quarks have a typical decay length of about 2 mm at the LEP CMS energies. On the other hand, hadrons containing only u, d or s quarks fly at least few centimeters. Particles arising from decays of c-hadrons therefore have small but finite and positive impact parameters with respect to the primary vertex (see Section 4.6). As a selection parameter the significance of the impact parameter is chosen. It is defined as the impact parameter divided by its measurement error.

Apart from the impact parameters, jets arising from c quarks can be characterised by some additional properties. Because of a relatively large mass of the c quark ($m_c \sim 1.3$ GeV), c-hadrons are in general heavier than those composed of the light flavour quarks (u, d, s). Decay products of c-hadrons will therefore have larger momenta in the rest frame of hadrons. In the process of fragmentation c quarks retain a larger fraction of the initial momentum as the light quarks do. Again, this is a consequence of a larger mass of the c quark. Therefore, decay products of c-hadrons are more boosted along the jet direction leading to larger momenta in the laboratory frame. Despite large momenta, the angle between a track and the jet is still relatively large because of a large transverse momentum with respect to the jet axis.

The significance of impact parameter, the angle between the track and the jet axis, and momentum of the track, are used to construct the probability P_i^c that the track arises from a c-hadron. [2] The expected distributions used to calculate P_i^c are provided as a function of all three quantities simultaneously in order to account for correlation among them (see Section 4.10). Large samples are needed to obtain three parametric distributions for c jets and light flavour jets. For this reason, the simulated hadronic Z^0 decays are used.

The probability $P^{c\prime}$ that a jet arises from a c quark is obtained by multiplying the single track probabilities P_i^c:

$$P^{c\prime} = \frac{\prod_i P_i^c}{\prod_i P_i^c + \prod_i (1 - P_i^c)}.$$

The $P^{c\prime}$ distribution for different jet flavours is shown in Figure 7.3 a). In Figure 7.3 b) the expected efficiency and purity of the selection of c quarks is presented. Note that $P^{c\prime}$ does not posses properties of a true probability mainly because of the multiplication of the single track probabilities that are correlated within a single jet. The true probability P^c is calculated from the expected distribution of $P^{c\prime}$ (see Section 4.10).

[2]The method is just a slight modification of the method described in [63]. It will be referred as 'lifetime tag' because the significance of impact parameters is the crucial separating variable.

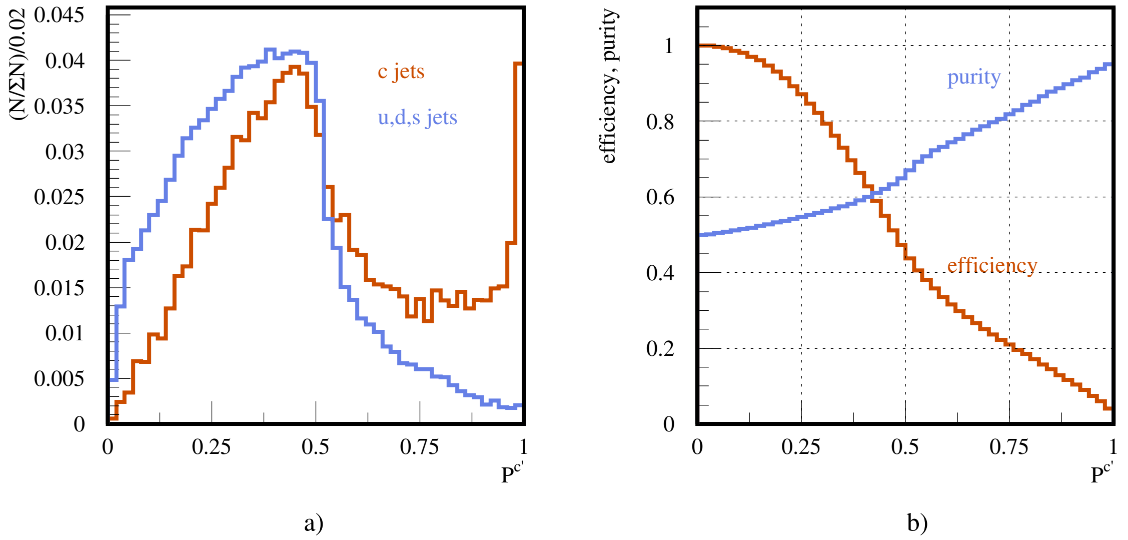

Figure 7.3: **a)** Distribution of $P^{c\prime}$ for c jets and light flavour jets in the W^+W^- decays. **b)** The efficiency and purity of the selected c jets as a function of cut on $P^{c\prime}$ whereby an equal initial number of c jets and light flavour jets is assumed.

7.2.4 Particle identification

Identities and momenta of particles produced in the process of fragmentation depend on flavour of the primary quark. In the process of fragmentation the primary quark most probably acquires a u or a d quark from the vacuum to form a hadron. As this hadron contains the primary quark, it will be among the fastest particles in the jet.

If the primary quark is an s quark, the corresponding meson is a kaon. About half of produced kaons are charged particles $K^+(u\bar{s})$ or $K^-(\bar{u}s)$. The rest are neutral kaons K^0_S or K^0_L. K^0_L is a stable particle within the detector dimension while K^0_S decays after about 8 cm into two pions. One could identify K^0_S via two reconstructed charged tracks with a common displaced vertex and an invariant mass compatible with that of K^0_S. However, the efficiency of K^0_S selection has been found low ($\sim 15\%$), therefore, the identification of K^0_S is not used in the analysis. Barions composed of s quarks are produced in about 10% of s-jets. They are not directly searched for in the analysis.

The fragmentation of c quarks is also likely to yield a kaon because of a weak $c \to s$ transition. This transition proceeds via exchange of a virtual $W^{\pm}$ boson. Since the s quark is a decay product, the kaons are expected to be slower than those emerging from the primary s quarks. In about 19% of cases the virtual $W^{\pm}$ boson decays leptonicaly into an electron or a muon. Thanks to a high efficiency and purity, the muon identification (Section 4.7.1) is used as a supplementary indication for c jets. The electron identification is less efficient and is not implemented.

After the fragmentation, a primary u or d quark will mostly end up within a fast pion. The probability that an s quark is acquired from the vacuum is six times smaller.

To identify $K^{\pm}$ and $\pi^{\pm}$ we use information from the barrel RICH counters by combining the HADSIGN and RIBMEAN algorithms as described in Section 4.7.4. For the flavour tagging of jets at most one of identified particles is exploited. The fastest of identified kaons is selected if it is among three fastest particles in the jet. If not, the particle identified as a muon is considered. In case there are no muons identified, the fastest of identified pions among the three leading particles in the jet is selected. Slower particles are not considered as they are not likely to contain the primary quark. In about 35% of jets none of reconstructed particles meets the above criteria. In such cases the identification does not contribute to the flavour tagging.

Based on properties of the selected particle we calculate the probabilities P^f_{id} that a jet arises from the primary quark f, where $f = u, \bar{u}, d, \bar{d}, c, \bar{c}$, s, or $\bar{s}$. Separation between quarks and anti-quarks of the same flavour is achieved by exploiting charge of the selected particle. The simulated density-distributions used to calculate probabilities P^f_{id} are provided as a function of momenta of the selected particles for each of the possible discrete cases: $1K^+$ (the leading K^+), $1K^-$ (the leading K^-), $2K^-$ (the second leading K^-),..., $1\pi^-$, ..., μ^-. A few of these distributions are shown in Figure 7.4. By comparing the distributions to each other one can observe many features that can be easily understood on a qualitative basis. The distributions are normalised such that the sum over all momenta and discrete cases equals one for a given jet flavour. The case with no particle selected is also accounted in the normalisation.

7.3 Tagging of cs di-jets

The jet probabilities P^{W^+}, P^{up}, P^c, and P^f_{id} are combined into the probability P_{cs} that a di-jet consists of a c and an s jet. The most severe background is expected from the ud di-jets that are considered as the only alternative to the cs di-jets when the probability is calculated. Hence, we are left with the following possible combinations:

$$c\bar{s},\ \bar{c}s,\ \bar{s}c,\ s\bar{c},\ u\bar{d},\ \bar{u}d,\ \bar{d}u,\ d\bar{u}, \tag{7.1}$$

where the first written quark denotes the jet no.1 and the second quark the jet no.2 from the same $W^{\pm}$. Probabilities for the considered di-jet combinations (Eq. 7.1) are

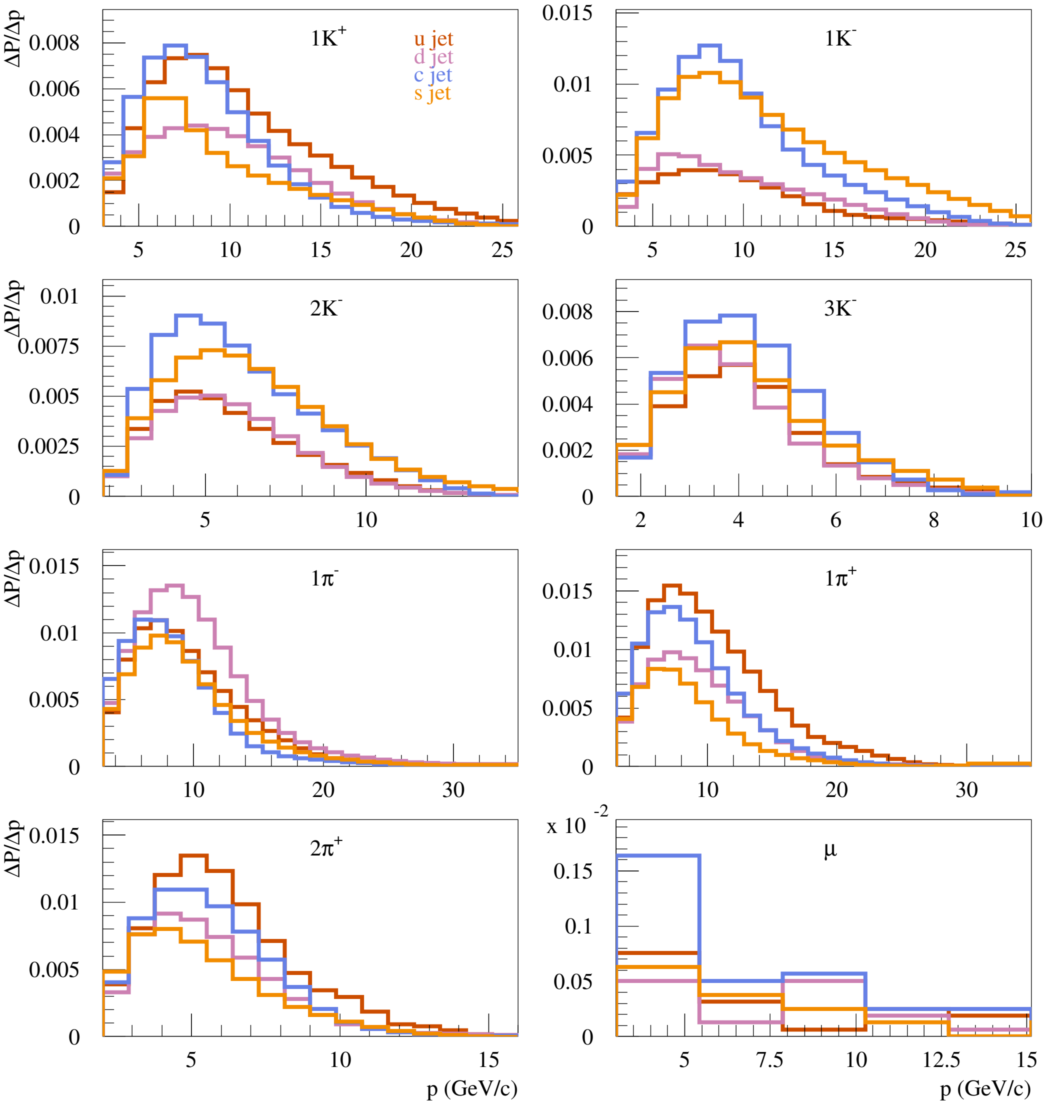

Figure 7.4: Momentum distributions of identified particles arising from different jet flavours. The distributions are shown for the first, the second, and the third fastest kaon as well as for the leading and the second fastest pion and identified muon. Distributions of anti-quarks are equivalent to the above distributions with inverted particle charges. One observes that: the separating power degrades from $1K^-$ to $3K^-$, $1K^-$ enables better separation of c and s jets than $1K^+$, the separation based on $\pi^{\pm}$ is worse from the one based on $K^{\pm}$, $1\pi^+$ enables the best separation between u and s jets, the separation based on muons is weak, ...

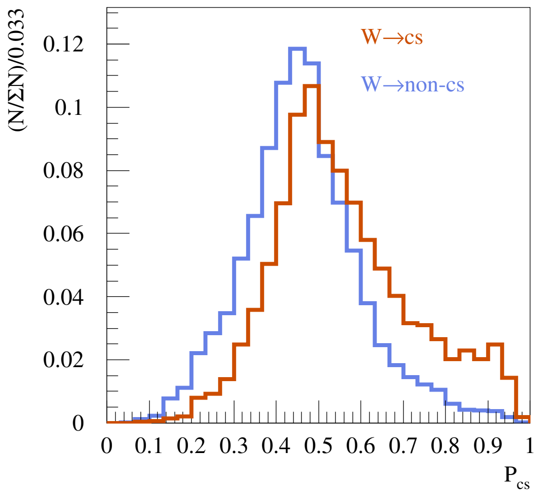

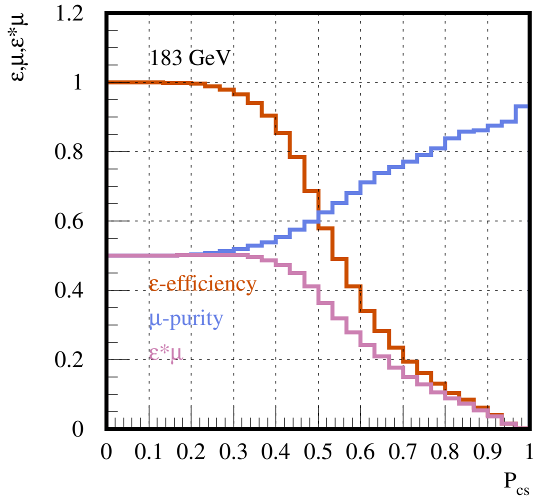

Figure 7.5: a) The normalised distribution of P_{cs} for the cs and non-cs di-jets from the hadronic $W^{\pm}$ decays. **b)** The efficiency, purity, and the product of the two for the selected cs di-jets as a function of cut on P_{cs}. An equal number of cs and non cs di-jets is assumed.

calculated in the following way:

$$\begin{aligned}
P_{c\bar{s}} &= P^{W^+} \cdot P^{up}(1) \cdot P^{c}(1) \cdot (1 - P^{c}(2)) \cdot P^{c}_{id}(1) \cdot P^{\bar{s}}_{id}(2), \\
P_{\bar{c}s} &= (1 - P^{W^+}) \cdot P^{up}(1) \cdot P^{c}(1) \cdot (1 - P^{c}(2)) \cdot P^{\bar{c}}_{id}(1) \cdot P^{s}_{id}(2), \\
P_{\bar{d}u} &= P^{W^+} \cdot (1 - P^{up}(1)) \cdot (1 - P^{c}(1)) \cdot (1 - P^{c}(2)) \cdot P^{\bar{d}}_{id}(1) \cdot P^{u}_{id}(2),
\end{aligned} \tag{7.2}$$

and equivalently for other combinations. The indices (1) and (2) relate to the jet no.1 and the jet no.2, respectively. As such, the probability for a given flavour combination is a product of single jet probabilities based on different information. The probability P^{up} is used once per a di-jet because the angles of two jets are fully correlated. As opposed to the separating variables used in the selection of W^+W^- events, the quantities used in the flavour tagging are expected to be only weakly correlated. There is some correlation between the charge difference and the charge of identified particle. A weak correlation is expected between the momentum of identified particle and the momenta used in the lifetime tag. Some correlation between two jets is also possible due to a correlated performance of jet reconstruction within an event. However, to a very good approximation, the variables are uncorrelated, therefore, the multiplication of probabilities is close to an optimal combination of the single probabilities.

For the measurement of $|V_{cs}|$ we do not need to distinguish between quarks and anti-quarks, nor we are interested whether the first or the second jet is an s or a c jet. It is sufficient to know the probability P_{cs} that a given di-jet combination emerges from an

$s(\bar{s})$ and a $c(\bar{c})$ quark. The probability P_{cs} is evaluated from the specified probabilities (Eq. 7.2) by summing up all contributions containing $s(\bar{s})$ and $c(\bar{c})$ jets:

$$P_{cs} = \frac{P_{c\bar{s}} + P_{\bar{c}s} + P_{s\bar{c}} + P_{\bar{s}c}}{P_{c\bar{s}} + P_{\bar{c}s} + P_{s\bar{c}} + P_{\bar{s}c} + P_{u\bar{d}} + P_{\bar{u}d} + P_{d\bar{u}} + P_{\bar{d}u}}, \tag{7.3}$$

where the denominator normalises the probability P_{cs} under the assumption that ud and cs di-jets form a complete set. The expected P_{cs} distribution for the cs di-jets and non-cs di-jets from the hadronic $W^{\pm}$ decays is shown in Figure 7.5. The efficiency and purity as a function of cut on P_{cs} is also presented.

8

Interpretation of tagged cs di-jets: r_{cs}, $|V_{cs}|$

8.1 Likelihood fit

The fraction of cs di-jets in the hadronic $W^{\pm}$ decays (r^{cs}) and consequently the value of $|V_{cs}|$ (see Section 2.3) are obtained by the likelihood fit of the expected P_{cs} distribution to the measured distribution (Figure 8.1). The number of expected di-jets $\bar{N}_{i,j}$ in the i-th bin and j-th channel (j=$qqqq$, $qql\nu$) is written as a function of r_{cs} as follows:

$$\bar{N}_{i,j}(r_{cs}) = \mathcal{L} \cdot N_{had} \cdot (\sigma_{i,j}^{bkg} + \sum_{N_{cs}=0,1,2} (\sigma'_{WW\to j} \cdot \epsilon_{i,j\to j}^{N_{cs}} \cdot f_j^{N_{cs}} + \sigma'_{WW\to j'} \cdot \epsilon_{i,j'\to j}^{N_{cs}} \cdot f_{j'}^{N_{cs}})), \tag{8.1}$$

where

$$\begin{aligned} &f_{qqqq}^0 = (1-r_{cs})^2,\ f_{qqqq}^1 = 2\cdot r_{cs}\cdot(1-r_{cs}),\ f_{qqqq}^2 = r_{cs}^2, \\ &f_{qql\nu}^0 = 1-r_{cs},\ f_{qql\nu}^1 = r_{cs},\ f_{qql\nu}^2 = 0. \end{aligned} \tag{8.2}$$

Here, $\mathcal{L}$ is the integrated luminosity and N_{had} is the number of hadronic $W^{\pm}$ decays per event. $\sigma_{i,j}^{bkg}$ is the accepted background cross-section in the given bin and channel. $\epsilon_{i,j\to j'}^{N_{cs}}$ is the probability that a di-jet produced in the j-th channel in an event with N_{cs} cs di-jets is picked up in the i-th bin of the j'-th channel. The factor $f_j^{N_{cs}}(r_{cs})$ is the expected fraction of events with the N_{cs} cs di-jets produced in the j-th channel. The second term accounts for migrations from the j'-th channel into the channel j. This term is practically negligible since the probability for migrations is only at the percent level. $\sigma'_{WW\to j}$ are the normalisation factors that rule out any dependence of r_{cs} on the total number of reconstructed events in each channel separately. They are determined simultaneously for a given value of r_{cs} in such a way that the total number of expected di-jets in each channel equals the measured number of di-jets. In practice, the dependence of $\sigma'_{WW\to j}$ on the value of r_{cs} is negligible. It would appear if the event selection efficiency would depend on the jet flavours.

Since the total number of expected events is normalised to the measured number, the multinomial distribution [30] is assumed for the number of reconstructed di-jets in bins of the P_{cs} distribution. The probability P_j for the j-th channel where $N_{i,j}$ di-jets are measured and $\bar{N}_{i,j}(r_{cs})$ expected is given by:

$$P_j = \frac{N_j!}{N_{1,j}! \cdot N_{2,j}!, \ldots} p_{1,j}^{N_{1,j}} \cdot p_{2,j}^{N_{2,j}} \ldots,$$

with $p_{i,j} = \bar{N}_{i,j} / \sum_i \bar{N}_{i,j}$. The combined probability P for both channels is obtained by multiplying single-channel probabilities:

$$P = P_{qqqq} \cdot P_{ql\nu}.$$

The probability for all CMS energies together is derived by multiplying the probabilities P for single energies.

Comparison between the expected and the measured P_{cs} distributions is shown in Figure 8.1 for 183, 172 and 161 GeV samples. The value of r_{cs} is obtained by maximising the probability P using the MINUIT program ([29]). If r_{cs} is expressed by $|V_{cs}|$ (Eq. 2.20) and the measured values of other CKM elements are used the value of $|V_{cs}|$ is obtained. The fitted values r_{cs}^{fit} and $|V_{cs}^{fit}|$ are presented in Table 8.1.

8.2 Corrections of fitted values

The fitted value of $|V_{cs}|$ (or r_{cs}) is very sensitive to the simulation of quantities related to the particle identification and the lifetime tag. In Section 4.6 and 4.7.4 we presented the methods for a fine tuning of the relevant parameters in order to obtain a realistic simulation. However, some discrepancies can still remain; in particular those arising from the modeling of fragmentation processes which is not accounted for in the fine tuning.

We developed a method that provides the distributions needed to calculate the jet probabilities from real data itself. By comparing these distributions with the equivalent simulated distributions we can estimate the a shift of the fitted value of $|V_{cs}|$ due to eventual discrepancies in the simulation. The fitted values are then corrected according to the estimated shift.

In order to estimate differences between the simulation and real data a large number of events is needed and the analysed processes should be well known. We used the hadronic Z^0 decays collected at the beginning of each year's data taking. The method is based on assumption that comparison of jets from the Z^0 decays provides reliable estimates for jets arising from the $W^{\pm}$ decays as far as relative differences between the simulation and real data are concerned. The hadronic Z^0 decays contain two colinear jets of the same flavour.

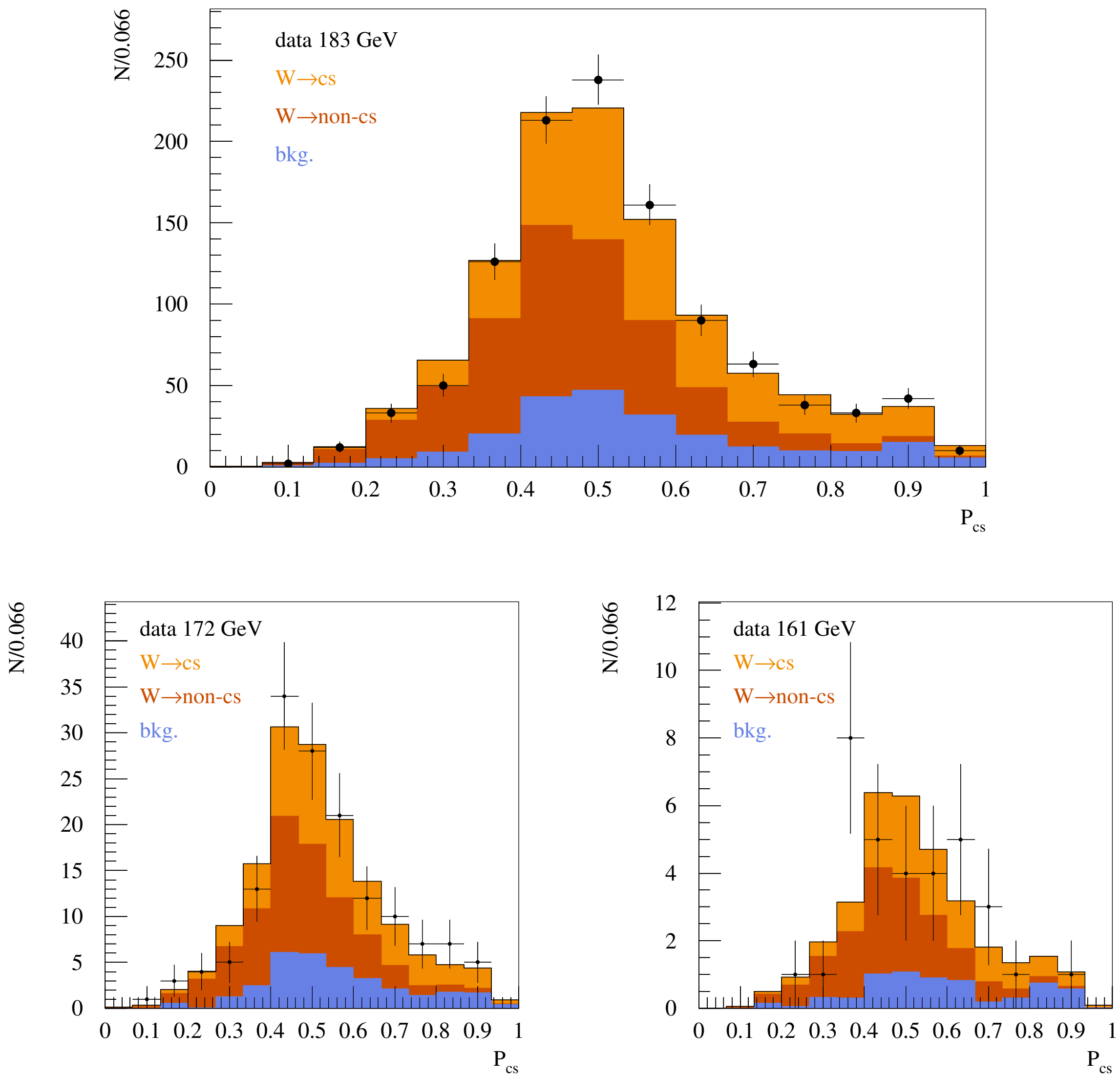

Figure 8.1: The expected and the measured P_{cs} distributions for 183, 172, and 161 GeV samples. The expected distributions correspond to the measured value of $|V_{cs}|$. They are divided into contributions from the $W^{\pm} \to cs$ di-jets, $W^{\pm} \to$ non $- cs$ di-jets and the di-jets from non-W^+W^- events.

Fragmentation of two jets can be considered as independent to a very good approximation [38]. The flavour ratios $N_{Z^0 \to b\bar{b}}/N_{Z^0 \to hadrons}$, $N_{Z^0 \to c\bar{c}}/N_{Z^0 \to hadrons}$, .. are measured with a high precision at LEP1 and SLD [86].

8.2.1 Corrections of lifetime tag probability

As far as the lifetime tag is concerned we are interested in three groups of flavours: $f = uds$, c and b. By applying a cut on the variable $P^{c'}$ for one of two jets in an event a sample with changed flavour contents is obtained. The flavour ratios $r^{f,s}$ after the cut s has been applied are obtained from the simulation. Each of three flavour groups has a specific distribution of $P^{c'}$. They are extracted from the simulation, too. We will denote these distributions by $g^{f,s}$ and normalise them to unity. Here we account that $g^{f,s}$ depends also on the cut s in the opposite jet. A weak dependence is due to some correlation between two jets.

If the same cut s is applied in the simulation and real data, we can compare the $P^{c'}$ distributions of remaining jets. Let us assume the following relation:

$$N_i^s = N^s \cdot r^{f,s} \cdot g_i^{f,s} \cdot c_i^f, \tag{8.3}$$

where N_i^s is the number of real events found in the i-th bin of the $P^{c'}$ distribution whereby N^s events are accepted in all bins together. c_i^f is the correction factor to the simulated single flavour distribution $g^{f,s}$ in the i-th bin. It ensures that the corrected expected number of events meets the measured one in each bin of $P^{c'}$. The correction factors are assumed to be independent on the cut s. For each bin there are three correction factors; one for each flavour group. Therefore, we need at least three different samples s to be able to calculate the correction factors by solving three linear equations with three unknowns c_i^f for each bin. For a good precision, the samples have to be as orthogonal as possible in terms of different flavour ratios. A sample enriched with the light flavour jets is obtained by selecting events with a low $P^{c'}$ value for the opposite jets. The second sample is obtained by selecting jets with a medium $P^{c'}$ probability resulting in an enhanced content of c jets. A sample enriched with b jets is obtained by accepting jets where the opposite jet has a very high $P^{c'}$ probability. The selected regions and comparison of real data and uncorrected simulation for three samples is shown in Figure 8.2. The correction factors c_i^f are obtained by the maximum likelihood fit of all three samples simultaneously using the condition in Eq. 8.3.

The flavour ratios $r^{f,s}$ obtained from the simulation implicitly depend on the assumed single flavour distributions g^f with no cuts applied. In the first step the flavour ratios are obtained with the uncorrected distributions g^f. In the next step we correct g^f

with the obtained correction factors. As a consequence the flavour ratios change. The resolving of linear equations is then repeated with the new flavour ratios resulting in slightly different correction factors. These iterative steps are repeated until correction factors between two consecutive steps do not differ any more. At the end the corrected simulated distributions fully match the measured distributions for all samples s simultaneously.

The obtained correction factors for three flavour groups are shown in Figure 8.3 using the Z^0 sample collected in the year 1997. There seems to be more than 40% less entries from c jets at high values of $P^{c'}$ with regard to the uncorrected simulated distribution. On the other hand, the number of light flavour jets is about 80% larger than initially expected in this region of $P^{c'}$ values. Therefore, after the correction, the $P^{c'}$ distributions for c and light flavour jets become more similar. This degrades the separating power between c jets and light flavour jets with respect to the original simulation.

Separate correction factors were obtained for Z^0 runs in the years 1996 and 1997. To ensure reliability of the estimates also for the high energy runs, the time stability of the inclusive $P^{c'}$ distribution was followed. The distribution was found stable during the whole period of data taking at the higher CMS energies.

8.2.2 Corrections of particle identification

The method used to correct the simulated distributions related to the particle identification is conceptually the same as the one practiced for the lifetime tag. Here, we have to distinguish between four flavour groups: ud, c, s and b. Therefore, we need at least four subsamples with different flavour ratios. Since many subsamples are required and many distributions have to be corrected, a large sample of hadronic Z^0 decays collected in the year 1994 is analysed. Since then the RICH counters have not changed hardware wise and the tuning algorithm remained unchanged. The stability of agreement between the simulation and real data was checked by comparing relevant distributions for years 1994, 1996 and 1997. No significant difference between the years was observed, thus allowing us to conclude that the year 1994 can be used to estimate performance of the particle identification at LEP2.

To extract subsamples with different flavour ratios the three criteria from the lifetime tag are retained. The sample with enriched u, d, s content is split into samples enriched with u, d jets and s jets. The u, d sample is obtained by requiring a fast identified pion in the opposite jet while the s sample contains at least one fast kaon in the opposite jet. Comparison between the uncorrected simulation and real data for some quantities of interest is shown in Figure 8.4. The largest discrepancy is observed for the number and the momentum distribution of identified kaons in the ud enriched sample. It seems as if there were more fast kaons and less slow kaons produced in the fragmentation of u and d jets.

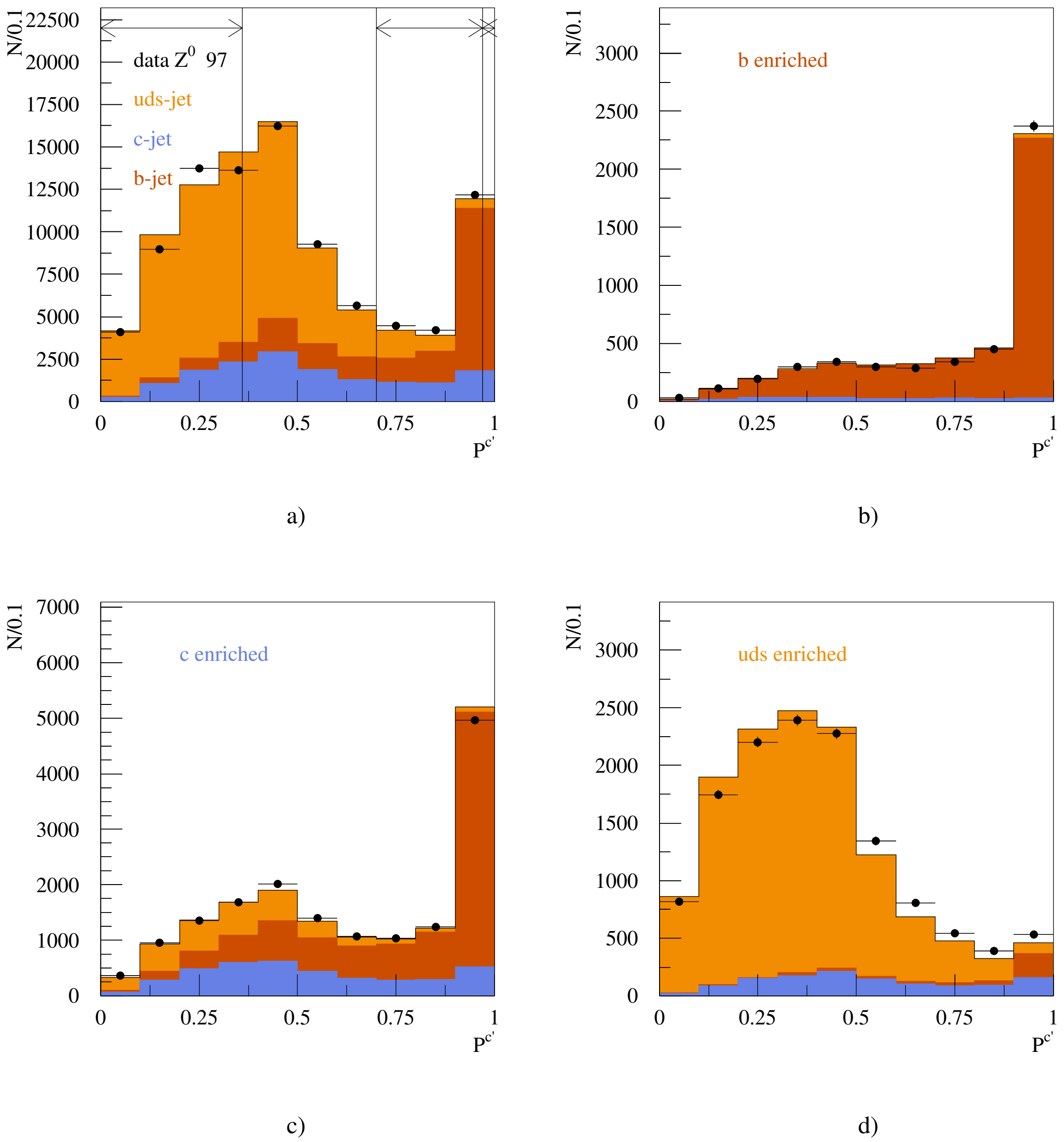

Figure 8.2: The simulated and the measured $P^{c\prime}$ distributions for various cuts in the opposite jets using hadronic Z^0 decays collected in 1997: **a)** the inclusive distribution showing the selected regions of the $P^{c\prime}$ distribution used to obtain three samples with enriched contributions of a single flavour, **b)** $P^{c\prime}$ distribution with an enriched b jet content, **c)** an enhanced c jet content, **d)** the sample enriched with the light flavour jets.

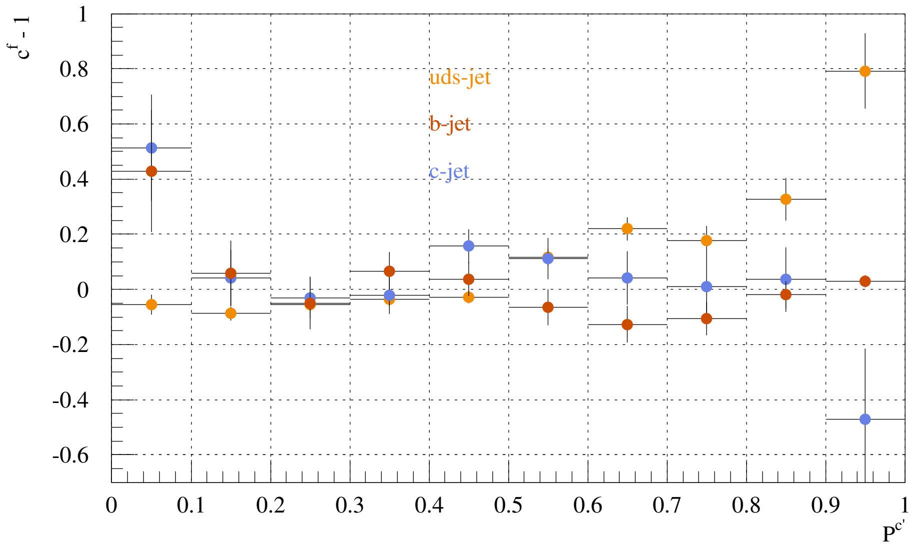

Figure 8.3: Flavour dependent correction factors of the simulated $P^{c\prime}$ distributions obtained from the 1997 Z^0 events.

It is not very likely that the effect is due to the detector simulation since the distributions related to other flavours, in particular b and c jets, agree much better. The simulation of fragmentation process is a more likely candidate for the source of discrepancy. The correction factors to the simulated flavour distributions are obtained by solving linear equations for the four samples. The corrections are shown in Figure 8.5. Apart from u and d jets, they are relatively close to unity with regard to the statistical uncertainties. A similar level of agreement was found for the second and the third fastest kaons and pions as well.

8.2.3 Correction of the fitted value of $|V_{cs}|$

The obtained corrections of simulated $P^{c\prime}$ distributions and momentum spectra of identified particles are propagated to correct the fitted value of $|V_{cs}|$ ($|V_{cs}^{fit}|$). For this purpose two samples of W^+W^- events and background events are generated. They are obtained from the ordinary simulated events by replacing the initially generated values of $P^{c\prime}$ as well as momenta and identifications of particles. For the first sample the new values are provided by a random generation according to the uncorrected distributions of a given jet flavour. For the second sample the values are generated according to the corrected distributions. The distributions from the first sample are equal to those from the original simulation on the single-jet basis. However, there might be differences on the event-by-event basis since the values are generated on the single-jet basis regardless to the event

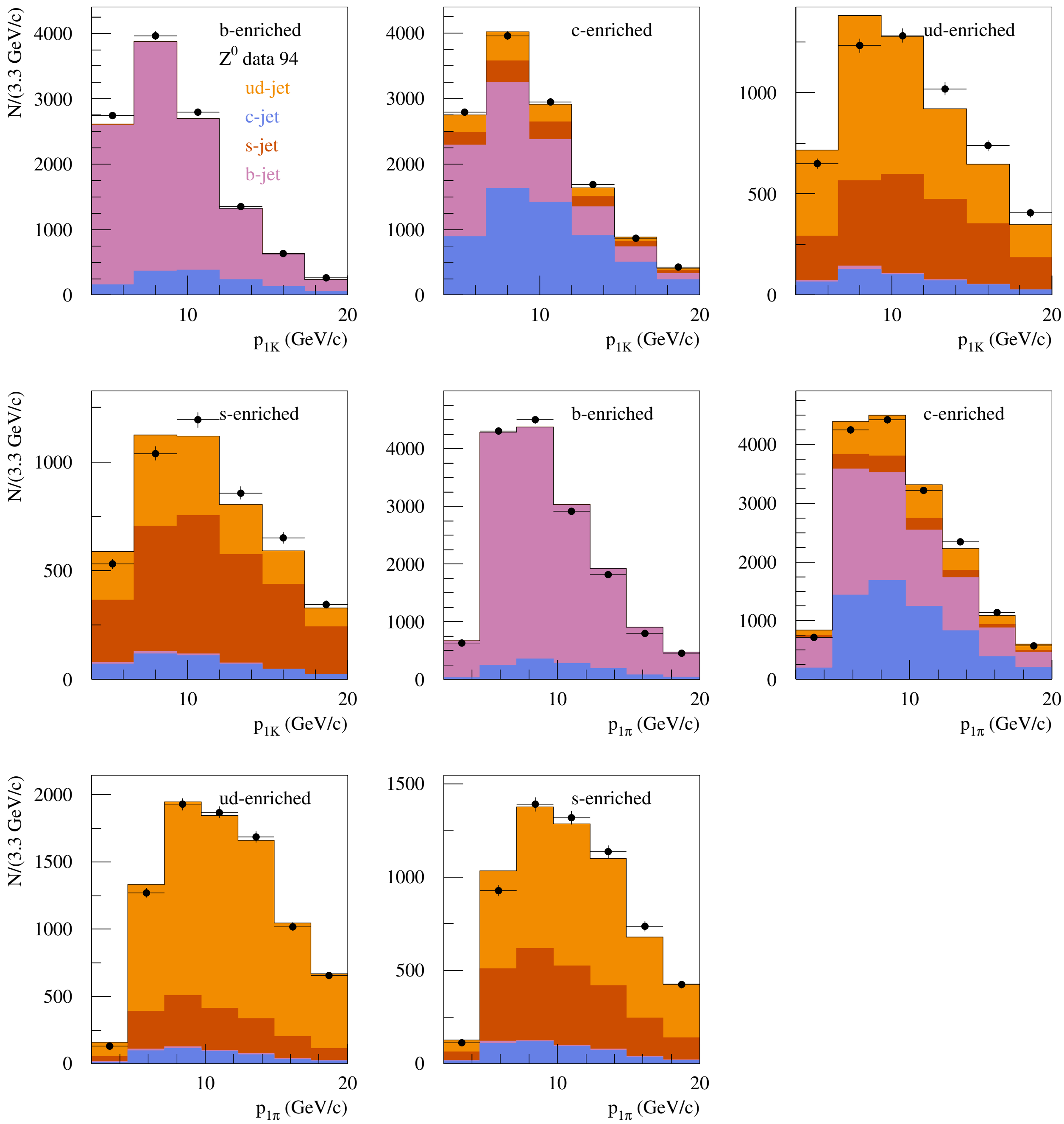

Figure 8.4: The expected and the measured momentum spectra of identified leading kaons and pions in jets from Z^0 decays collected in 1994. The simulated distributions are normalised such that the total number of accepted events is equal in the real data and in the simulation for each of the four samples separately.

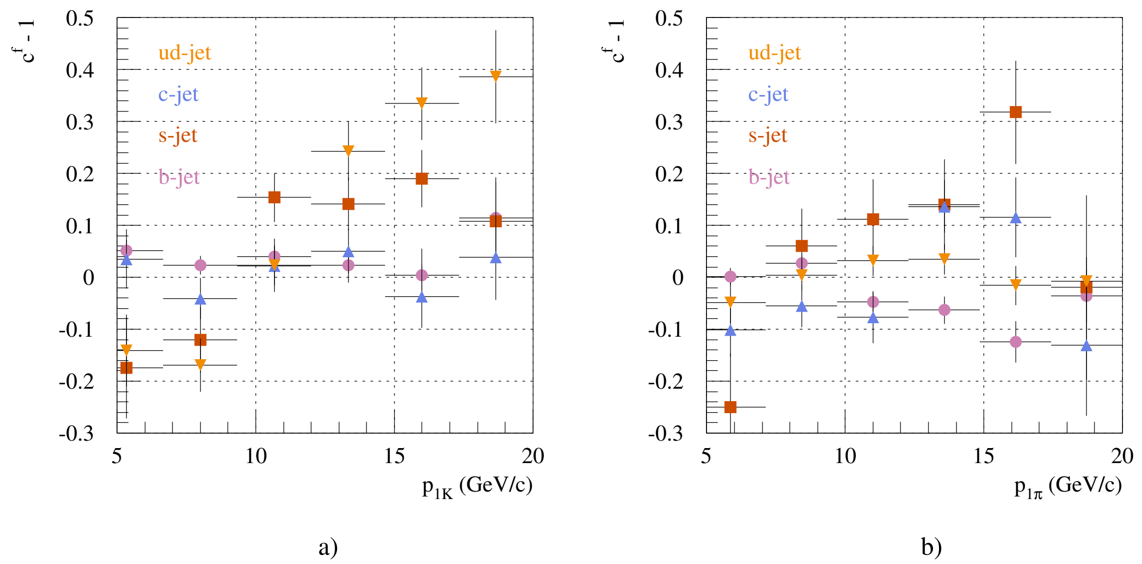

Figure 8.5: Flavour dependent correction factors to the simulated momentum spectra of identified leading kaons **a)**, and leading pions **b)**, obtained from the 1994 Z^0 events.

topology, possible correlation among jets within an event, etc. This reflects in slightly different distributions of the probability P_{cs} for the ordinary simulation and the first sample. Namely, to derive P_{cs} two jets within an event are combined. A small difference between the two P_{cs} distributions is an indication for a small interjet correlation. For reliability of the presented method it is even not important how large this correlation is. What is important is that differences between the simulation and real data are small as far as the interjet correlation is concerned. It is assumed that eventual differences in the correlation have a negligible impact on the fitted results.

The first generated sample plays the role of an ordinary simulation and provides the expected P_{cs} distribution. It is used to fit the P_{cs} distribution obtained from the second (corrected) sample that was generated with a certain value $|V_{cs}^{gen}|$. The second sample therefore plays the role of real data. The fitted value $|V_{cs}^{fit'}|$ will in general differ from the generated value $|V_{cs}^{gen}|$ because of the corrections included in the second sample. The difference between the two represents bias of the fitted value $|V_{cs}^{fit'}|$ with respect to the true value $|V_{cs}^{gen}|$. In general, the shift depends on the generated value $|V_{cs}^{gen}|$. To estimate the shift for the real data we found the value of $|V_{cs}^{gen}|$ where the fitted value $|V_{cs}^{fit'}|$ meets the fitted value $|V_{cs}^{fit}|$ for the real data. The value of $|V_{cs}^{gen}|$ is used as the corrected and final measured value of $|V_{cs}|$ ($|V_{cs}| = |V_{cs}^{gen}|$). The fitted value $|V_{cs}^{fit}|$ and the corrected value $|V_{cs}|$ are presented in Table 8.1. The largest difference between the fitted and the corrected value of -0.07 has been found for the 172 GeV sample. Still, the difference amounts to only about 20% of the statistical uncertainty. Relatively small corrections are partially due to a cancellation between the corrections from the lifetime tag and the particle identification. The corrections due to the lifetime tag are somewhat larger and tend to lower the fitted value $|V_{cs}^{fit}|$. On the other hand, the corrections due to the particle identification shift $|V_{cs}|$ to higher values than the value obtained from the fit.

8.2.4 Correction of statistical uncertainty

The statistical uncertainty σ_{stat}^{fit} of the fitted value $|V_{cs}^{fit}|$ depends on the expected separating power between the cs di-jets and the non-cs di-jets as well as on the background distribution. If the 'true' separating power was different from the one assumed in the fit, the 'true' statistical uncertainty σ_{stat} would also be different than σ_{stat}^{fit}. To estimate the relative difference between σ_{stat}^{fit} and σ_{stat} the two samples generated with and without corrections for the lifetime tag and the particle identification are used again (see previous Section). First, the corrected P_{cs} distribution generated with the final value ($|V_{cs}|$) (see Table 8.1) is fitted with a statistically independent corrected distribution. The corresponding statistical uncertainty will be denoted by σ_{stat}^{corr}. Secondly, the same sample is fitted with the uncorrected P_{cs} distribution leading to σ_{stat}^{uncorr}. The 'true' statistical uncertainty σ_{stat} is obtained by scaling σ_{stat}^{fit} as follows:

$$\sigma_{stat} = \frac{\sigma_{stat}^{corr}}{\sigma_{stat}^{uncorr}} \cdot \sigma_{stat}^{fit} \tag{8.4}$$

The relative difference between σ_{stat} and σ_{stat}^{fit} is presented in Table 8.1. The corrected statistical uncertainty σ_{stat} is larger than σ_{stat}^{fit} for all CMS energies. Due to the lifetime tag corrections the increase is between 8% and 20% while the corrections of particle identification increase the statistical uncertainty between 4% and 9%. The largest overall increase of about 26% has been found for the 183 GeV sample. Thus, the correction of the statistical uncertainty is non-negligible.

Among different pieces of information, the particle identification is the most important for the final precision. It alone results in about 30% better precision than the lifetime tag alone (Table 8.1). The inclusion of the $W^{\pm}$ charge separation and the separation between the up-like and the down-like quarks improves the final precision by about 10%.

The scaling of statistical uncertainty (Eq. 8.4) accounts also for a dependence of the statistical uncertainty on the measured value of $|V_{cs}|$. The expected statistical uncertainty as a function of $|V_{cs}|$ is shown in Figure 8.6. The quantity that is approximately insensitive to the value of $|V_{cs}|$ is the relative uncertainty $\sigma(|V_{cs}|)/|V_{cs}|$ which should therefore be used if precisions of two different values are compared. On the other hand, the expected statistical uncertainty of r_{cs} is almost independent on the value of r_{cs}.

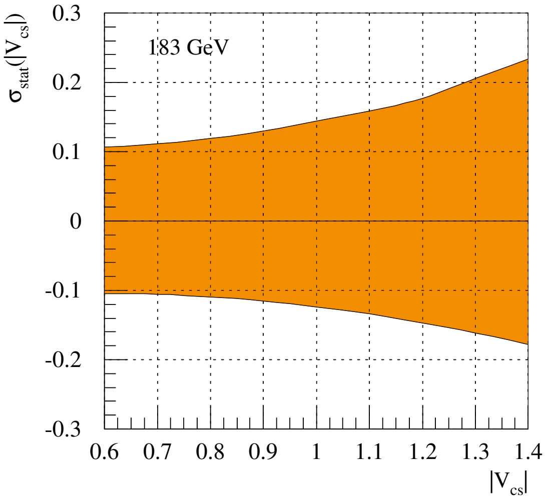

Figure 8.6: The expected statistical uncertainty of $|V_{cs}|$ as a function of the measured value of $|V_{cs}|$ at the CMS energy of 183 GeV.

	161 GeV	172 GeV	183 GeV	combined
$\|V_{cs}\|$ r_{cs}	$0.66^{+0.77}_{-0.55} \pm 0.07$ $0.29^{+0.37}_{-0.28} \pm 0.04$	$1.08^{+0.44}_{-0.31} \pm 0.08$ $0.53^{+0.16}_{-0.16} \pm 0.04$	$1.10^{+0.16}_{-0.14} \pm 0.05$ $.535^{+.067}_{-.067} \pm .025$	$1.09^{+0.14}_{-0.13} \pm 0.05$ $.530^{+.061}_{-.061} \pm .022$
$\|V_{cs}^{fit}\|$	$0.79^{+0.64}_{-0.46}$	$1.17^{+0.44}_{-0.31}$	$1.11^{+0.12}_{-0.11}$	
$\Delta\|V_{cs}\|$ (P^c) $\Delta\|V_{cs}\|$ (P^f_{id})	-0.16 +0.03	-0.16 +0.07	-0.07 +0.06	
$\sigma_{stat}/\sigma^{fit}_{stat}$ (P^c) $\sigma_{stat}/\sigma^{fit}_{stat}$ (P^f_{id})	1.17 1.09	1.08 1.04	1.20 1.05	
σ_{stat} (P^c only) σ_{stat} (P^f_{id} only)			± 0.27 ± 0.20	

Table 8.1: Results of the measurement of $|V_{cs}|$ using the flavour tagging of cs di-jets. The final values are $|V_{cs}|$ and r_{cs}. $|V_{cs}^{fit}|$ and r_{cs}^{fit} represent the values obtained by the likelihood fit. $\Delta|V_{cs}|$ is the applied shift of the fitted value. $\sigma_{stat}/\sigma^{fit}_{stat}$ is the relative difference between the corrected statistical uncertainty and the one given by the fit. $\sigma_{stat}(P^c$ only) and $\sigma_{stat}(P^f_{id}$ only) are the corrected statistical uncertainties if the lifetime tag or the identification were used alone, respectively.

8.3 Systematic uncertainty

The quoted results include the corrections due to discrepancies in the simulation of the lifetime tag and the particle identification. A residual uncertainty is due to the statistical uncertainty of the obtained correction factors. To estimate the uncertainty several samples were generated where the correction factors were varied according to the normal distribution of the statistical fluctuations. The variance of the fitted values of $|V_{cs}|$ is used as an estimate of the systematic uncertainty (Table 8.2). Note, that the uncertainty depends on the measured value of $|V_{cs}|$.

A comparable contribution to the systematic uncertainty is due to statistical fluctuations of the expected P_{cs} distribution. About 70% of the simulated events are used to obtain the distributions needed to calculate the probabilities. The remaining events are used to obtain the expected P_{cs} distribution which is therefore subject to relatively large statistical fluctuations (Table 8.2).

Since the expected P_{cs} distribution of W^+W^- events is normalised in the likelihood fit (Eq. 8.1), the uncertainty of the selection efficiency does not induce any uncertainty on the value of $|V_{cs}|$. This is true as long as the separating power of P_{cs} does not depend on values of the event probabilities P_{qqqq} and $P_{ql\nu}$ and possible differences in the event topology of accepted events. The same holds for possible differences between real data and simulation due to interferences between four-fermion diagrams.

The background events are not normalised, therefore, the uncertainties of the background level (Table 6.3 and 6.4) directly contribute to the uncertainty of the value of $|V_{cs}|$. As an additional check of the background simulation we relaxed cuts on the event probabilities to accept mostly background events. The observed differences in the P_{cs} distribution between the simulation and real data are compatible with those expected between the corrected and the uncorrected P_{cs} distribution. Therefore, there is no indication of any additional source of systematic uncertainty as far as the background is concerned.

Uncertainties due to the measurement errors of physical parameters, such as m_W, α_S, and the CKM elements, are negligible.

The impact of possible interconnection effects between different $W^\pm$ bosons in the hadronic decays is neglected, too. The interconnection phenomena affect slower particles that are of little importance in the flavour tagging of jets. Moreover, none of dedicated measurements of the interconnection effects has resulted in any evidence, yet.

We have checked also for a possible bias of the likelihood function (Eq. 8.1) by performing a number of likelihood fits using samples generated with different values of $|V_{cs}|$. The most-likely fitted-value coincides with the generated value of $|V_{cs}|$. The difference between the fitted and the generated value is smaller than the given statistical uncertainty

Source	161 GeV	172 GeV	183 GeV	combined
Lifetime tag	0.04	0.06	0.04	
Particle id.	0.01	0.02	0.02	
MC statistics	0.05	0.05	0.03	
Background level	< 0.01	0.01	< 0.01	
Total $\|V_{cs}\|$	0.07	0.08	0.05	0.05
Total (r_{cs})	0.04	0.04	0.03	0.02

Table 8.2: Contributions to the systematic uncertainty of the value of $|V_{cs}|$ from the flavour tagging of cs di-jets.

in about 68% of the fits. This result confirms reliability of the statistical uncertainty. With the help of the simulated samples we also proved that the fitted value of $|V_{cs}|$ does not depend on the number of accepted W^+W^- events in the two decay channels.

A complete list of contributions to the systematic uncertainty is displayed in Table 8.2. For the sample collected at a single CMS energy the individual contributions are combined as uncorrelated into the common uncertainty. For the combined result the contributions due to the background normalisation and the particle identification are considered as fully correlated among different CMS energies. Other contributions are combined as completely uncorrelated.

As an intuitive test of reliability of the measurement we compared the expected and the measured distributions of relevant quantities used to obtain P_{cs}. In Figure 8.8 we present comparison of angular distributions of the $W^\pm$ bosons and their decay products. The distributions of $P^{c'}$, the number of identified particles, and their momenta are shown in Figure 8.7. The expected distributions related to the particle identification and the lifetime tag are corrected with the obtained correction factors.

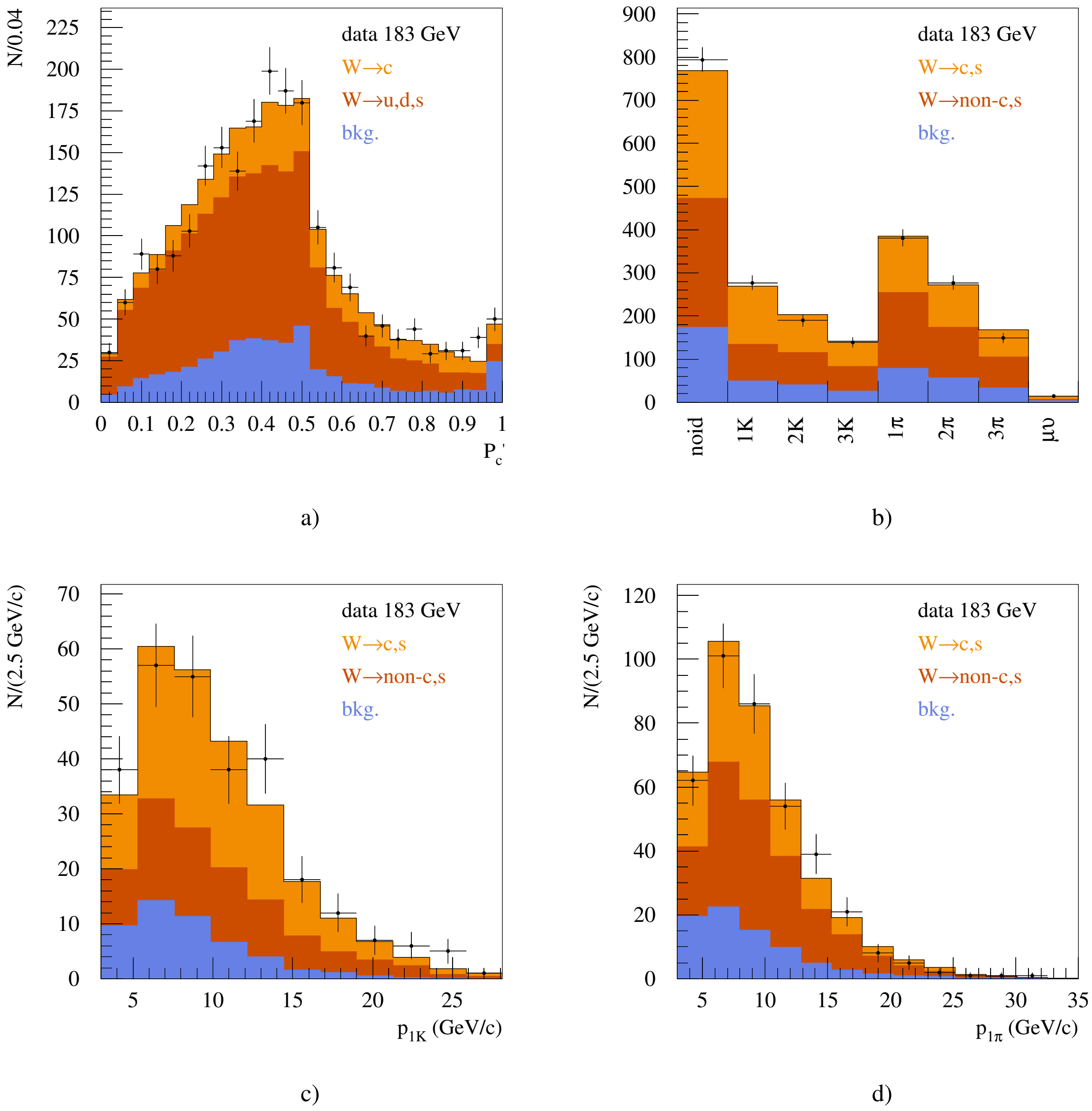

Figure 8.7: Comparison between the measured and the corrected expected distributions at 183 GeV; **a)** $P^{c\prime}$, **b)** the number of identified particles (noid = no identification), **c)** momentum distribution of leading kaons, **d)** momentum distribution of leading pions.

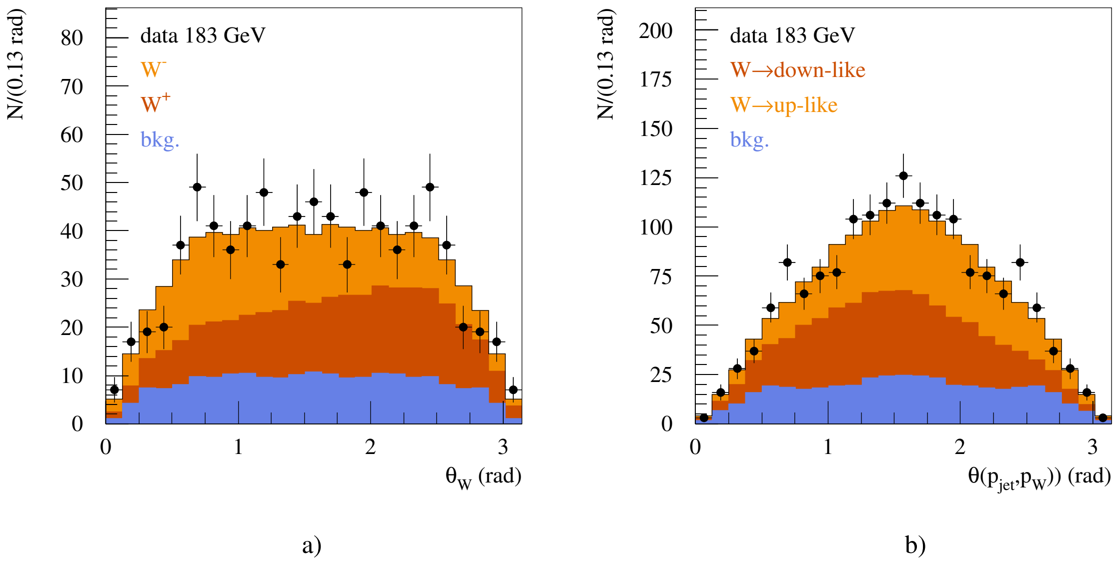

Figure 8.8: Comparison between the measured and the expected distributions in the hadronic W^+W^- decays at 183 GeV; **a)** the polar angle of $W^\pm$ bosons, **b)** the angle between a jet and the parent $W^\pm$ boson in its rest-frame. The distributions are by definition symmetric around $\pi/2$ as they include two $W^\pm$ bosons and four jets per event after the constraint fit has been performed.

9

Conclusions and outlook

9.1 Summary and conclusions

The study of decays of produced W^+W^- pairs at the LEP2 e^+e^- collider provided a precise measurement of the $|V_{cs}|$ element of the Cabbibo-Cobayashi-Maskawa matrix. The value of $|V_{cs}|$ was extracted from the measured hadronic branching ratio of the $W^\pm$ bosons and from the measured fraction of cs di-jets in the hadronic decays of $W^\pm$ bosons.

The analysed data were collected by the DELPHI detector at center of mass energies of 161, 172, and 183 GeV with integrated luminosities of about 10 pb^{-1}, 10 pb^{-1}, and 51 pb^{-1}, respectively.

The selection of W^+W^- events was performed separately in each of three main decay channels: hadronic, mixed, and leptonic decay channel. A probabilistic approach was used to combine different separating variables into the probability that an event is a W^+W^- event. The hadronic branching ratio of the $W^\pm$ bosons $Br_{W\to had}$ was obtained by the likelihood fit of the expected distributions of event probabilities to the measured ones. The fit was performed simultaneously for all considered decay channels and sub-channels by assuming the universality of leptons. This yields:

$$Br_{W\to had} = 0.678 \pm 0.013\,(\text{stat.}) \pm 0.008\,(\text{syst.}). \tag{9.1}$$

The value of $Br_{W\to had}$ was interpreted in terms of $|V_{cs}|$ whereby the measured values of other CKM elements were used [11]. The value of the strong coupling constant at the $W^\pm$ boson mass ($\alpha_S = 0.123$) is evaluated from the one measured at the mass of the Z^0 boson [11]. In this way we obtained:

$$|V_{cs}|(Br_{W\to had}) = 0.99 \pm 0.06\,(\text{stat.}) \pm 0.04\,(\text{syst.}). \tag{9.2}$$

The systematic uncertainty is dominated by the uncertainty of the selection efficiency and the background normalisation.

The second free parameter of the likelihood fit was the total cross-section for the production of W^+W^- pairs. The total cross-sections $\sigma_{W^+W^-}$ measured at different CMS energies are the following:

$$\begin{aligned}
\sigma_{W^+W^-} &= \ \ 3.57^{+0.91}_{-0.79}\,(\text{stat.}) \pm 0.16\,(\text{syst.})\ pb \text{ at } 161 \text{ GeV}, \\
\sigma_{W^+W^-} &= 12.26^{+1.44}_{-1.35}\,(\text{stat.}) \pm 0.34\,(\text{syst.})\ pb \text{ at } 172 \text{ GeV}, \\
\sigma_{W^+W^-} &= 15.89^{+0.69}_{-0.67}\,(\text{stat.}) \pm 0.38\,(\text{syst.})\ pb \text{ at } 183 \text{ GeV}.
\end{aligned} \tag{9.3}$$

If the Standard Model branching ratios of the $W^\pm$ bosons are imposed, the measured cross-sections remain almost identical to the above results (Table 6.1).

In order to measure the fraction of cs di-jets in the hadronic decays of $W^\pm$ bosons we developed a method to tag the flavour of jets arising from the $W^\pm$ decays. This was achieved by exploiting momentum spectra of identified $K^\pm$, $\pi^\pm$, $\mu^\pm$, and by using the impact parameters of charged tracks. A probabilistic approach was applied to combine different pieces of information into the probability P_{cs} that a di-jet emerges from a c and an s quark. The fraction of cs di-jets in the hadronic decays of $W^\pm$ bosons, r_{cs}, was obtained by the likelihood fit of the expected P_{cs} distribution to the measured distribution. The fitted value was then corrected according to the observed differences between the simulated and real jets from hadronic Z^0 decays. In this way we obtained:

$$r_{cs} = 0.530 \pm 0.061\,(\text{stat.}) \pm 0.022\,(\text{syst.}).$$

The value of $|V_{cs}|$ is evaluated from r_{cs} by using the measured values of other CKM elements. This yields:

$$|V_{cs}|(r_{cs}) = 1.09^{+0.14}_{-0.13}\,(\text{stat.}) \pm 0.05\,(\text{syst.}). \tag{9.4}$$

The main contribution to the systematic uncertainty is due to the residual statistical uncertainty of the correction of the fitted value.

The two results of $|V_{cs}|$, Eq. 9.2 and Eq. 9.4, were combined into the single value. Since they are uncorrelated, the two likelihood functions were multiplied to obtain the combined likelihood function (Figure 9.1). This gives:

$$|V_{cs}|(r_{cs} \otimes Br_{W\to had}) = 1.01 \pm 0.06\,(\text{stat.}) \pm 0.03\,(\text{syst.}) \tag{9.5}$$

The combined value and its precision are dominated by the result obtained from the hadronic branching ratio. On the other hand, the value of $|V_{cs}|$ derived from the fraction of cs di-jets is more direct as no assumption about the weak interaction of leptons is needed. The systematic uncertainties of two measurements were combined as uncorrelated apart from the contribution due to the background normalisation. The latter was considered as fully correlated.

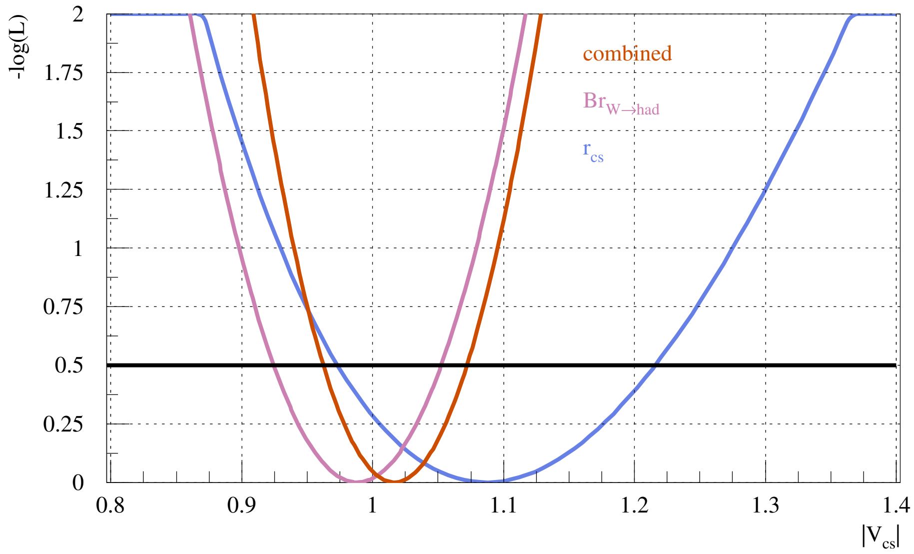

Figure 9.1: Negative logarithm of the likelihood functions for the measurements based on $Br_{W\to had}$, r_{cs} and combination of the two. The interval of one standard deviation is presented by the horizontal line indicating the point where the value of $-log(\mathcal{L})$ increases by 0.5 with respect to its minimum value.

The combined value of V_{cs} (Eq. 9.5) is consistent with the Standard Model that at 90% confidence level predicts the value between 0.9737 and 0.9753 whereby three quark families and the unitarity of the CKM matrix are assumed. The achieved precision of the value of $|V_{cs}|$ exceeds by a factor of 2.5 the combined precision of all measurements before the LEP2 measurements took place. The unitarity constraint without any assumption on the number of quark families, limits the 90% confidence interval for V_{cs} between 0.925 and 0.975. Further limitation to three quark families does not change the existing constraints presented in Table 2.8 since the achieved precision of $|V_{cs}$ is still significantly below the precisions of other measured CKM elements.

9.2 Comparison with other measurements

In Section 2.1 we have presented the methods and the results of the $|V_{cs}|$ measurements before the LEP2 measurements took place. The first results of the measurement of $|V_{cs}|$ at LEP2 were published in the DELPHI note [84] by the author of this thesis and other members of Ljubljana group in the DELPHI collaboration. Soon after, measurements of $|V_{cs}|$ were performed also by other three collaborations at LEP. All of them have a similar capability to measure the hadronic branching ratio of $W^{\pm}$ bosons from which the value of $|V_{cs}|$ is extracted. Therefore, a similar precision was achieved by all LEP experiments [80, 79, 81] (see Figure 9.2). Differences between the experiments are somewhat more pronounced only for the estimated systematic uncertainties that at least for the time being do not limit the overall precision of measurements. The DELPHI published results on the hadronic branching ratio [76] are obtained by a different method than the one presented here. However, the results of the two analyses are fully compatible, except that our method provides about 5% lower statistical uncertainty in all channels.

Capability to tag flavour of jets depends much more on the detector used. DELPHI with the RICH counters is the only detector able to tag s jets with a reasonable efficiency. ALEPH ([78]) and OPAL ([82]) have precise silicon vertex detectors that enable tagging of c jets. They examine also identified leptons and inclusively reconstructed D and D^* mesons as an indication for c jets. An additional information is provided by studying multiplicity and momentum distribution of tracks within jets. The resolution of impact parameters measured with the L3 detector is worse than from the other three detectors. In order to tag c jets, they extensively exploit identified leptons, partially reconstructed D and D^* mesons, and jet shape properties such as multiplicity and momentum distributions.

There is a difference between interpretation of the DELPHI results and the results from other LEP experiments as far as the value of $|V_{cs}|$ from the flavour tagging is concerned. Other collaborations essentially measure the fraction of c jets in the hadronic $W^{\pm}$ decays. This fraction is then interpreted in terms of $|V_{cs}|$ by fixing other CKM elements to the measured values and assuming that there are no additional quarks to which c quarks could couple. We measured directly the fraction of cs di-jets within all di-jets emerging from $W^{\pm}$ decays. From this ratio the value of $|V_{cs}|$ is calculated by using the measured values of other CKM elements. The presented method is therefore more direct and sensitive to possible scenarios outside the SM.

The status of all measurements of the $|V_{cs}|$ element is graphically presented in Figure 9.2. The thin vertical line corresponds to the value predicted by the SM by assuming the unitarity of the CKM matrix and three quark families. This value is strongly limited by other CKM elements that have been measured with a higher precision. The broader band represents the SM limits without any assumption on the number of quark families. The limits are calculated with no LEP results. Apart from the value obtained by the L3 collaboration from $Br_{W\to had}$, all other results agree with the SM prediction within one standard deviation. As already stated, all LEP experiments achieved a similar precision of the hadronic branching ratio. Larger differences appear between the results based on the flavour tagging. The best precision achieved by the ALEPH collaboration is followed by our analysis with about 5% worse precision, if the relative uncertainty is used as the criterion. The other two collaborations claim significantly larger uncertainty. Apart from

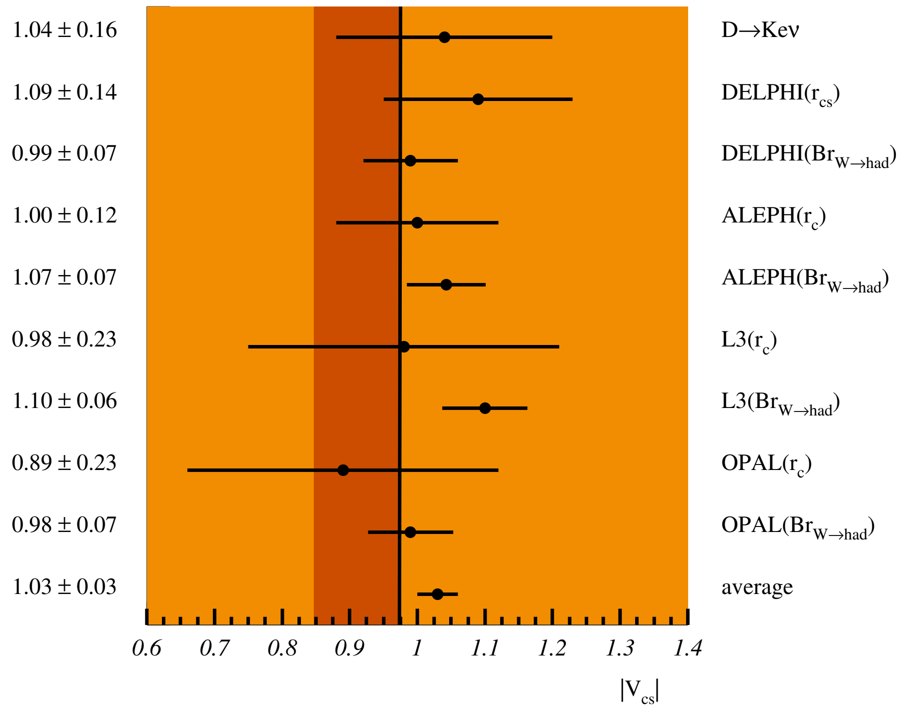

Figure 9.2: The results of all measurements of the $|V_{cs}|$ element. The quoted errors include statistical and systematic uncertainties. The thin vertical line represents the SM limit if three quark families are assumed. The broader band corresponds to no limit on the number of families.

the OPAL result from the c-tag, all other results favour larger values of $|V_{cs}|$ than predicted by the SM. The average value calculated from the individual results is about 1.7 standard deviations above the predicted SM value. To account for correlation of the systematic uncertainties between the LEP experiments we followed the method and the assumptions of the LEP Electroweak Working Group which calculated the common value of $|V_{cs}|$ from $Br_{W\to had}$ using preliminary results [86]. In general, the uncertainty arising from the initial state radiation, the fragmentation models, and other QCD processes is considered as fully correlated. In this way, about 70% of the systematic uncertainty per single experiment appears to be correlated. A possible correlation of the systematic uncertainties from the flavour tagging is neglected. In any case the results from the flavour tagging are of little importance for the precision of the combined value. Among experiments DELPHI and ALEPH contribute most. Due to the way we treated and estimated the systematic uncertainty from the flavour tag it could be anticipated that our systematic uncertainty is to a large extend uncorrelated with other measurement at LEP.

9.3 Future prospects

In the near future no other experiment is expected to measure $|V_{cs}|$ with the precision of LEP. A particularly interesting question is whether the tendency towards values larger than 0.977 will persist as this directly contradicts the SM and opens many questions.

The year 2000 is foreseen to be the last year of LEP operation. Until then the total integrated luminosity at high energies should amount to about 500 pb^{-1}. The number has to be compared to approximately 70 pb^{-1} analysed in the presented measurement. In this respect, the statistical uncertainty of the measured value of $|V_{cs}|$ should decrease by a factor of about 2.5 until the end of the LEP era.

The expected final statistical-precision of $|V_{cs}|$ from the flavour tagging is about 0.05 if no improvement in the separating power will be achieved. As there are still unused quantities, each contributing a small piece of information to the flavour tagging of jets, we expect about 20% reduction of the statistical error by inclusion of additional information. The systematic uncertainty is also likely to decrease with the increasing number of collected events. With the integrated luminosity of 500 pb^{-1} the statistical and the systematic uncertainty of about 0.04 each seem to be achievable at the end of LEP data taking.

For the analysis based on the hadronic branching ratio the systematic uncertainty is expected to dominate unless a much more profound treatment will be performed. As discussed in Section 6.2 the method used to estimate the systematic uncertainty is based on rather conservative assumptions. The differences observed in the merged events could be used to correct the fitted value of the hadronic branching ratio instead of attributing these differences to the systematic uncertainty. Since Z^0 events are mostly used to estimate the systematic uncertainty, a sufficient number of Z^0 events is essential to keep the uncertainty low. If they were collected also during high energy runs and at the end of data taking period each year, the uncertainty due to the detector stability could be lowered and better controlled. We estimate that an overall precision of about 0.03 is achievable for the value of $|V_{cs}|$ obtained from the hadronic branching ratio.

References

[1] N. Cabibbo, Phys. Rev. Lett. 10 (1963) 531 .

[2] M. Gell-Mann, Phys.Lett. 8 (1964) 214.

[3] G. Zweig, CERN-Reports/8128/TH401 (1964).

[4] S.L. Glashow, Nucl. Phys. 22B (1961) 579.

[5] A. Salam, J.C. Ward, Phys. Lett. 13 (1964) 168.

[6] S. Weinberg, Phys. Rev. Lett. 19 (1967) 1264.

[7] G. 't Hooft, Nucl. Phys. B35 (1971) 167.

[8] O. Nactmann, *Elementary Particle Physics*, Springer-Verlag (1990).

[9] D. Perkins, *Introduction to High Energy Physics*, Addison-Wesley (1987).

[10] F.Halzen, A.D. Martin, *Quarks and Leptons*, John Wiley and Sons (1984).

[11] Particle Data Group, Review of Particle Physics, Eur. Phys. J. C (1998) 1.

[12] M. Kobayashi, T. Maskawa, Progr. Theor. Phys. 49 (1973) 652.

[13] L.L. Chau, W.Y. Keung, Phys. Lett. B181, (1984) 1802.

[14] H. Abramowitz et al., Z. Phys. C15 (1982) 19.

[15] A. Bean et al., Phys. Lett. 66 (1993) 647.

[16] Z. Bai et al., Phys. Rev. Lett. 66 (1991) 1011.

[17] J. Adler et al., Phys. Rev. Lett. 62 (1989) 1821.

[18] J.R. Raab et al., Phys. Rev. D37 (1988) 2391.

[19] G. Arnison et al., Phys. Lett. 122B (1983) 476.

[20] M. Banner et al., Phys. Lett. 122B (1983) 476.

[21] F. Abe et al., Phys. Rev. Lett. 75 (1995) 1017.

[22] B. Abbott et al., Phys. Rev. Lett. 79 (1997) 1441.

[23] W. Beenakker, F.A. Berends et al., WW cross section and distributions, Physics at LEP2, eds. G. Altarelli, T. Sjostrand and F. Zwirner, CERN 96-01 (1996) Vol. 1.

[24] Z. Kunszt, W.J. Stirling et al., Determination of the mass of the W boson, Physics at LEP2, eds. G. Altarelli, T. Sjostrand and F. Zwirner , CERN 96-01 (1996) Vol. 1.

[25] T. Muta, R. Najima and S. Wakaizumi, Mod. Phys. Lett. A1 (1986) 203.

[26] F. Boudjema, B. Mele et al., Standard Model Processes, Physics at LEP2, eds. G. Altarelli, T. Sjostrand and F. Zwirner, CERN 96-01 (1996) Vol. 1.

[27] P. Nason, B.R. Webber et al., QCD Physics at LEP2, eds. G. Altarelli, T. Sjostrand and F. Zwirner, CERN 96-01 (1996) Vol. 1.

[28] P. Aurenche, G.A. Schuler et al., $\gamma\gamma$ Physics, Physics at LEP2, eds. G. Altarelli, T. Sjostrand and F. Zwirner, CERN 96-01 (1996) Vol. 1.

[29] F. James, MINUIT Function Minimisation and Error Analysis, CERN Program Library Long Writeup D506.

[30] W.T. Eadie, D. Drijard, F.E. James, M. Ross, B. Sadoulet, *Statistical Methods in Experimental Physics*, North-Holland (1971).

[31] F.A. Berends, R. Kleiss, Comput. Phys. Commun. 85 (1996) 11.

[32] T. Sjostrand, PYTHIA 5.7 and JETSET 7.4 Physics and Manual, CERN-TH (1993) 7112.

[33] L. Lonnblad, Comput. Phys. Commun. 71 (1992) 15.

[34] D. Bardin et al., GENTLE/4fan v2.0: A Program for the Semi-Analytic Calculation of Predictions for the Process $e^+e^- \to 4f$, HEP-PH/9612409 (1996).

[35] C.J. Parkes, P.B. Renton, H.T. Phillips, A Study of Four Fermion Final State Interference relevant to the Measurement of the W^+W^- Cross-Section and the W Mass, DELPHI 97-96 (1997).

[36] C.J. Parkes, A Determination of the W Boson Mass near the W-Pair Production Threshold, Ph.D. Thesis, Uni. of Oxford 1998.

[37] eds. G. Altarelli, T. Sjostrand, F. Zwirner, et al., Event generators, Physics at LEP2, CERN 96-01 (1996) Vol. 2.

[38] eds. G. Altarelli, R. Kleiss, C. Verzegnass et al., Z Physics at LEP1 Vol. 1, CERN 89-08 (1989).

[39] M. Battaglia et al., A Search for Interconnection Effects in WW Decays using Identified Hadrons, DELPHI 98-101, submitted to the ICHEP'98 Vancouver.

[40] P. Abreu et al., Particle Correlations in $e^+e^- \to W^+W^-$ and $q\bar{q}$ Events, DELPHI 98-130 CONF 91, submitted to the ICHEP'98 Vancouver.

[41] J. Ellis, K. Geiger, Phys. Rev. D54 (1996) 1967.

[42] B.R. Webber, Colour Reconnection and Bose-Einstein Effects, HEP-PH/9708463 (1997).

[43] J. Ellis, K. Geiger, Phys. Lett. B404 (1997) 230.

[44] L. Lonnblad, T. Sjostrand, Modelling Bose-Einstein Correlations at LEP2, HEP-PH/9711460 (1997).

[45] R. Barate et al., Bose-Einstein Correlations in W-pair Decays, CONF 97 HEP97 paper 590.

[46] P. Abreu et al., Phys. Lett. B401 (1997) 181.

[47] P. Abreu et al., Zeit. Phys. C73 (1996) 11-60.

[48] P. Abreu et al., DELSIM User's Guide, DELPHI 89-67 (1989).

[49] C. Green, T. Bowcock, FASTSIM Manual, http://wwwcn.cern.ch/ greenc/fsimguide/fsimguide.html.

[50] DELPHI Collaboration, DELANA User's Guide, DELPHI 89-44 (1989).

[51] P. Billoir, Nucl. Instr. Meth. 225 (1984) 352.

[52] Particle Data Group, Review of Particle Physics, Phys. Rev. D54 (1996) 1.

[53] LEP Energy Working Group, LEP Energy Calibration in 1996, LEP Energy Group/97-01 (1997).

[54] S. Myers, The LEP Collider, From Design to Approval and Commissioning, CERN/91-08.

[55] P. Aarnio et al., Nucl. Instr. Meth. A303 (1991) 223.

[56] P. Abreu et al., Nucl. Instr. Meth. A378(1996) 57.

[57] A.C. Benvenuti et al., IEEE Trans. Nucl. Sci. 42 (4) (1995) 478.

[58] V. Bocci et al., Architecture and Performance of the DELPHI Trigger System, CERN-PPE/94-141.

[59] P. Chochula et al., The DELPHI Silicon Tracker at LEP2, CERN-PPE/97-155.

[60] G. Borisov, C. Mariotti, Fine Tuning of Track Impact Parameter Resolution of the DELPHI Detector, DELPHI 95-142 PHYS 567.

[61] G. Borisov, C. Mariotti, Nucl. Instr. Meth. A372 (1996), 181.

[62] G.V. Borisov, C. Mariotti, Performance of b-tagging at LEP2, DELPHI 97-16 (1997).

[63] W.J. Murray, Improved B tagging using Impact Parameters, DELPHI 95-167 (1995).

[64] W. Adam et al., Nucl. Instr. Meth. A343 (1994) 68.

[65] G. Lenzen et al., Nucl. Instr. Meth. A343 (1994) 268.

[66] W. Adam et al., IEEE Trans. Nucl. Sci. 41 (4) (1994) 866.

[67] M. Battaglia, P.M. Kluit, Particle Identification using the RICH detectors based on the RIBMEAN package, DELPHI 96-133 (1996).

[68] E. Schyns, NEWTAG- π, K, p Tagging for Delphi RICHes, DELPHI 96-103 (1996).

[69] W. Adam et al., Nucl. Instr. Meth. A343 (1994) 1.

[70] J. Seguinot, T. Ypsilantis, Nucl. Instr. Meth. 142 (1977) 377.

[71] P. Baillon, Nucl. Instr. Meth. A238 (1985).

[72] E. Schyns, Measurement of $\pi^{\pm}, K^{\pm}, p$ and $\bar{p}$ production in $Z^0 \to q\bar{q}$, $Z^0 \to b\bar{b}$ and $Z^0 \to u\bar{u}, d\bar{d}, s\bar{s}$, Ph.D. Thesis, WUB-DIS 96-22 (1996).

[73] P. Abreu et al., SPRIME, DELPHI 96-124 (1996).

[74] P. Abreu et al., Phys. Lett. B397 (1997) 158.

[75] P. Abreu et al., CERN-PPE/97-160

[76] P. Abreu et al., W-pair production cross-section and W branching ratios in e^+e^- interactions at 183 GeV, CERN-EP/99-47 (1999).

[77] L3 Collaboration, Preliminary results on charm production in W decays, L3 Note 2232, submitted to the ICHEP'98 Vancouver.

[78] ALEPH Collaboration, Measurement of $|V_{cs}|$ in hadronic W decays, ALEPH 98-011, submitted to the ICHEP'98 Vancouver.

[79] OPAL Collaboration, W^+W^- production and triple gauge boson couplings at LEP energies up to 183 GeV, CERN-EP/98-167 (1998).

[80] ALEPH Collaboration, Measurement of W-pair production in e^+e^- collisions at 183 GeV, CERN-EP/99-035 (1999).

[81] L3 Collaboration, Measurement of W-Pair Cross Sections in e^+e^- Interactions at $\sqrt{s} = 183$ GeV and W-Decay Branching Fractions, CERN-EP/98-121 (1998).

[82] OPAL Collaboration, Measurement of R_c^W in $e^+e^- \rightarrow W^+W^-$ at $\sqrt{s} = 183$ GeV, OPAL PN355, submitted to the ICHEP'98 Vancouver.

[83] P. Abreu et al., Phys. Lett. B439 (1998) 209.

[84] B. Erzen, B. Golob, T. Podobnik, Measurement of the $|V_{cs}|$ in Hadronic W-decays at LEP-2, DELPHI 97-9.

[85] B. Erzen, B. Golob, T. Podobnik, Measurement of $|V_{cs}|$ using W decays at LEP2, DELPHI 98-107, Contribution to ICHEP'98.

[86] The LEP Electroweak Working Group, and the SLD Heavy Flavour Group, A Combination of Preliminary Electroweak Measurements and Constraints on the Standard Model, CERN-EP/99-15 (1999).